

ELECTRON TOMOGRAPHY OF DEFECTS

This dissertation is submitted for the degree of Doctor of
Philosophy

by Joanne Sharp

Of Wolfson College

Submitted 26th April 2010

Acknowledgements

This dissertation is the result of my own work and includes nothing which is the outcome of work done in collaboration except where specifically indicated in the text.

The data and images presented in Section 3.3 from the weak-beam dark-field tilt series of gallium nitride were presented as part of my MSci dissertation at the University of Cambridge in 2005. They are the first attempt at defect tomography in the electron microscope in the world and as such are an important part of this work. The reconstruction of the data for that dissertation was initially done using a different software package that produced inferior results to the one used for the reconstruction in this thesis. Reconstruction with the new software has been done since that time and is presented here; some parameters from the MSci work have been quoted here but are accompanied by references to papers published from that work.

Experimental assistance was provided by Dr Jonathan Barnard, Senior Technical Officer in the HREM group. The initials JSB are used as a shorthand where it is indicated in the text that he collaborated on that part of the work.

This dissertation contains 38400 words.

Dedication

I owe immense gratitude to my supervisor Paul Midgley who found somehow the right balance between honesty and kindness. Innumerable times he has been more helpful than I could have imagined.

I would also like to thank Jon Barnard who taught me to use the electron microscope, helped with these experiments and rescued me from many microscope disasters, as well as Graham Sharp our technician who keeps everything running and Robin Taylor before him. Everybody in the HREM group at Cambridge has patiently given me advice when needed, but especially Tom White, fellow PhD student who fixed the things I broke during the transition from complete novice to halfway-competent programmer, without beating me over the head with a keyboard even once. I literally could not have done any of this without your help. Robin Schäublin is to be thanked for allowing and teaching me to use CUFOUR, and Ana Hungria for teaching me to use Inspect3D.

My long-suffering friends are also to be thanked, for listening to all the rants and pointing out blatant errors. I would also like to thank the doctors and nurses of illegible or unrecorded name who saved my life after an unexpected illness in my second year and dealt with the ensuing fallout; I may have passed you in a corridor without recognition many times but I hope we were both smiling.

We choose to go to the moon in this decade and do the other things, not only because they are easy, but because they are hard.

John F Kennedy, 1962

Contents

| | | |
|----------|---|-----------|
| 1 | Introduction | 1 |
| 1.1 | Dislocations: the purpose of this work | 1 |
| 1.2 | Electron microscopy of dislocations | 3 |
| 1.2.1 | Dark field imaging | 5 |
| 1.2.2 | Dislocations in STEM | 6 |
| 1.3 | The effect of TEM sample preparation | 9 |
| 1.3.1 | Effect of mechanical shaping methods | 10 |
| 1.3.2 | Non-mechanical shaping methods | 11 |
| 1.3.3 | Thinning to electron transparency by chemical polishing | 12 |
| 1.3.4 | Thinning to electron transparency by ion milling | 13 |
| 1.4 | Image processing | 15 |
| 1.4.1 | Techniques to remove background noise | 15 |
| 1.4.2 | Techniques to enhance dislocation contrast | 19 |
| 2 | Tomography | 21 |
| 2.1 | Introduction to tomography | 21 |
| 2.1.1 | Precedent for dislocation tomography | 23 |
| 2.1.2 | The projection requirement - a requirement for successful tomography | 23 |
| 2.2 | Alignment of images | 25 |
| 2.2.1 | Lateral alignment | 26 |
| 2.2.2 | Tilt axis alignment | 27 |
| 2.2.3 | Other misalignments | 27 |
| 2.3 | Reconstruction by weighted back projection | 29 |

| | | |
|----------|--|-----------|
| 2.3.1 | The Fourier slice or projection-slice theorem | 29 |
| 2.3.2 | Weighting | 31 |
| 2.4 | Reconstruction by algebraic reconstruction techniques | 32 |
| 2.5 | Other reconstruction techniques | 35 |
| 2.5.1 | Maximum entropy techniques | 36 |
| 2.5.2 | Discrete tomography | 36 |
| 2.6 | Limitations of electron tomography | 37 |
| 2.6.1 | The missing wedge | 37 |
| 2.6.2 | Minimum reliable spacing of features | 39 |
| 3 | Tomography of dislocations using weak-beam dark field images | 49 |
| 3.1 | Basis of the weak-beam dark field (WBDF) technique | 49 |
| 3.1.1 | Dislocations in the kinematical theory of electron diffraction | 49 |
| 3.1.2 | Dislocations in the dynamical theory of electron diffraction | 52 |
| 3.1.3 | The weak-beam dark field technique | 53 |
| 3.2 | Using the WBDF technique for electron tomography | 54 |
| 3.2.1 | Weak-beam dark-field contrast and the projection requirement | 55 |
| 3.2.2 | The Fourier slice theorem and WBDF dislocation tomography | 58 |
| 3.3 | The first test of weak-beam dark-field dislocation tomography: gallium nitride | 61 |
| 3.3.1 | Procedure | 62 |
| 3.3.2 | Results and discussion | 63 |
| 3.4 | Weak-beam dark-field tomography of a microcrack in Si using tilt series around multiple axes | 70 |
| 3.4.1 | Tilt series acquisition | 72 |
| 3.4.2 | Results and reconstruction | 72 |
| 3.4.3 | Discussion: implications for WBDF tomography of stacking faults | 79 |

| | | |
|----------|--|------------|
| 3.5 | Dislocations in a Ti-Al alloy reconstructed by weak-beam dark-field tomography | 86 |
| 3.5.1 | TiAl samples | 86 |
| 3.5.2 | Tilt series collection | 87 |
| 3.5.3 | Reconstruction | 89 |
| 3.6 | Problems in using WBDF images for dislocation tomography . | 93 |
| 3.7 | Conclusions and further work | 97 |
| 4 | ADF STEM for dislocation tomography | 99 |
| 4.1 | Basic concept | 99 |
| 4.2 | STEM tomography of GaN | 101 |
| 4.2.1 | Procedure | 103 |
| 4.2.2 | Results | 103 |
| 4.2.3 | Discussion | 105 |
| 4.3 | ADF STEM tomography of silicon | 112 |
| 4.3.1 | Sample and experimental details | 112 |
| 4.3.2 | Results | 114 |
| 4.3.3 | Discussion | 115 |
| 4.4 | ADF STEM tomography of dislocations in TiAl | 118 |
| 4.4.1 | Experiment | 118 |
| 4.4.2 | Results | 120 |
| 4.4.3 | Discussion | 125 |
| 4.5 | Conclusions and further work | 128 |
| 5 | Theoretical considerations for ADF STEM tomography of defects | 131 |
| 5.1 | Introduction | 131 |
| 5.2 | Contributions to ADF-STEM defect images | 132 |
| 5.2.1 | Differences in Bragg scattering | 132 |
| 5.2.2 | Thermal diffuse scattering | 135 |
| 5.2.3 | Huang scattering | 140 |
| 5.3 | Bloch wave theories for ADF STEM dislocation contrast . . . | 142 |
| 5.3.1 | Incorporating the convergent beam | 142 |

| | | |
|----------|--|------------|
| 5.3.2 | Thermal diffuse scattering in Bloch wave theories . . . | 143 |
| 5.3.3 | Application to dislocations | 144 |
| 5.4 | Dechanneling | 148 |
| 5.5 | Inner detector angle | 149 |
| 5.5.1 | Importance of Higher Order Laue Zones to ADF STEM dislocation images | 150 |
| 5.6 | Application of ADF STEM contrast to tomography: the effect of tilting | 150 |
| 5.7 | Conclusions and further work | 153 |
| 6 | Conclusions and further work | 159 |
| 6.1 | Conclusions from weak-beam dark-field tomography experiments | 159 |
| 6.2 | Conclusions from annular dark field STEM tomography experiments | 160 |
| 6.3 | General conclusions | 161 |
| 6.4 | General experimental improvements | 162 |
| 6.5 | Further work on WBDF tomography | 162 |
| 6.6 | Further work: ADF STEM tomography | 164 |
| A | Fourier slice theorem for WBDF images | 167 |

Summary

Tomography of crystal defects in the electron microscope was first attempted in 2005 by the author and colleagues. This thesis further develops the technique, using a variety of samples and methods. Use of a more optimised, commercial tomographic reconstruction program on the original GaN weak-beam dark-field (WBDF) tilt series gave a finer reconstruction with lower background, line width 10-20 nm. Four WBDF tilt series were obtained of a microcrack surrounded by dislocations in a sample of indented silicon, tilt axes parallel to $\mathbf{g} = 2\bar{2}0, 220, 400$ and 040 . Moiré fringes in the defect impaired alignment and reconstruction. The effect on reconstruction of moiré fringe motion with tilt was simulated, resulting in an array of rods, not a flat plane. Dislocations in a TiAl alloy were reconstructed from WBDF images with no thickness contours, giving an exceptionally clear reconstruction. The effect of misalignment of the tilt axis with systematic row $\mathbf{g}(n\mathbf{g})$ was assessed by simulating tilt series with diffraction condition variation across the tilt range of $\Delta n = 0, 1$ and 2 . Misalignment changed the inclination of the reconstructed dislocation with the foil surfaces, and elongated the reconstruction in the foil normal direction; this may explain elongation additional to the missing wedge effect in experiments.

Tomography from annular dark-field (ADF) STEM dislocation images was also attempted. A tilt series was obtained from the GaN sample; the reconstructed dislocations had a core of bright intensity of comparable width to WBDF reconstructions, with a surrounding region of low intensity to ~ 60 nm width. An ADF STEM reconstruction was obtained from the Si sample at the same microcrack as for WBDF; here automatic specimen drift correction in tomography acquisition software succeeded, a significant improvement. The microcrack surfaces in Si reconstructed as faint planes and dislocations were recovered as less fragmented lines than from the WBDF reconstruction. ADF STEM tomography was also carried out on the TiAl sample, using an detector inner angle (β_{in}) that included the first order Bragg spots (in other series β_{in} had been $4-6\theta_B$). Extinctions occurred which were dependent on tilt; this produced only weak lines in the reconstruction. Bragg

scattering in the ADF STEM image was estimated by summing simulated dark-field dislocation images from all Bragg beams at a zone axis; a double line was produced. It was hypothesised that choosing the inner detector angle to omit these first Bragg peaks may preclude most dynamical image features. Additional thermal diffuse scattering (TDS) intensity due to dilatation around an edge dislocation was estimated and found to be insignificant. The Huang scattering cross section was estimated and found to be 9\AA , ten times thinner than experimental ADF STEM dislocation images. The remaining intensity may be from changes to TDS from Bloch wave transitions at the dislocation; assessing this as a function of tilt is for further work. On simple assessment, only three possible axial channeling orientations were found over the tilt range for GaN; if this is typical, dechanneling contrast probably does not apply to defect tomography.

Chapter 1

Introduction

1.1 Dislocations: the purpose of this work

Defects are an important factor in the behaviour of materials and it is therefore important to understand how they form and interact. For example, metals tend to deform under a force instead of fracturing because dislocations move and absorb energy; crystal defects in semiconductor devices such as light emitting diodes can trap electrons and inhibit light emission.

In particular the interactions between dislocations are important in how they affect material properties. They may form tangles and be immobilised, such as the Lomer-Cottrell interaction in face-centred cubic metals, or form arrangements that produce more dislocations, such as Frank-Read sources [1]. Understanding these interactions is necessary to understand material behaviour. Dislocation interactions occur in three dimensions, and a single 2D image can be only partially informative or even misleading; the aim of this work is to develop a method to observe them in 3D. No method has done this completely before, though X-ray topography and TEM stereo pairs have been successful under some circumstances (Chapter 2).

A dislocation is described by its line direction \mathbf{l} and Burgers vector \mathbf{b} defined using the Finish-Start/Right-Hand rule (Figure 1.1). Line direction is usually referred to as \mathbf{u} , but as \mathbf{u} will be introduced as the displacement vector, line direction is \mathbf{l} here.

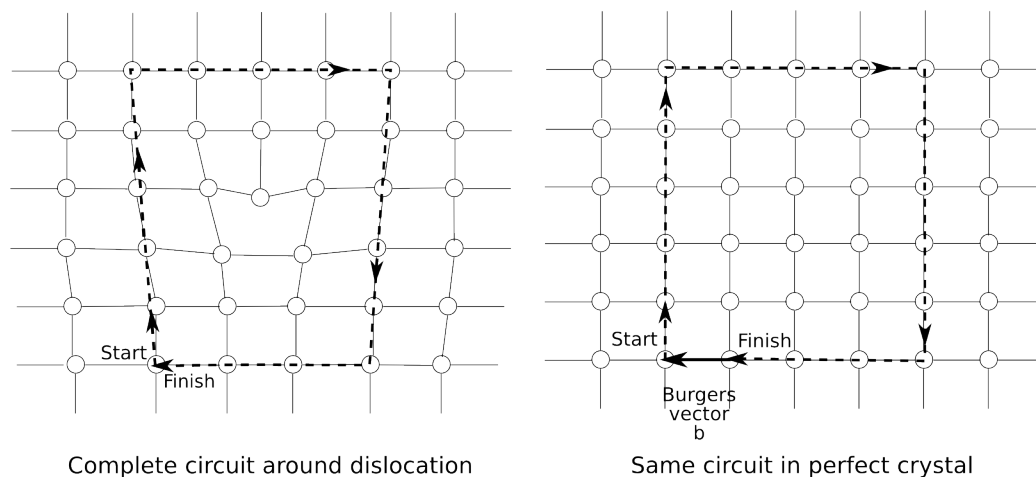


Figure 1.1: The Finish-Start/Right-Hand convention (FS/RH) for determining the Burgers vector of a dislocation. A complete circuit is made around the dislocation such that if the thumb of a right hand points along the chosen line direction (here, into the page), the circuit follows the fingers. The same path in lattice vectors is then taken in a perfect crystal; the Burgers vector is the step needed to join the finish to the start of the path in the perfect crystal, i.e. the overall displacement that has been induced by the dislocation.

The **character** of a dislocation describes the relation between line direction and Burgers vector:

Edge dislocation has \mathbf{l} perpendicular to \mathbf{b} ; the displacement field has components only in the plane perpendicular to \mathbf{l} and there is a small change in crystal volume; it is as if an extra plane of atoms has been added starting at the dislocation line.

Screw dislocation has \mathbf{l} parallel to \mathbf{b} ; there is no overall change in volume and the displacement is all in the direction of \mathbf{l} and \mathbf{b} .

Mixed dislocation is part screw and part edge, and has displacement components along the dislocation and in the plane perpendicular to \mathbf{l} . A mixed dislocation is often specified by the angle between \mathbf{l} and \mathbf{b} .

In elastically isotropic crystals, the displacement field $\mathbf{u}(x, y, z)$ (Cartesian) or $\mathbf{u}(r, \theta, z)$ (cylindrical polar) around a general straight dislocation can be given in an analytical form, with an edge component (Equations 1.1 in

Cartesian co-ordinates or 1.2 in cylindrical polars) and a screw component (Equation 1.3) [1]. In these expressions, \mathbf{b}_e and \mathbf{b}_s are the edge and screw components of the Burgers vector and ν is the Poisson ratio of the material.

$$u_x = \frac{|\mathbf{b}_e|}{2\pi} \left[\tan^{-1} \frac{y}{x} + \frac{xy}{2(1-\nu)(x^2+y^2)} \right] \quad (1.1)$$

$$u_y = -\frac{|\mathbf{b}_e|}{2\pi} \left[\frac{1-2\nu}{4(1-\nu)} \ln(x^2+y^2) + \frac{(x^2-y^2)}{4(1-\nu)(x^2+y^2)} \right]$$

$$u_r = \frac{|\mathbf{b}_e|}{2\pi} \left[-\frac{1-2\nu}{2(1-\nu)} \sin \theta \ln r + \frac{\sin \theta}{4(1-\nu)} + \theta \cos \theta \right] \quad (1.2)$$

$$u_\theta = \frac{|\mathbf{b}_e|}{2\pi} \left[-\frac{(1-2\nu)}{2(1-\nu)} \cos \theta \ln r - \frac{\cos \theta}{4(1-\nu)} - \theta \sin \theta \right]$$

$$u_z(r, \theta) = |\mathbf{b}_s| \frac{\theta}{2\pi} = \frac{|\mathbf{b}_s|}{2\pi} \tan^{-1} \frac{y}{x} \quad (1.3)$$

These edge and screw displacement fields are plotted in Figure 1.2.

1.2 Electron microscopy of dislocations

The first direct observations of dislocations were recorded by Hirsch *et al.* in Cambridge in 1956 [2], in transmission electron microscope (TEM) images of heavily deformed aluminium. A simplified explanation of this contrast, following Bragg's model of diffraction in which electrons are reflected from planes of atoms, is that the bending of atom planes by the dislocation's displacement field redirects intensity away from the bright field beam into dark field beams (Figure 1.3). Planes on one side of the dislocation are bent into the diffraction condition for scattering into a dark field reflection, thus giving a line of brighter intensity within the dark field image corresponding to the line where the planes are bent. A dark line is left in the bright field image where this has occurred. The same dislocation can diffract electrons into other dark field beams, because the curvature of the planes varies around the dislocation core. The line image appears to one side of the actual position

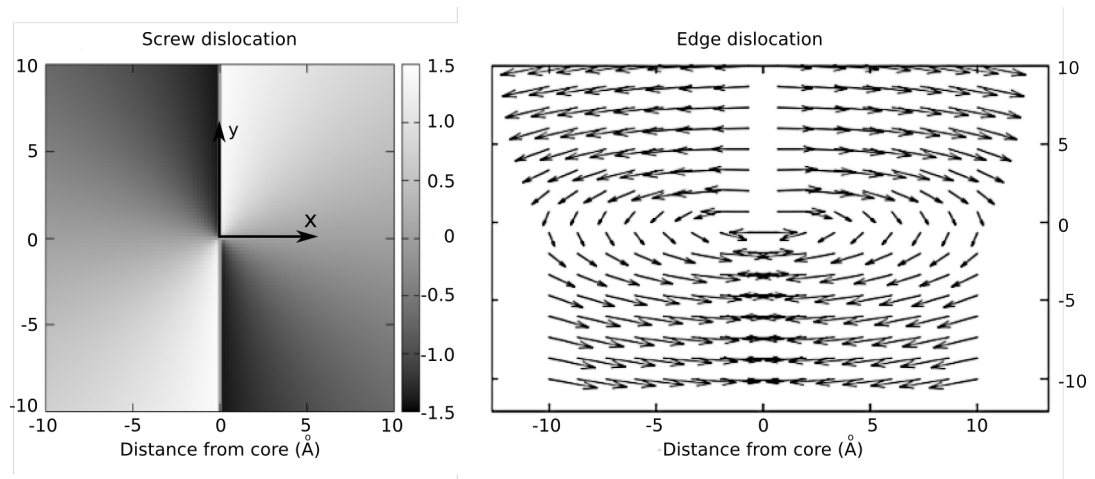


Figure 1.2: Displacement fields of screw and edge dislocation components, with dislocation core pointing out of the page along coordinate z . Coordinates x and y are as shown; polar coordinate θ is measured anticlockwise from the x axis direction. Screw component: intensity shows magnitude of displacement in \AA , pointing out of the page in the direction of the dislocation line; the atom planes spiral around the core, but discontinuities are shown above and below where the arbitrary distinction is drawn between parts that belong to the above plane and are displaced downwards, and parts that belong to the underneath plane and are displaced upwards. The total displacement for one 2π rotation around the core runs through almost two circuits of the grey range, corresponding to 5.73 \AA , the lattice spacing along the dislocation's line direction. Edge component: arrows show direction and size of displacement, which is in the plane perpendicular to the line direction.

of the dislocation core, because the curvature occurs there and not at the core; the profile and position of the dislocation line image are thus different in images from different dark field reflections.

Dislocations are also seen in scanning transmission electron microscope (STEM) images; observed image contrast depends on the detector geometry. This section is only a brief introduction to these imaging methods: they will be covered extensively in later chapters.

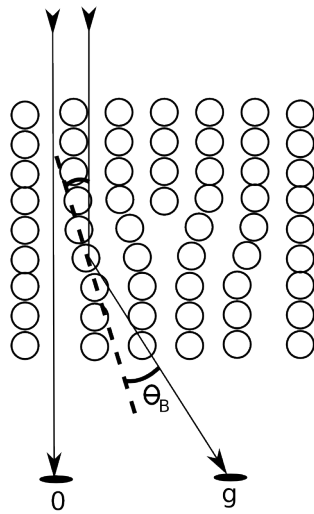


Figure 1.3: Schematic diagram of diffraction of extra intensity into dark field spots by distortion of atom planes around a dislocation. Angle θ_B is ~ 5 mrad ($\sim 0.3^\circ$) but exaggerated here for clarity.

1.2.1 Dark field imaging

The dislocation contrast in dark field images can be predicted using the kinematical and dynamical theories of electron diffraction developed by Hirsch, Howie *et al.* [3] and the displacement fields of dislocations as described above. Qualitatively, the kinematical theory predicts a dislocation of Burgers vector \mathbf{b} will give bright contrast in a dark field image from a diffracted beam \mathbf{g} if $\mathbf{g} \cdot \mathbf{b} \neq 0$, i.e. if the Burgers vector has some component that can bend atom planes in the direction of \mathbf{g} . The displacement field of an edge dislocation also has a small component perpendicular to \mathbf{b} (see

Figure 1.2), so dislocations of line direction \mathbf{l} that have any edge character also give contrast if $\mathbf{g} \cdot (\mathbf{b} \times \mathbf{l}) \neq 0$, even when $\mathbf{g} \cdot \mathbf{b} = 0$. By taking dark-field images from at least three diffraction spots of linearly independent \mathbf{g} and assessing dislocations' visibility in each image, the Burgers vectors of the dislocations can be deduced.

1.2.2 Dislocations in STEM

STEM is quite different from conventional TEM. The beam is much more convergent, forming a probe typically ≈ 1 nm across on the sample, where normally a field of view of 200-5000 nm is illuminated. Scan coils raster this narrow probe across the image, and the **diffraction pattern** from each point arrives on the STEM detector; it is normally restored to the optic axis by another set of scan coils (Figure 1.4). The signal recorded at each pixel is the sum of the diffraction pattern intensity falling on the detector from that point. The STEM detectors are separate from the CCD used to record conventional TEM images; the signal recorded depends strongly on the detector's shape and size. There are two kinds of detector commonly used for STEM:

Bright field detector — receives the straight-through (undiffracted) beam and possibly some of the diffracted/scattered intensity, depending on its radius.

Annular dark field (ADF) detector — receives the diffracted beams and thermal diffuse scattering over a range of scattering angles, cut off at its inner and outer radii.

The angular range over which an annular detector can receive intensity depends on the camera length used to place the diffraction pattern on the detector (Figure 1.5) — a longer camera length translates to smaller inner and outer collection angles, collecting fewer and larger diffraction spots from closer to the centre of the diffraction pattern.

At long camera lengths (small β_{in}), the intensity collected by both detectors is mainly from coherent Bragg scattering close to the optic axis.

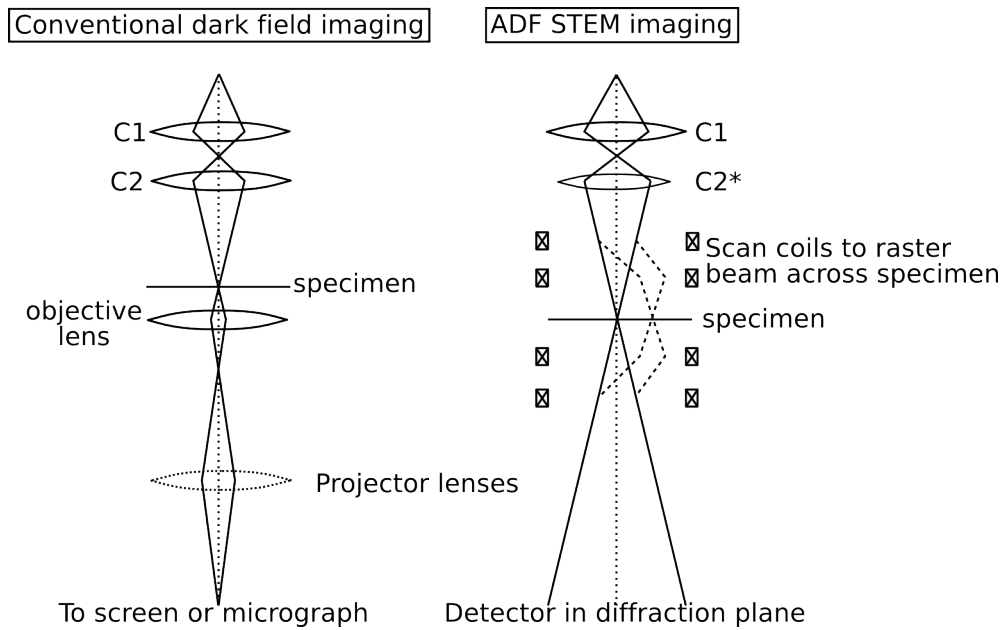


Figure 1.4: A comparison of conventional dark field imaging and annular dark field STEM imaging. The beam in STEM is more convergent than in conventional DF imaging; the action of C2 in the STEM case is actually achieved by a combination of C2 and the upper polepiece of the objective lens. The projector lenses are here simplified into one and are idle in STEM mode, allowing the diffraction pattern to fall on the detector from the present probe position.

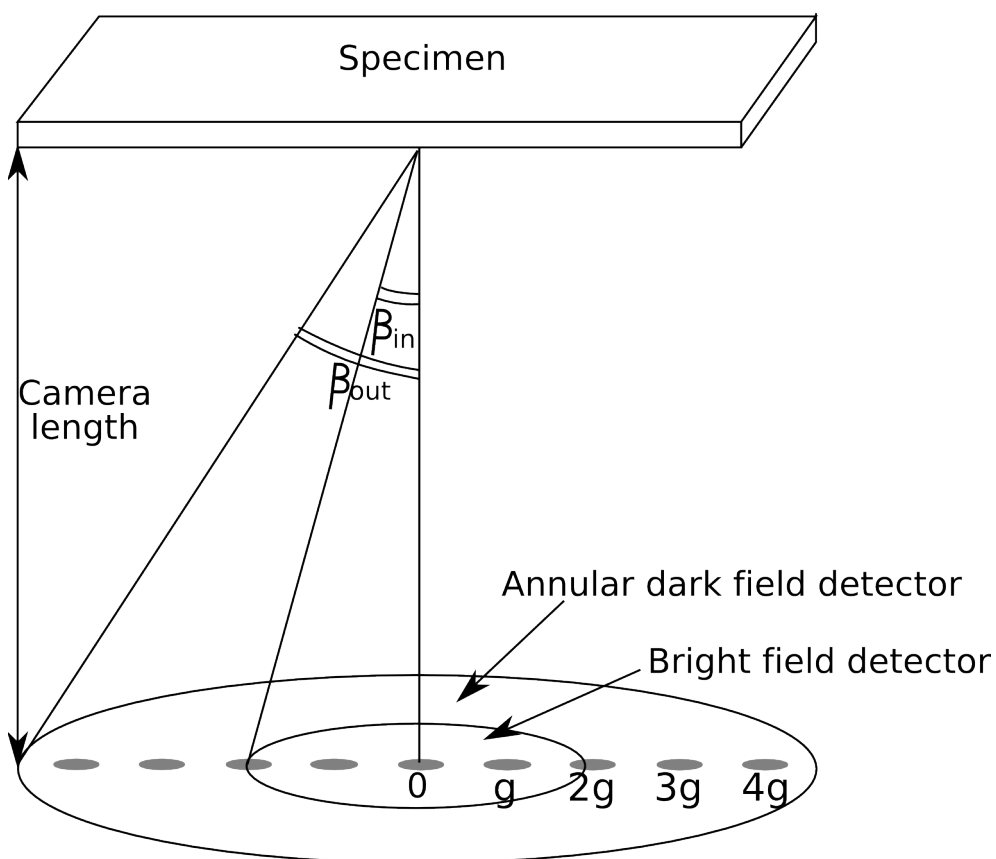


Figure 1.5: Bright field and dark field STEM detectors, showing inner and outer collection angles of ADF detector, β_{in} and β_{out} , and camera length. A systematic row orientation is chosen so the diffraction pattern can be shown more clearly. This is a simplified geometry equivalent to the analogous X-ray experiment; effective camera lengths for the electron microscope are calibrated such that calculations can be done using this diagram.

At very short camera lengths (large β_{in}), most of the zero order Laue zone falls on the bright-field detector, and intensity collected by the annular dark field detector is mainly from Rutherford-type mass-thickness contrast and thermal diffuse scattering. Dislocations also contribute to this short camera length HAADF (high-angle) STEM image because they give more large angle scattering than the undisturbed crystal around them. At intermediate collection angles the situation is complicated and has not been fully explored; Chapter 5 considers this further.

1.3 The effect of TEM sample preparation

The TEM specimen must be very thin to be electron transparent, of the order hundreds of nanometres; it must also be either a disc of the correct size for the specimen holder, or able to be mounted on a grid of that size. The process of thinning the specimen may change the dislocation structure in the material, and if this is not allowed for, any defect tomography will not provide correct information on the material. In addition some sample geometries are not adequate for tomography; this section provides a brief summary of which methods are appropriate for a sample that will be used for dislocation tomography.

Defects may be affected by sample preparation in two ways: by mechanical damage causing ductile deformation, and through **image forces**. Image forces are experienced by a dislocation when it is close to a specimen surface, and arise because the dislocation's stress field is no longer restricted by the surrounding mass of perfect crystal on the side close to the surface. The most common effect of this is for the dislocation to be attracted to the surface, as if a dislocation of the opposite sign were the other side of it [1, pp 68&86], hence the term image forces. When the sample is thinned, dislocations near the surfaces experience image forces they were not exposed to in the bulk, and may move from their previous positions and even escape through the surfaces. To give a worst case, for example, image stresses on prismatic loops in water-quenched copper foils have been reported to be great enough to cause dislocation loss up to 250 Å from the surface [4].

The effect of sample preparation depends on the mobility of dislocations in the sample: a material in which dislocations are less mobile at the temperature at which the sample is prepared, such as silicon at room temperature, will experience less dislocation movement during sample preparation than a very ductile material such as pure copper. Dislocation mobility depends on crystal parameters such as the Peierls stress [5] required to move a dislocation through the crystal, and on other defects that are present. Dislocations are pinned by precipitates [6] and point defects [7], and become tangled with other dislocations following interactions, and pinned that way also [8]. Surface oxide can also retard the motion of dislocations that intersect the surface [9], [10], [11]. There is a dependence on temperature: at high temperatures, point defect processes such as climb can be activated [12] allowing dislocations to escape pinning sites, and additional slip systems may be activated such as the ductile-brittle transition in silicon in the range 700 – 950°C [13].

1.3.1 Effect of mechanical shaping methods

Mechanical methods are the conventional way of removing a small specimen from a large piece of material. Plastic deformation from techniques such as sawing extends for typically 150 μm under the apparently undamaged new surface of a ductile material [14], so that at least this much material is unrepresentative of the bulk. Using ultrasonic cutting appears to reduce the size of the plastic zone beside the cutting tool, in ductile materials [15]. As for brittle materials, surface damage from ultrasonic dimpling has been reported in silicon [16], similar to that made by ordinary abrasion, down to a depth of $\approx 20 \mu\text{m}$.

To remove further material, the sample is ground and polished. The surfaces of a disc sample may also be polished into a dimple to ensure final thinning to transparency occurs in the centre. Optical microscopy and TEM have been used previously to assess abrasion damage in silicon [17]; the coarse abrasives used in grinding introduced cracks with severely strained dislocation networks between them, to 16 μm below the new surface. The fine

abrasives used in polishing with $0.25\ \mu\text{m}$ diamond left single dislocations to a depth of 200 nm below the new surface. Polishing processes typically removed a thickness of $\sim 60\ \mu\text{m}$ of material, enough to remove grinding damage. $0.02\ \mu\text{m}$ is a typical grade of polishing solution used for tripod polishing, which is generally considered to leave brittle semiconductor specimens with sufficiently low amounts of damage as to give some area with defect structure typical of the material before sample preparation. A similar study in brass [18] (more ductile, with more damage expected) found the maximum depth of plastic deformation to be $40\ \mu\text{m}$ in the case of 600-grade abrasion and $4\ \mu\text{m}$ for polishing — mean depth $0.7\ \mu\text{m}$ but with occasional large gouges. Therefore, in ductile materials, the additional thinning needed after mechanical polishing is also necessary to remove the damaged layer left behind by polishing.

The shape of the particles used to polish a sample is important; pointed particles of diamond can become stuck in ductile materials such as copper, so rounder particles such as aluminium oxide are used for these samples [19]. As seen by comparing silicon and brass, subjecting a ductile material to abrasion causes much deeper disruption than in a brittle material, as energy is diverted to plastic deformation.

1.3.2 Non-mechanical shaping methods

Spark cutting may be used, in which matter is removed by vaporising material in a spark discharge. The depth of damage from spark cutting of a (111) face in copper has been found to be $\sim 300\ \mu\text{m}$ [20]; similar studies in brass [21] found plastic zones that extended down $280\ \mu\text{m}$.

An alternative way of obtaining a disc from a sheet, or a thin slice from a large piece, is to apply electropolishing to a small area to remove material along a cut [22], [23]. These methods do not introduce any additional deformation into the sample, but in a material with high dislocation mobility (for which these methods are generally used) dislocations may still escape due to image forces at the new surfaces. The parts that do not need to be cut must be covered with an acid resistant lacquer such as Lacomit if the cut is

to be sharp [22].

1.3.3 Thinning to electron transparency by chemical polishing

Chemical polishing is the standard method used to thin metallic samples to electron transparency. The sample is eroded by a corrosive solution until a hole develops that lets light through, indicating that the material surrounding the hole is probably electron transparent. Electrochemical thinning (electropolishing) applies an electrical potential between the sample and another part of the apparatus, which aids the reaction and allows one to prepare metals that otherwise passivate, and to use less corrosive solutions.

A study using precipitate hardening in aluminium–silver alloys [6], however, showed that up to 60% of dislocations could be lost through the surface by escape due to image forces during electropolishing. Other studies on deformed Ni-Co alloys [24] prepared by only electrochemical techniques found almost no screw dislocations in some sections, though slip line studies on the same batch disagreed [25], and they were present in other sections. It was proposed that the more mobile screw dislocations were lost by cross-slip at the surfaces, and some edge dislocations also. Screw dipoles can also mutually annihilate by cross-slip under stress, leaving short edge dipoles and loops as a clue that this has occurred [26] [27]. Not all dislocations will be lost, however; indeed the interesting dislocations are often those in tangles that do not escape or even move (Figure 1.6). The early studies referred to here were carried out on pure metals and present rather a worst case scenario; electropolishing is considered a reliable and versatile technique [28].

If the crystallographic section is chosen carefully so that easy directions for dislocation motion do not point toward the TEM sample surfaces, losses can be minimised; in principle one can orient a foil such that a particular family of dislocations cannot escape at all, if one knows their motion already [20].

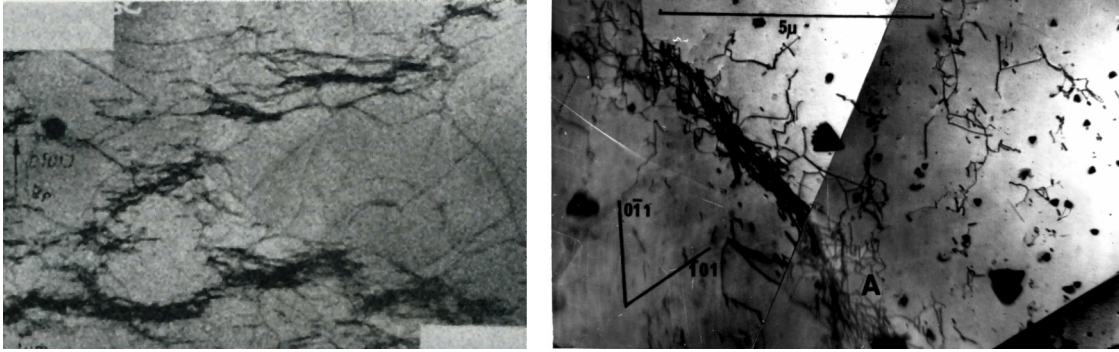


Figure 1.6: Two samples of copper, late Stage II deformation, dark field images taken in g of the form 111. Left: prepared by neutron irradiation pinning to immobilise dislocations, followed by electropolishing [12] (permission gratefully received from H. Mughrabi). Right: prepared by electropolishing alone (permission gratefully received from J. W. Steeds). Any difference is mainly in the regions of low dislocation density, where there are fewer dislocations in the non-pinned sample.

1.3.4 Thinning to electron transparency by ion milling

For samples that cannot be electropolished to the required shape, ion milling techniques are used. The specimen is mounted in a vacuum chamber; a plasma is formed and the ions in the plasma are accelerated toward the specimen. Ions hitting the surface trigger a cascade of collisions in a pear-shaped interaction volume under the surface [29], and atoms are ejected in a plume from the surface. When this sputtering continues, the specimen becomes thinner. The higher the kinetic energy of the ions, the deeper the interaction volume [30]. In copper, for incident ions of 3-5 keV the interaction volume is of the order 2-3 nm [31]. Vacancies and interstitials are created in the collision cascade.

Ion thinning uses two broad beams of ions at relatively low energy, $< 10 keV$ [32]. The beams are incident at an angle, to reduce damage, and the specimen is rotated in the beam so directional artefacts are not produced. The final specimen is biconcave with a thin part in the centre, like an electrochemically prepared specimen.

Focused ion beam milling is a more controlled version: a beam of Ga^+ ions focused down to $< 10 nm$ width with energy typically 30 keV is used to

remove material from specific areas. Secondary ions and electrons are used to form an image of the specimen during milling, so that a feature can be chosen. This is an advantage over other methods, and is especially useful to the semiconductor industry for analysis of specific features on silicon chips e.g. [33].

Geometries of FIB prepared specimens are one of the following [34]:

Trench geometry — a trench is milled either side of the volume of interest, stopping abruptly at the sides of the volume, leaving a thin electron transparent slab between the two trenches. This geometry hinders high-tilt applications: **a trench specimen cannot be used for tomography.**

Lift-out geometry — a piece containing the volume of interest and thin enough to be electron transparent is cut out, and attached to a grid using a micromanipulator.

Point defect clusters created by the ion beam can coalesce and collapse to form dislocation loops of diameter 5-10 *nm* [35], [36], depending on point defect mobility in the material and the energy needed to form a loop. Metals have higher point defect and dislocation mobility than other materials, and because of the low stacking fault energy of close-packed metals, dislocation loops that form on ion milling are of particular concern. Not all metals form dislocation loops - they are seen in steel and copper, for example [37], but not in tin [34]. Unless the material is a difficult case such as a metal matrix composite [38] or a particular sparse feature is required in the sample, electrolytic thinning causes less damage than ion thinning in metallic specimens [31] and is generally used. Less ductile samples tend to form an amorphous layer rather than dislocation loops, which can then be removed by a brief low-energy mill at the end of sample preparation, and ion beam techniques are much more suitable for these samples. Cooling the specimen to 77K has been found to slightly reduce the size of introduced defects in III-IV semiconductors [39] and to reduce formation and migration in metals [31], by decreasing the mobility of point defects.

It has also been found that dislocated material can be preferentially removed during ion milling [40]; it must be borne in mind that the most heavily dislocated areas may have been removed during preparation in ion milled samples.

1.4 Image processing

The images in a tilt series, in the state in which they are taken from the microscope, are not ideal for producing tomographic reconstructions. They contain background noise; in addition the dislocation images may not be continuous where the dislocation is continuous, for example striped dynamical contrast from inclined dislocations in the film (Chapter 3). These problems may be addressed by pre-processing the images before embarking upon the reconstruction process.

When processing the images, care must be taken to preserve the information about the dislocations. It would be misleading and defeat the point of tomography to eliminate dislocations from the images, or to introduce artifacts that were not present in the sample. In this section, image processing techniques useful for this purpose are considered, and the development of a technique adapted for this purpose is outlined.

1.4.1 Techniques to remove background noise

Sharpening

This technique has been used by the author and colleagues to reduce background noise in dislocation images before tomographic reconstruction, to some success. In particular it is useful for some STEM tilt series in which there is a diffuse region of intensity surrounding the bright line of the dislocation, which when reconstructed produces a low intensity region surrounding the dislocation. For the results presented in [41] and [42] using a WBDF tilt series from GaN, and [43] using a STEM tilt series from Si, the images were smoothed repeatedly with a kernel of size 3-20 pixels and then the smoothed version was subtracted from the original image. This was

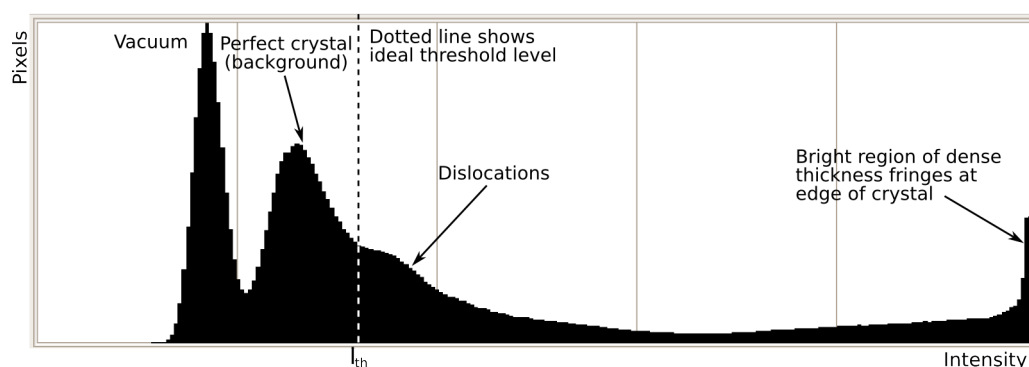


Figure 1.7: Histogram from image in Figure 1.8 showing the basis of thresholding a dislocation image to remove background. Discarding pixels with intensity less than the threshold intensity I_{th} should leave only the dislocations. It is quite difficult to find the best position for I_{th} .

mostly successful, but the strong variations such as thickness fringes near the edge of the specimen were not entirely removed (Figure 1.8).

Thresholding

Ideally, thresholding can be used to remove background noise from dislocation images if the threshold value is set as in Figure 1.7, though this is simplified; the background intensity varies within an image as thickness and curvature of the sample vary, so that in some regions the background is more intense than even the dislocations in other areas. The correct threshold level also varies between images in a tilt series, as the intensity of the background of inelastically scattered electrons varies with tilt. Thresholding with the same level over the whole image is shown in Figure 1.8. It can be seen that most of the background is removed, but some of the dislocation contrast is also removed where it is particularly weak; it would be more successful for images with a higher signal-to-noise ratio.

Fourier filters

An image can be filtered in Fourier space by removing parts of the Fourier transform that correspond to background and unwanted features. The initial

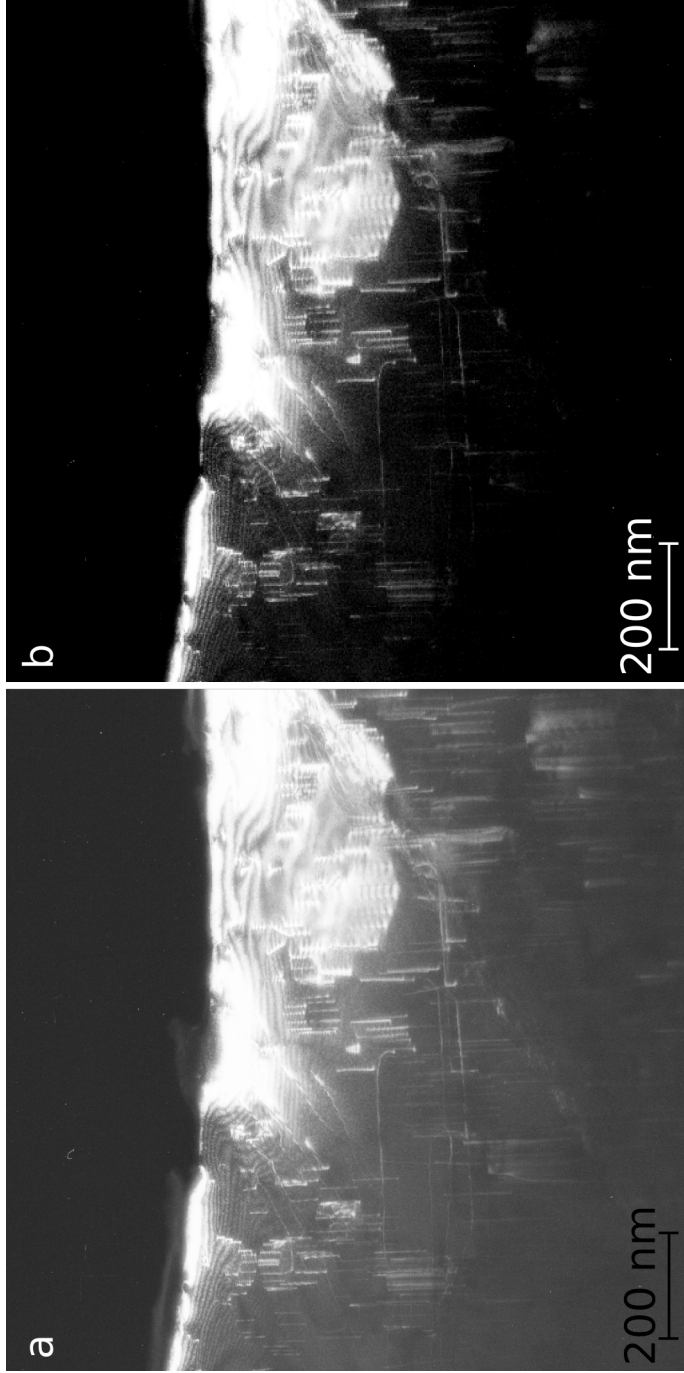


Figure 1.8: (a) Original energy filtered weak-beam dark-field image of dislocations in GaN. (b) The effect of thresholding, which does not improve dislocation clarity in areas of high background. Figure 1.7 is the histogram of the original image and the threshold was placed at the intensity shown to produce (b).

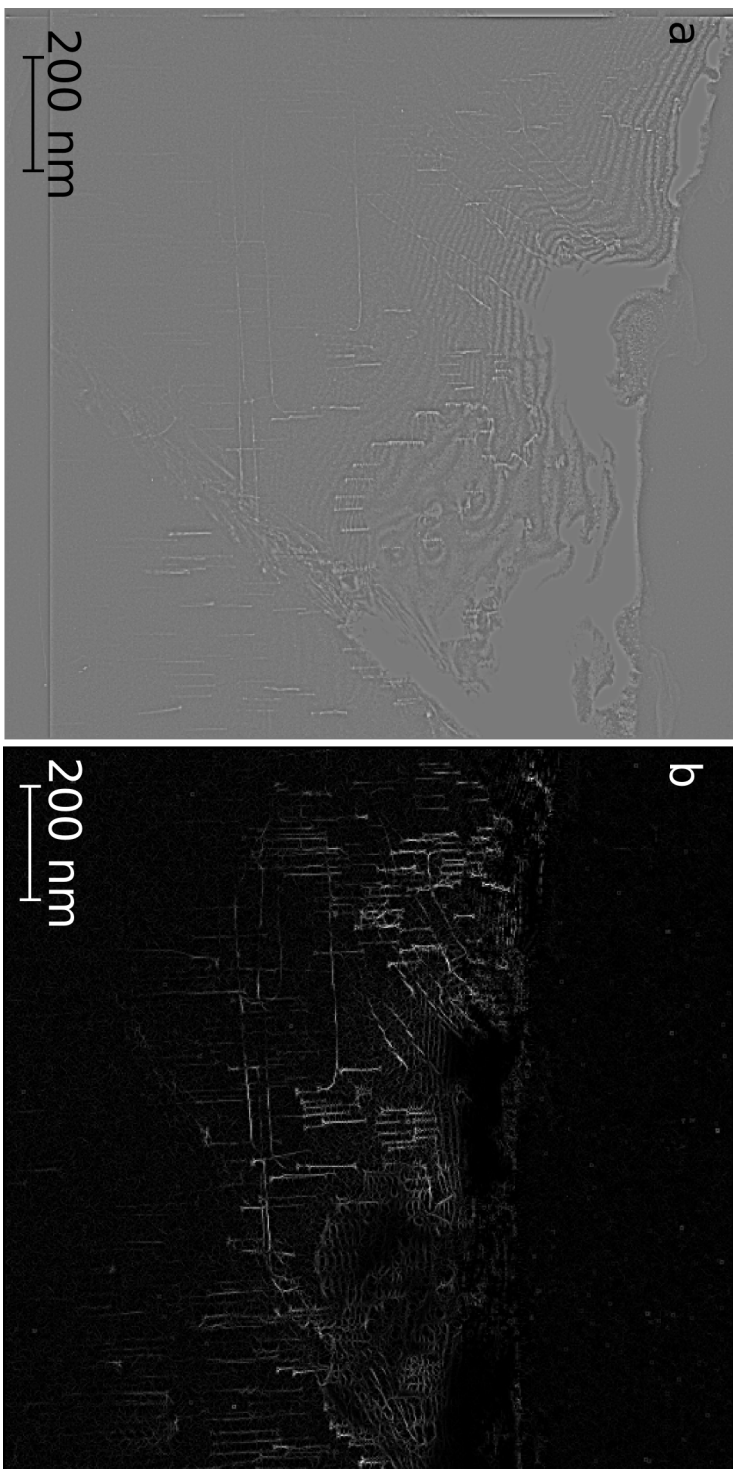


Figure 1.9: (a) The effect of smoothing on Figure 1.8a (from 5° smaller tilt angle in the series); background intensity is high but varies very little. (b) The effect of processing using the linefinding technique as described in text; this appears clear but some dislocation lines are broken, thickness fringes enhanced and a speckled background is introduced.

image processing methods used in our first dislocation electron tomography study [44] used two Fourier filters:

- A bandpass filter to remove the high frequency speckle noise (scale of single pixels) and the low frequency large scale variations in background levels, but not remove the dislocations.
- A directional wedge filter to remove specific sets of background variations that hamper tomography, such as thickness contours.

The directional wedge filter met with limited success; portions of the dislocations were removed by the directional filter, for a relatively small reduction in intensity of thickness contours. In addition the filters required to do this change with tilt, and unless a computer program could be written to determine these changes automatically, this would not be practical for large tilt series.

1.4.2 Techniques to enhance dislocation contrast

Ways to enhance the dislocation contrast include:

Edge finding — images of dislocations are in effect thin lines, and their image should be enhanced well by using an edge finding operation such as a Sobel filter [45]. Applying this appears to give some improvement in reconstruction quality.

Joining up the parts — a major problem is that the dislocation line images are broken, and differently at different tilt angles due to dynamical contrast. Joining up the parts to make continuous lines ought to give a better reconstruction of where the dislocation core runs, provided joins are not made where there were not dislocation lines in the specimen.

Isotropically dilating a dislocation image only appears to help a little in linking the dislocation parts together, and the noise is also dilated such that the net effect is not good. Anisotropic dilation gives more success in joining

up parts of broken dislocation line images; a version was written by the author and colleagues to test on dislocation tilt series before reconstruction, and was found to enhance dislocation contrast but also enhance thickness contours and background noise (Figure 1.9).

Image processing techniques that enhance dislocation contrast are different in principle to those which act on the background: there is a danger that they could be used to join up lines that are not part of the same dislocation. Manual segmentation, as done for a different silicon sample by collaborators at Kyushu University after these initial studies [46], in a case where material properties and general dislocation behaviour are well known and can be used as *a priori* knowledge, is a way to achieve similar results that is less prone to such errors. This too could be misleading if used on a completely new defect structure, however.

Chapter 2

Tomography

2.1 Introduction to tomography

Tomography is the reconstruction of an n -dimensional object or structure from a series of $(n - 1)$ -dimensional projections. It was originally used as a technique in 1917 [47], developed rapidly from the 1960s onwards, and is now used commonly in medical science to image parts of living bodies on a macro scale, using techniques such as positron emission tomography [48]. X-ray tomography is used in the physical sciences for applications such as finding the shape of cracks and cavities in materials or components [49]. Tomography in the electron microscope has been used to reconstruct biological specimens such as viruses or cell organelles since the late 1960s [50]. Recently, electron tomography has been adopted as a micro- or nanoscale technique for materials science [51].

Tomography in the electron microscope is special in a number of ways. The source (electron gun) and detector are fixed and cannot be scanned around the sample as in medical tomography; the sample is instead rotated in the beam by tilting the specimen holder, to give a series of projections (images) of the sample at a range of angles — a tilt series. The subsequent process of reconstruction consists of the stages described in Figure 2.1.

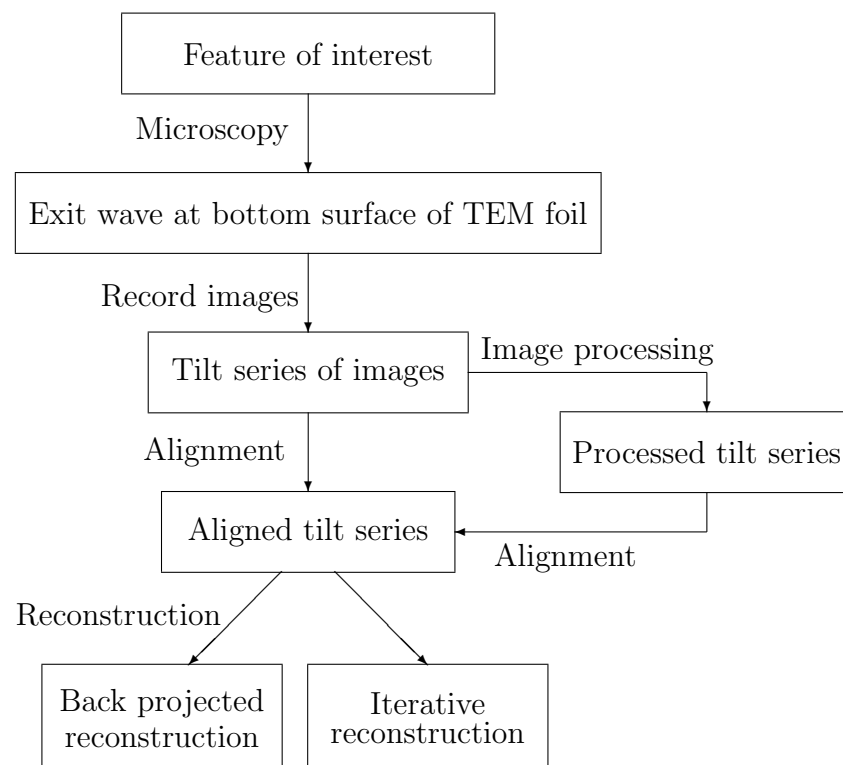


Figure 2.1: Flowchart showing steps required for electron tomography.

2.1.1 Precedent for dislocation tomography

Dislocations have previously been represented in 3D using stereo pairs [52], using electron microscopy or X-ray topography. This technique uses two dark field images taken in the same reflection \mathbf{g} , and the sample is rotated by $\sim 15^\circ$ about a tilt axis parallel to \mathbf{g} . The two images are viewed in the two eyepieces of a stereo viewer to give a loose 3D representation. Some time later, X-ray stereo pair topography was developed by Ludwig et al. [53] into X-ray topo-tomography. A tilt series was recorded as the sample was rotated 180° in the X-ray beam, keeping the imaging reflection constant as initially suggested by Haruta [54]. The reconstruction resolved dislocations with separations of the order of $100 \mu\text{m}$ in a sample of diamond.

The resolution of X-ray topo-tomography is limited by the width of a dislocation image in a dark-field X-ray beam, given in Equation 2.1:

$$w(\mathbf{b}, \lambda, F_g) \approx \frac{V_c \cos \theta_B(\mathbf{g}, \mathbf{b})}{2r_e \lambda C (F_g F_g^*)^{1/2}} \quad (2.1)$$

In Equation 2.1, F_g is the structure factor for reflection \mathbf{g} , V_c is the volume of the unit cell, r_e is the classical electron radius and C is the polarisation factor [53]. The reflection \mathbf{g} and the wavelength can be changed to give small improvements; in the paper referenced, dislocation line images are $\approx 50 \mu\text{m}$ wide. Comparable dislocation images from the transmission electron microscope are of the order 1-10 nm. The use of electron microscopy to achieve tomography of dislocations on a finer scale is therefore a logical step to improve 3D imaging of dislocations, and gain information on denser dislocation structures that cannot be reconstructed with the X-ray method.

2.1.2 The projection requirement - a requirement for successful tomography

It is generally acknowledged that tomography of any kind will only work if the object and imaging method fulfil the projection requirement — the images used to make the tomogram:

‘need not necessarily be a (weighted) sum or integral through the structure of some physical property of [the structure]; in principle, a monotonically varying function would be acceptable, although solving the corresponding inverse problem might not be easy’ [55].

In X-ray tomography of components and HAADF STEM electron tomography of nanostructures, the physical property thus measured is approximately the mass-thickness distribution of the object, for example when HAADF-STEM Z-contrast is used to reconstruct heavy metal catalysts on carbon supports [56]. For the contrast modes used to image dislocations, it is not so clear cut.

Weak-beam dark-field contrast is often described using the column approximation, i.e. the image intensity is given by an integral of an appropriate function down columns of the material parallel to the beam direction; an image that can be predicted using the column approximation is therefore a projection suitable for tomography, and this is generally true of weak-beam dark-field images. This is not quite as simple as it seems; the relationship of weak-beam dark-field imaging to the projection requirement will be discussed further in Chapter 3.

Annular dark-field STEM contrast of dislocations has not been investigated as thoroughly as WBDF contrast. For the low-angle detector we have used, at the time of writing there is not an established theory to predict dislocation contrast. Existing theories for ADF-STEM contrast give images that are integrals over depth and therefore can be described as projections, though certainly not simple ones, for example that used by Perovic, Howie and Rossouw to explain ADF STEM dislocation contrast [57]. Simpler theories of high-angle ADF-STEM assume even smaller columns: atomic columns down which channeling occurs when the narrow beam is over that column, the dechanneling from these columns giving a measure of the strain field [58]. This simpler model may not apply to the ADF-STEM used here, however, because the inner detector angle is different, and because channeling applies primarily at zone axis orientations whereas tomographic acquisition tends to avoid such orientations for most of the tilt range. This will be explored further in Chapters 4 and 5.

An additional problem, for both ADF-STEM and WBDF, is that the displacement field of a dislocation is a vector field; tomography has usually been undertaken on scalar quantities such as mass-thickness, and for a vector field, vector field tomography should be used. This is approached from many fields including microscopy of magnetic materials [59]; in that case two tilt series are required to map two components of the magnetic induction vector field \mathbf{B} , then the third is derived from known properties of the field components *i.e.* using Maxwell's equations. The displacement field of a defect would introduce further challenges in vector field tomography. The relations used for vector field tomography are generally that the signal is an integral through the vector field [60], not through a complex function of the vector field as is the case for a dislocation image (See Chapter 3). Vector field tomography of dislocation displacement field is a goal for the future, and the work done so far using normal scalar tomography algorithms is a first step along the way.

2.2 Alignment of images

Before the tilt series images are used to make a reconstruction, they must be aligned in two main ways:

- Shift alignment: as the sample is tilted between images, the stage will experience some sideways movement; the images must be shifted to return the region of interest to the same co-ordinates in each image.
- Tilt axis alignment: reconstruction algorithms assume the tilt axis is along the vertical axis of the images, because the volume can be sliced along the tilt axis without extra calculation, making reconstruction more efficient and faster. The true angle of the tilt axis needs to be found and the images rotated to make this coincide with the vertical image axis.

The normal methods of performing these alignments will be summarised before reconstruction processes are described.

2.2.1 Lateral alignment

Lateral alignment can be performed automatically using a cross-correlation function between adjacent images in the tilt series. The position of the highest peak in the cross-correlation function corresponds to the shift between the two images; one image is shifted by that amount, then the comparison moves to the next image pair, and the process is repeated. To compensate for foreshortening with tilt, images are often stretched perpendicular to the tilt axis before calculating the cross-correlation, by a factor of $\cos\theta$. Filters such as an edge-finding Sobel function, Hanning window or bandpass filter may be applied to make the cross-correlation peak as clear as possible; the calculated shifts are then applied to the unfiltered images.

Diffraction contrast features such as thickness fringes may have a stronger influence on the cross-correlation function than the features of interest. As a sample of non-uniform thickness is tilted, causing the projected thickness to change, thickness fringes move relative to the features. The result of allowing thickness fringes to dominate the cross-correlation function is a progressive misalignment of the features of interest in each image: the features of interest drift across from image to image while the thickness fringes stay in the same place. In the course of developing defect tomography, the following techniques of preventing this problem have been found:

- align the images manually, which is inefficient and introduces human error,
- choose an area such that thickness fringes are restricted to the periphery of the image, and apply a Hanning window before automatic alignment to reduce the contribution of peripheral regions to the cross-correlation function,
- combine both of the above: place thickness fringes near the image boundaries, manually align images for a good starting point, then use the automatic method for final alignment.

It is possible to simply mask out the parts of the images' Fourier transforms that correspond to the thickness fringes; however, because they are often linear features of similar width to the spacings between dislocations, this process tends to also remove parts of dislocations, so has not been further pursued as a strategy.

2.2.2 Tilt axis alignment

No successful completely automatic method for finding the tilt axis is in widespread use; it is done by user judgement. The tilt axis position has two components:

- tilt — the angle it forms with the vertical axis of the images, where the goal is to make this zero
- shift — how far it is from the horizontal centre of the images, at the point where it crosses the vertical centre, also ideally zero.

The rough position of the tilt axis is first observed by running the tilt series in sequence so that it appears as a video of the specimen rotating, and the tilt axis is set to a position that is as correct as possible. The position of the tilt axis is then finely adjusted by choosing slices of the volume which intersect small pointlike features, and backprojecting these slices of all images around an estimated tilt axis; if the estimated tilt axis is misaligned, the points backproject as arcs, as seen in Figure 2.2. The tilt axis is rotated or shifted by a small increment by the user, who then assesses the effect and decides whether to keep or undo the change; the process is iterated until no further improvement can be found. The sum of the rotations and shifts found during alignment is then applied to the tilt series, which should output a tilt series with the tilt axis along the vertical image axis.

2.2.3 Other misalignments

As the specimen is tilted, it can not only shift but also rotate; the magnification may also change. These can be corrected for if gold markers

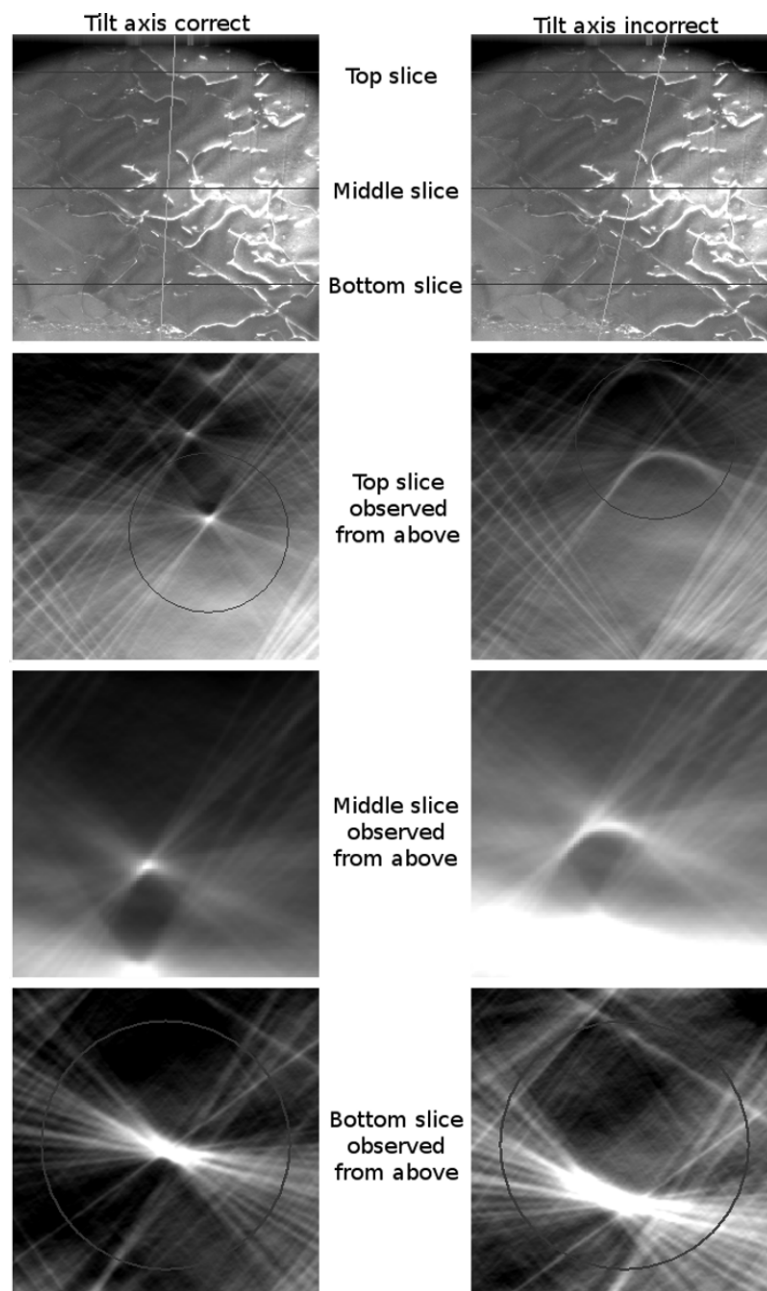


Figure 2.2: Left: correctly located tilt axis. Right: badly located tilt axis. The pale, near-vertical line in the image shows the estimated position of the tilt axis, used for calculating the slices. The slices shown are backprojected around the estimated tilt axis, at the positions shown by the intersections of this tilt axis with the dark horizontal lines on the image (top). The arcing of the feature in the middle slice shows that the tilt axis position (shift) is incorrect; the arcing of features in opposing directions in the top and bottom slices shows that the estimated tilt axis is also inclined with respect to its correct orientation (angle is incorrect).

were used, or if there are features clear enough to track, but dislocation contrast is not suitable for feature tracking and gold markers have yet to be tried for this case.

2.3 Reconstruction by weighted back projection

2.3.1 The Fourier slice or projection-slice theorem

When image intensity follows the projection requirement (Section 2.1.2), it can be represented as the Radon transform of the sample in the loose sense: an array of integrals of some function of the desired property, along straight lines through the sample [61], [62]. The Fourier Slice Theorem then applies. This states that the Fourier transform of a parallel projection of a real-space object $f(x, y)$ taken at an angle θ to the x -axis gives a central slice of the Fourier transform of the object $F(u, v)$, inclined at angle θ to the u -axis of Fourier space [63] — see also Figure 2.3.

When an object and its projections are related by the Fourier Slice Theorem, the object can be reconstructed by **backprojecting** the two-dimensional projections (tilt series images). The process of backprojection is that of projecting the values in the image over real space at the correct tilt angle [61]. When all the transformed projections are backprojected over the same volume, the highest values in the volume correspond to a (flawed) version of the object.

The first reconstruction technique used when tomography was developed, referred to as the Fourier method, was a direct inversion of the Fourier slice theorem [64]: the projections were Fourier transformed, then the Fourier transforms were inserted at the correct angles around the tilt axis, without backprojecting. This 3D ensemble was interpolated radially to fill the gaps in data between projection angles, then inverse Fourier transformed to produce the reconstruction. This is less successful when used with a limited number of views than the subsequently developed techniques of backprojection and

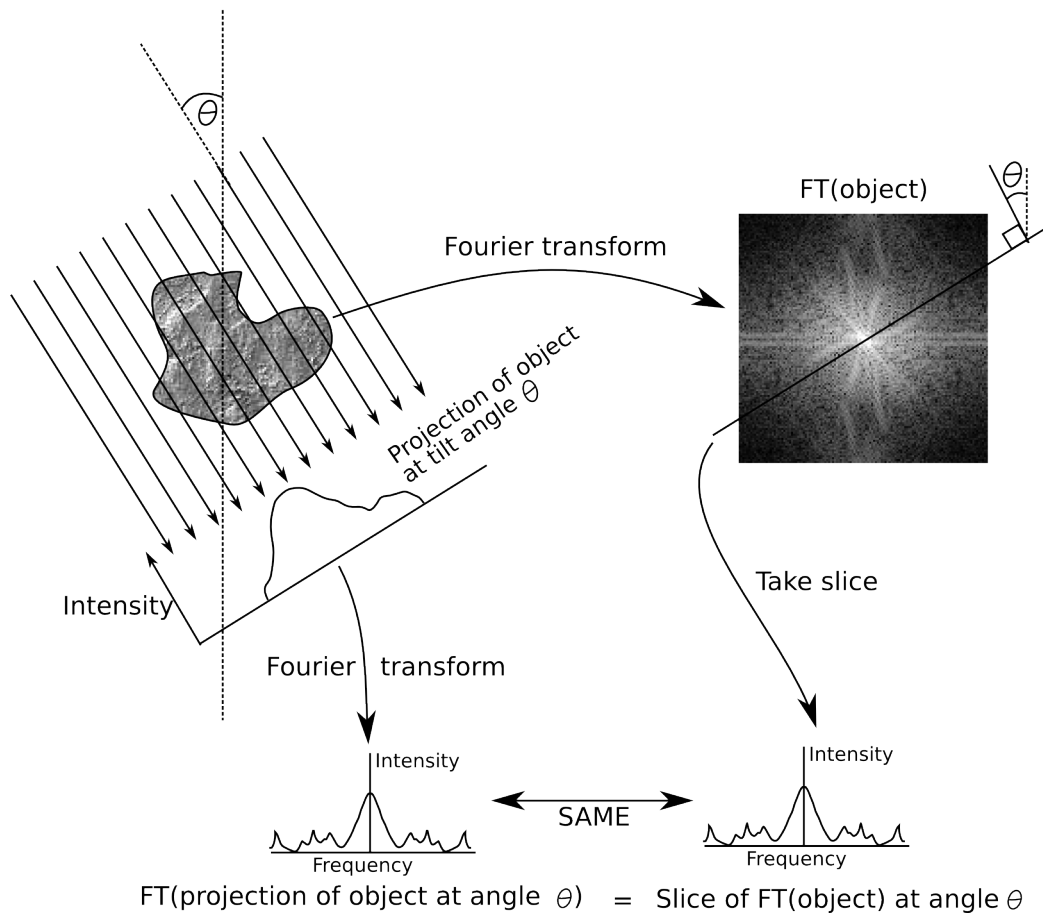


Figure 2.3: The Fourier Slice theorem: a projection of an object through direct space (left) is equivalent to the Fourier transform of a section through the object's Fourier transform (right) at the same angle with respect to u , the spatial frequency axis.

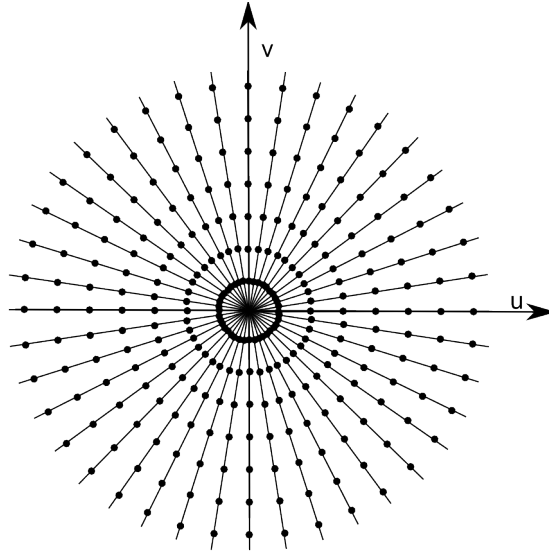


Figure 2.4: Schematic to show how building a volume with regularly sampled projections results in data of lower density at higher frequencies. Lines represent slices of Fourier space that correspond to projections according to the Fourier slice theorem, points on the projections correspond to regular sampling points, becoming sparser at higher frequencies further from the origin of Fourier space.

algebraic reconstruction [65], so is not suitable for this work.

2.3.2 Weighting

Simple backprojection does not impart all of Fourier space with equal density of coverage: if sampling points are distributed evenly along the lines of backprojection, the data is less dense further from the origin of Fourier space (Figure 2.4). This corresponds to the data being of lower density at higher spatial frequencies; the fine details are weakened. This poses a particular problem when reconstructing dislocation structures that are composed mainly of fine detail.

The problem is partially solved by applying a Fourier-space **weighting filter** to the data [66]. The weighting filter at a given radius in Fourier space corresponds to the separation of sampling points on neighbouring projection lines at that frequency w , given in Equation 2.2 where N is the number of

projections and Θ is the tilt range in radians.

$$f \approx \frac{\Theta |w|}{N} \quad (2.2)$$

It is not possible to inverse transform a function that extends out to infinity, and a filter that is greatest at the highest frequency will enhance shot noise more than the features in the image, so the filter function is actually one which reverts to zero at some frequency less than the highest frequency of the data [61]. It is better to do this using a soft-edged cutoff rather than a sudden cutoff in the filter at the highest frequency, so as not to introduce edge effects. The final weighting filter f is multiplied by the Fourier transform of each projection before the product is inverse Fourier-transformed and backprojected to add to the reconstruction.

2.4 Reconstruction by algebraic reconstruction techniques

Algebraic reconstruction techniques give reconstructions with less residual arcing around pointlike features than is seen in the results of weighted backprojection. Most final reconstructions in electron tomography for materials science are done using algebraic techniques. A test reconstruction is made with backprojection to check alignment (typically, this takes approximately 10 minutes after alignment) and then when the alignment is optimised, an algebraic reconstruction is done, which generally takes several hours.

Algebraic reconstruction techniques are based on the initially quite surprising idea that a reconstruction problem can be represented as a matrix equation of the form $\mathbf{Ax} = \mathbf{b}$; the correspondence between these is explained in Figure 2.5.

If the images were all exactly correct representations of the object according to $\mathbf{Ax} = \mathbf{b}$, the equations describing the projections would have a common solution, and this could be found by simply finding and inverting

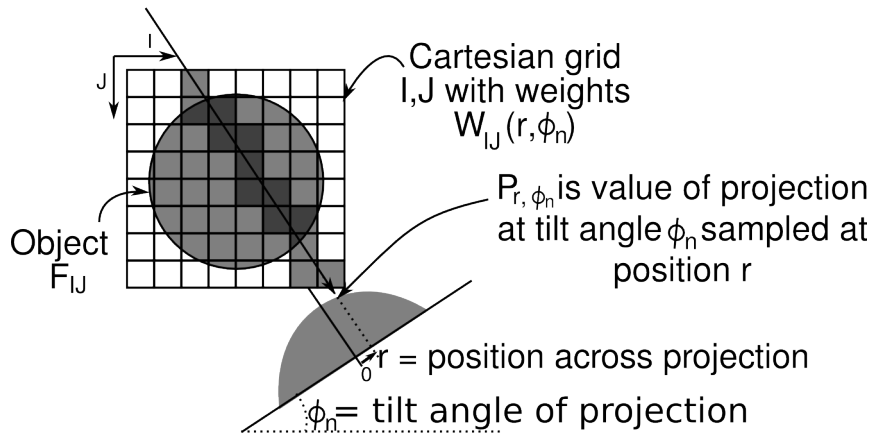


Figure 2.5: The tomography problem as seen for algebraic reconstruction techniques, n^{th} projection $P_{r, \phi_n} = \sum_{I=1}^M \sum_{J=1}^M W_{IJ}(r, \phi_n) F_{IJ}$ with terms as shown in diagram. In matrix form $\mathbf{Ax} = \mathbf{b}$, vector \mathbf{x} (unknown) contains the property being measured for each point in space (e.g. mass-density, appropriate function of displacement field) with each element of the vector corresponding to a position I, J . The vector \mathbf{b} corresponds to the measurement data, P_{r, ϕ_n} . The matrix relating them \mathbf{A} represents the weightings that are used to reproduce the measuring process, $W_{IJ}(i, \phi_j)$. Generally \mathbf{A} is quite sparse, because only points within a ray contribute to the pixel at the end of the ray, so all elements of \mathbf{A} that relate an image pixel in \mathbf{b} to parts of the object off its ray-path are zero. Each projection image represents an equation inside this matrix.

A. This is not the case for two reasons:

- The images are not exactly correct representations of the object: they contain noise that is uncorrelated between images, and there is no common solution
- An array made of all the equations is so large with so many dimensions (as many as there are volume samples of the object) that it would take an unfeasible amount of computer time and RAM to perform the matrix inversions needed to solve all the equations in it, even if there was a unique solution.

The best that can be done is to find the nearest thing to a unique solution — and this is done using a very tailored least squares approach. An initial estimate of the object is made, either a backprojected reconstruction or a constant level — usually zero or the mean intensity of the tilt series — and projections of the ‘object’ are calculated for the same tilt angles as the data. A difference array is calculated between the projections of the ‘object’ and the real images. This difference array is then imposed onto the previous ‘guess’ reconstruction, correcting it. In this way algebraic techniques are often used as a further stage of refinement of a backprojected reconstruction. One round of calculating projections of the developing reconstruction, comparing to the images and applying difference corrections is an iteration; as more iterations are performed, a solution is generally converged upon. The corrections can be applied in different ways, giving two variations of the technique [61]:

Algebraic Reconstruction Technique (ART): In ART, the difference array for a projection is imposed on the developing reconstruction directly after it is calculated for that projection. For reconstruction value ρ at position (i, j) during iteration q , the correction factor based on the k^{th} ray at angle θ for projection image data $P_{k\theta}$ and projection of the reconstruction $R_{k\theta}^q$ is applied as Equation 2.3 [67]:

$$\rho_{ij}^{(q+1)} = \frac{P_{k\theta}}{R_{k\theta}^q} \rho_{ij}^q \quad (2.3)$$

Rapid convergence is possible in low noise conditions, but when noise is significant it is less successful. Noise is less correlated between images than the object, so background pixel positions experience proportionally large intensity variation between images when there is significant noise. This sharp variation between images on a very fine scale impairs convergence of ART.

Simultaneous Iterative Reconstructive Technique (SIRT): In SIRT, the corrections from all projections are stored up until the end of one iteration, combined, then the combined correction is applied [65]. The correction factor can be expressed algebraically with the same parameters and $N_{k\theta}$ the number of volume elements in ray k , projection angle θ and $L_{k\theta}$ the ray length for tilt angle θ , as Equation 2.4 [67]:

$$\rho_{ij}^{(q+1)} = \frac{\sum_{k,\theta} P_{k\theta} \sum_{k,\theta} N_{k\theta}}{\sum_{k,\theta} L_{k\theta} \sum_{k,\theta} R_{k\theta}^q} \rho_{ij}^q \quad (2.4)$$

Corrections can be a simple mean of the stored corrections (additive approach) or the normalised product of the stored corrections (multiplicative approach) as in Equations 2.3 and 2.4. Combining the corrections smoothes out the inconsistency and reduces the speckle noise, but in some cases, under low noise conditions, SIRT does not converge to as close a best solution as ART. The images in dislocation tomography are not low noise images, so SIRT is better for dislocation tomography.

The expressions given above are for correction schemes that multiply by the developing reconstruction; additive correction schemes are also possible but omitted here for clarity as they were not chosen in these experiments.

2.5 Other reconstruction techniques

There are other techniques used in tomographic reconstruction than those described in detail here. Some of these will be briefly described.

2.5.1 Maximum entropy techniques

Maximum entropy is a class of computational technique applied to a wide variety of problems; generally, constraints are imposed on the system and it is allowed to iteratively find the most probable solution that fulfils the constraint according to which has the maximum informational **entropy**, $S = -\sum p_{ij} \ln p_{ij}$ for solution parameters p_{ij} . In the case of tomography, the constraints imposed are that projections of the trial structure must differ as little as possible from the images in the tilt series according to a given noise model [68]. An attractive feature of this technique is that there is no limit on the frequency of data that can be used reliably.

For dislocation tomography it would be intriguing to attempt this technique with the added constraints of the general rules of dislocation behaviour, such as that dislocation lines may not start in the middle of the crystal [1] or the general pattern of dislocations in the sample. This has not yet been tried at the time of writing.

2.5.2 Discrete tomography

Discrete tomography can be applied to algebraic reconstructions of samples that have a number of distinct region types producing different grey levels in the images and reconstruction. The initial algebraic reconstruction is smoothed and re-reconstructed around the boundaries between regions, giving a result that shows the different regions clearly and with less arcing around features. It has been used successfully on experimental datasets in materials science [69]. Discrete tomography appears an ideal technique for determining the path of dislocations by separating the reconstruction into dislocation and non-dislocation regions. The authors of the discrete tomography algorithm presented in reference [69], among them Joost Batenburg and Sara Bals, attempted to use this algorithm to reconstruct from the tilt series of weak-beam dark-field images of dislocations in GaN, but did not meet with success at an initial attempt because of the variations in background intensity. Application of the image processing techniques used for conventional tomography could make future attempts successful; this is

yet to be pursued.

2.6 Limitations of electron tomography

2.6.1 The missing wedge

The transmission electron microscope brings a physical limitation to tomography - the **missing wedge**. There is a restriction on how far the specimen can be tilted inside the microscope while taking a tilt series:

- The specimen is held in the narrow gap between the upper and lower polepieces of the objective lens, and even a thinned conventional specimen holder cannot be tilted more than $\approx 80^\circ$ before it touches the polepieces, reducing the angular range to 160° — from $+80^\circ$ to -80° .
- A disc-shaped specimen in the traditional form of holder can be obscured by the specimen holder at high tilt, $\approx 85 - 90^\circ$.
- At some angle depending on the morphology and material of the specimen, the projected thickness of the specimen becomes too thick for the defects inside to be seen, as the diffracted beams are lost to absorption in the thickness of perfect crystal.

This limited range of tilt causes a wedge of missing data. This produces artifacts in the reconstruction; reconstructed objects are elongated parallel to the optic axis by a factor e given in Equation 2.5 in which θ_{max} is the maximum tilt angle obtained [70].

$$e = \sqrt{\frac{\theta_{max} + \sin \theta_{max} \cos \theta_{max}}{\theta_{max} - \sin \theta_{max} \cos \theta_{max}}} \quad (2.5)$$

The effect of the missing wedge on the reconstruction can also be represented in Fourier space. Figure 2.6 is the Fourier space representation of projection data pictured in Figure 2.4 (dots representing sampling points removed for clarity), but altered to show the missing wedge.

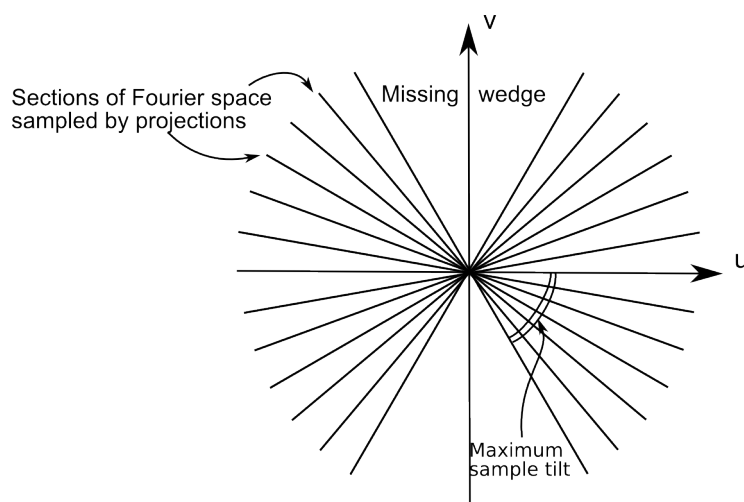


Figure 2.6: Diagram showing the effect of restricted tilt angle on the ability to fill up Fourier space with data about the object. Lines plotted on these u - v spatial frequency axes are slices through the object's Fourier transform that are equivalent to the projections in direct space, by the Fourier slice theorem.

The missing wedge can be minimised by maximising the tilt range of images; this can be done by using a specially thinned tomography holder, as used for these experiments. With the advent of aberration corrected lenses, it may soon be possible to have a much larger polepiece gap, though at present this technology has concentrated on improving high-resolution work and the possibility of larger polepiece gaps is yet to be thoroughly explored. Alternatively, specimen holders are available that hold a needle-shaped specimen by one end and can be rotated 360° , such as the Fischione 2050 on-axis rotation tomography holder [71]. This allows the missing wedge to be eliminated, if suitable specimens can be prepared from the material studied; however, use of a focused ion beam is generally required for this, which in some samples creates artifacts at the surface (such as dislocation loops in metals or amorphous layers in semiconductors) that may obscure the dislocations inside (Section 1.3).

2.6.2 Minimum reliable spacing of features

Using the Fourier method of reconstruction, there is a limit on the size of reliable features in the reconstruction, imposed by the decrease in Fourier-space density of data as the frequency increases (as in Figure 2.3). The Fourier method of reconstruction begins by interpolating and reconstructing at the lowest frequency, and works outward in Fourier space. At some critical frequency, the density of data becomes insufficient to supply enough Fourier coefficients to describe features at that frequency [64]. If reconstruction is continued beyond that frequency using the Fourier method, false detail is generated in the reconstruction.

For this reason it was important to find this critical frequency, so one could stop the process when it was reached. This smallest reliable spacing is given by Equation 2.6 [64], in which D is the size of the particle being reconstructed and m is the number of projections taken. The parameter D is a little misleading; when this was derived in Crowther's paper [64], D was introduced to decide the necessary spacing $1/D$ of samples in the image plane (pixels) needed to avoid aliasing effects from undersampling.

$$d = \frac{\pi D}{m} \tag{2.6}$$

For the weak-beam tilt series of 31 images taken from TiAl presented later in in this thesis, which is 1024×1024 pixels (the reason for using pixels and not length units will be explained later) this gives 104 pixels as the minimum size of feature that can be reconstructed reliably — this is comparatively large, roughly ten times the dislocation image width. For non-evenly spaced projections (e.g. when there is a missing wedge), this limit becomes larger still.

The question of whether this applies to backprojection and algebraic reconstruction techniques is an important one when reconstructing thin features such as dislocations, with small changes such as jogs or kinks in them. If it did, this would present a significant problem, because the algebraic techniques normally used to produce final reconstructions do not work up through frequency as they reconstruct, but from the beginning

use the data down to pixel detail; a reconstruction will be produced with detail equal to pixel size, but below a certain scale this detail may be false. Conversely, it can be seen in these reconstructions that details smaller than ten times dislocation width are reconstructed in a way that still resembles the dislocation structures seen in the sample; they cannot be wholly unreliable, but may fall on a continuum of reliability.

Approaching the problem from another angle, Norton [72] adapted algebraic reconstruction algorithms to continuous forms in order to analyse their convergence, and found that different frequencies converge to the closest solution at different rates. He found the Fourier transform of a SIRT reconstruction at iteration n , $F^{(n)}(\rho)$, is related to the object's Fourier transform $G(\rho)$ by Equation 2.7, where λ is a dimensionless feedback parameter chosen arbitrarily, but usually taken between 0 and 2; here it will be used with value 1; L_0 is the length of rays used across the projection, ρ is frequency.

$$F^{(n)}(\rho) = G(\rho) + [F^{(0)}(\rho) - G(\rho)] \left(1 - \frac{\lambda}{\pi L_0 \rho}\right)^n \quad (2.7)$$

Norton elaborated that if the initial 'guess' structure before iteration starts is all zero, the reconstruction's Fourier transform at iteration n simplifies to the real structure's Fourier transform $G(\rho)$ multiplied by a **transfer function** as in Equation 2.8. A transfer function of 1 denotes perfect representation in the reconstruction; a transfer function of 0 represents complete absence of that frequency in the reconstruction. Norton's transfer function for SIRT is plotted in Figure 2.7.

$$F_{SIRT}^{(n)}(\rho) = G(\rho) \left(1 - \left[1 - \frac{\lambda}{\pi \rho L_0}\right]^n\right) \quad (2.8)$$

Frequencies and lengths are plotted in 1/pixels and pixels rather than absolute length and frequency, because the important parameter for the reconstruction algorithm is the size of the object relative to the whole image; the reconstruction algorithm does not 'know' whether the object was 100 nm or 1 nm across, only how many pixels it takes up. As a result this transfer

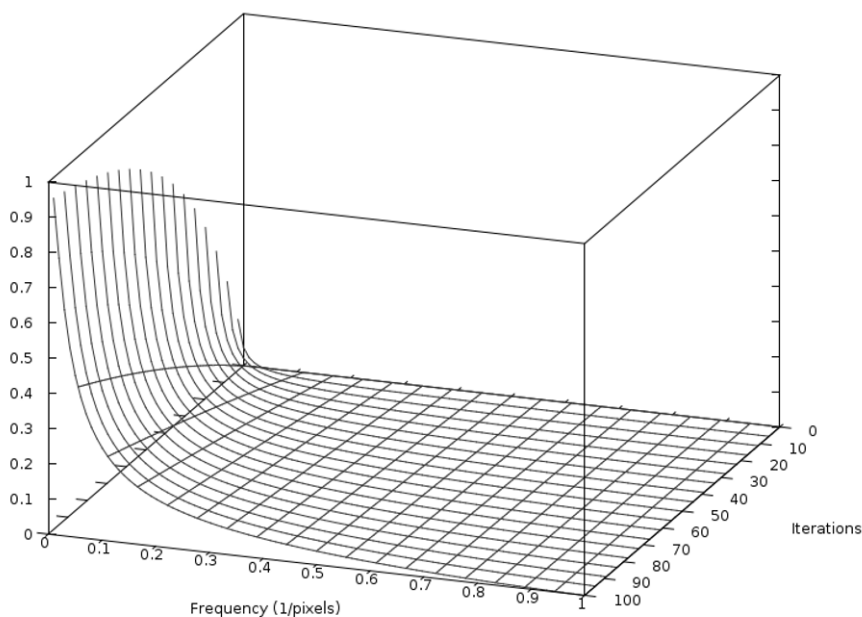


Figure 2.7: Plot of the transfer function of SIRT depending on frequency and number of iterations completed, for images of 1024×1024 px. Transfer function is the multiplier between the real structure and the reconstruction at iteration n , if the starting point of SIRT was zero. Reconstructions in this work start not from zero but from a rough backprojected reconstruction; this should push the steep part of the curve toward higher frequencies and smaller numbers of iterations, widening the domain for which a successful reconstruction might be expected.

function plot can be applied to a tilt series of any magnification that has images of 1024×1024 pixels (the length input for L_0), which is the size of images generally used for tomography by the HREM group as a compromise between large image size with slow reconstruction, and small image size with poor reconstruction quality.

Figure 2.7 shows that SIRT attenuates higher frequencies, and this only improves slowly as more iterations are completed. At the time of writing, 20 iterations of SIRT on a $1024 \times 1024 \times 1024$ volume takes eight hours to run on a desktop PC running FEI's *Inspect3DTM* under Windows XP; a fivefold increase in the number of iterations would only give a small improvement in the transfer function of small objects. A suitable measure of technique-

imposed resolution might be the halfway point in the fall-off of transfer function; for 20 iterations this is for a frequency of around $0.05px^{-1}$. To properly represent an object of size t , Fourier components of up to $1/2t$ are required [73], so this corresponds to an object of size 10 pixels. The Fourier method's limit, 104 pixels, falls at $0.01px^{-1}$, where the transfer function is nearly at its highest; much more conservative than SIRT's apparent practical limits. This makes some sense; a SIRT reconstruction has more *a priori* information than reconstructions from the Fourier method, in the form of the restriction that each pixel must be a ray-sum, which is not applied in the Fourier method for which that limit was derived.

If the SIRT transfer function model is correct, it strongly indicates that the best approach for tomography of a fine-scale object such as a dislocation is to use a higher magnification and make a montage of smaller reconstructions (in which the small object takes up more pixels), rather than one large reconstruction in which the objects are small.

To test this, an object of size $128 \times 256 \times 128$ pixels was used with the 'density' distribution shown in Equation 2.9.

$$P = 1000 \exp \left[-\frac{(z - 64)^2}{2 \times 5^2} \right] \exp \left[-\frac{(y - y_m)^2}{2 \times 5^2} \right] \cos \left(\frac{2\pi mx}{128} \right) + 1000 \quad (2.9)$$

At specific values of y denoted by y_m , $\cos mx$ type functions of successively higher frequency were used (i.e. with m periods across the x dimension of the object), for $m = 2, 4, 8$ and 16 , with peak height $P = 2000$, trough height $P = 0$. In the z and y directions the density faded off as a Gaussian curve so as not to introduce sharp edges (high frequency components). Two sections through the test object are shown in Figure 2.8. A tilt series of images was simulated from the test object, using a simple Radon transform with y as the tilt axis and z as the plane normal for zero tilt.

The 2D Fourier transforms of the test objects taken at the relevant $y = y_m$ planes have spikes in magnitude at the x -direction frequencies $2/128, 4/128, 8/128$ and $16/128 \text{ px}^{-1}$. These are all of the same magnitude, as shown in Figure 2.9, because the cosine functions were all of the same amplitude.

The test object was reconstructed using SIRT in *Inspect3DTM* with

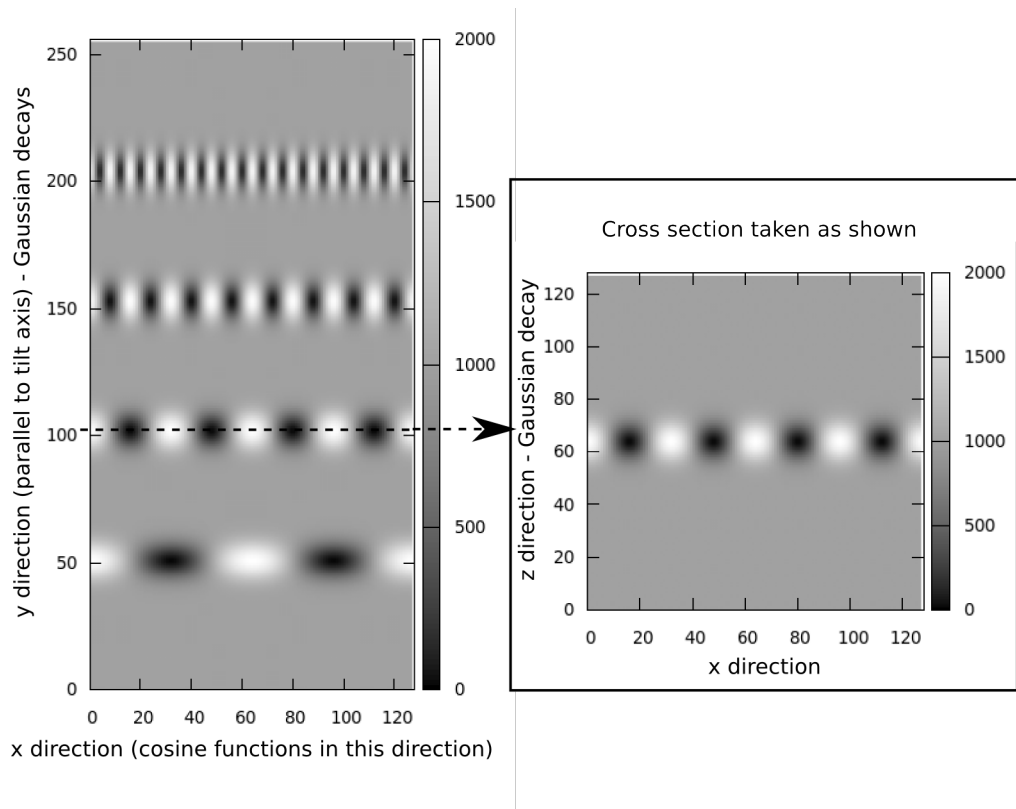


Figure 2.8: Test object used to characterise the frequency response of tomography reconstruction using SIRT. Left: section on the xy plane of the object. i.e. the same angle as for a zero tilt image, taken at $z = 64$, i.e. the peak of the Gaussian distribution in z . Right: section in the $y = y_m$ plane taken through the cosine function with 4 periods across the image ($m = 4$, frequency $4/128\text{px}^{-1}$).

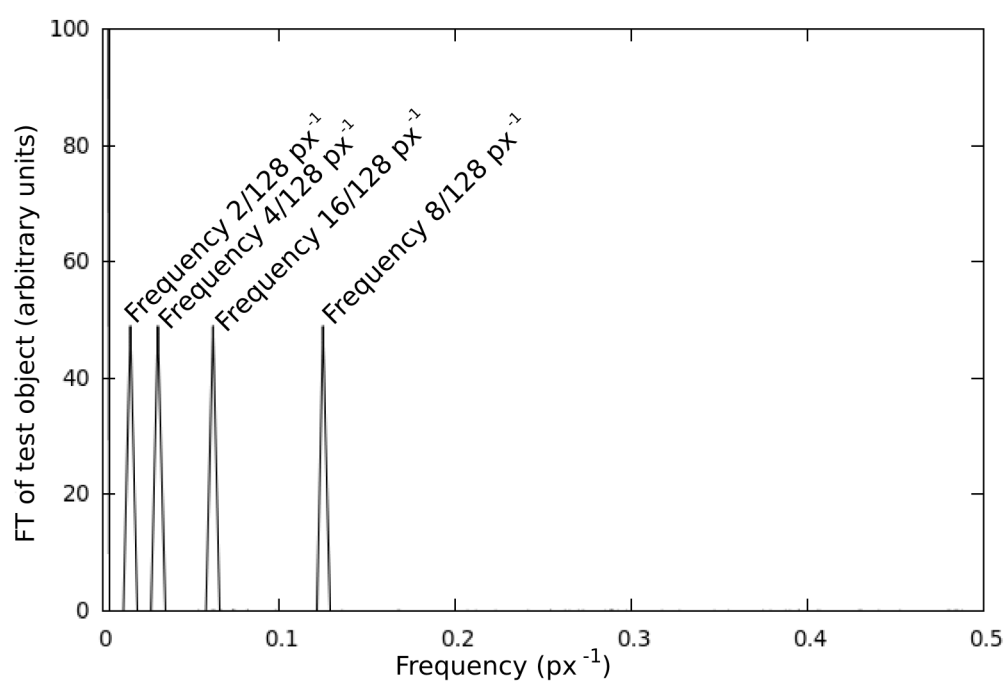


Figure 2.9: Plots of the magnitude of the 2D Fourier transform of the test object, taken along the x-direction; the plots from all four cosine gratings are superimposed on the same axes. The peaks corresponding to the cosine functions are all of the same magnitude.

30 iterations. Sections through the resulting reconstruction are shown in Figure 2.10. 2D Fourier transforms at the positions of the cosine fringes were taken as before, and the magnitudes of these in the x -direction are plotted in Figure 2.11. The Fourier transform magnitude at the peaks corresponding to the different frequency cosine fringes, falls off with increasing frequency as predicted, but appears to level off as it decreases.

The transfer function of the Inspect3DTM implementation of SIRT cannot be characterised directly because internal rescaling makes the values of the input and output not comparable. The input images are rescaled in intensity to the range of 2-byte integer values (32,768 to +32,767) before alignment and reconstruction are performed, and the reconstructed ‘density’ distribution is rescaled to the same range before writing out. The actual ratio between the ‘density’ of the same component in the input and output data is lost, so the transfer function cannot be calculated directly.

The frequency response can however be analysed indirectly through the ratio between different frequency components in the reconstruction. In this case where the four frequency spikes are of the same magnitude to begin with, taking a ratio between the strength of two frequency components gives the expression in Equation 2.10; $F(m\rho)$ is the magnitude of the Fourier transform at frequency $m\rho$ (for integer m), other terms are given in Equation 2.8. The object function’s Fourier transform has cancelled out from the top and bottom of the fraction leaving only the transfer function to affect the ratio.

$$\frac{F(m\rho)}{F(\rho)} = \frac{1 - \left[1 - \frac{1}{\pi L_o m \rho}\right]^n}{1 - \left[1 - \frac{1}{\pi L_o \rho}\right]^n} \quad (2.10)$$

The magnitudes of peaks in the Fourier transforms corresponding to the different frequencies were divided by the magnitude for the lowest frequency, $2/128px^{-1}$. These are given in Table 2.1 next to the ratio predicted from Norton’s transfer function, calculated using a program written for the purpose in C. The ratio appears to fall more quickly with increasing frequency than the transfer function predicts, but then levels off at a higher value than predicted as frequency increases.

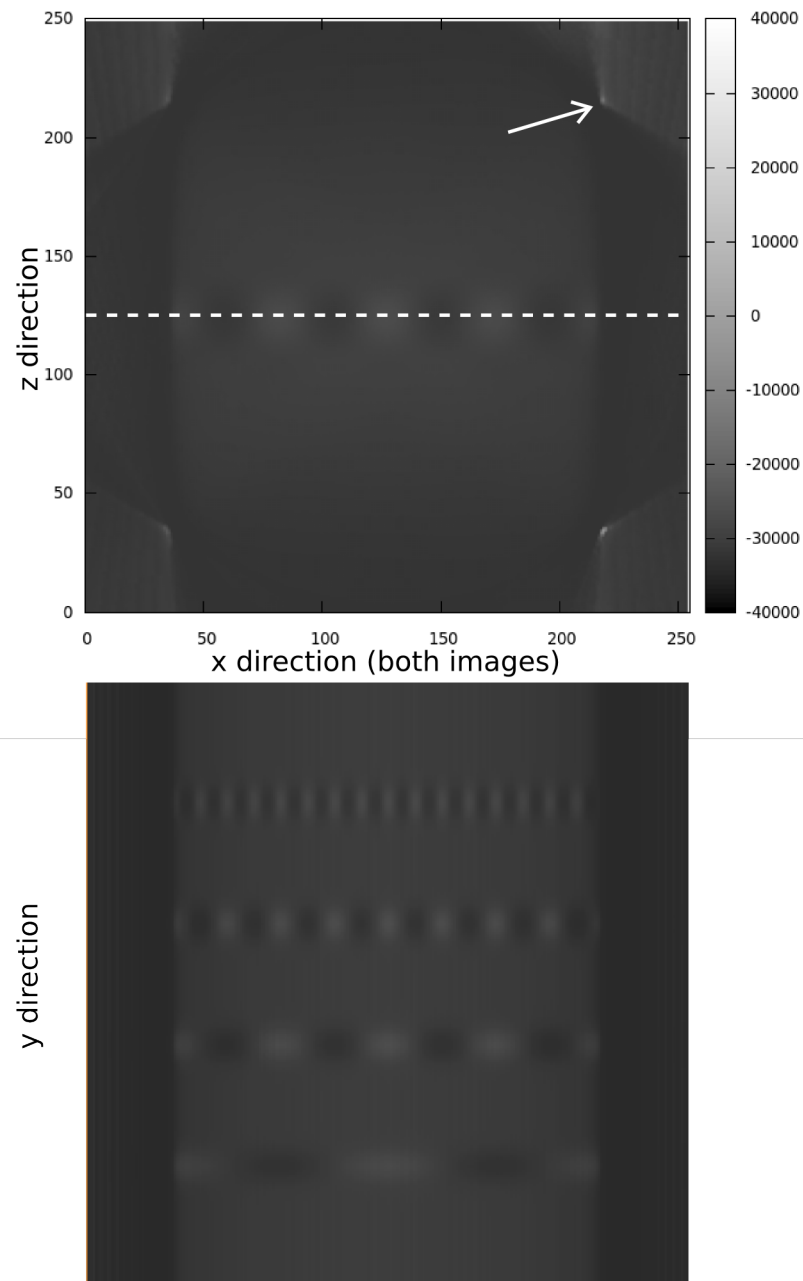


Figure 2.10: Reconstruction of the test object shown in Figure 2.8. Top: $y = y_m$ section taken at the same cosine function as in Figure 2.8. Arrowed are strong artefacts from backprojection of the edge of the volume that dominate the reconstruction's 'density' range.

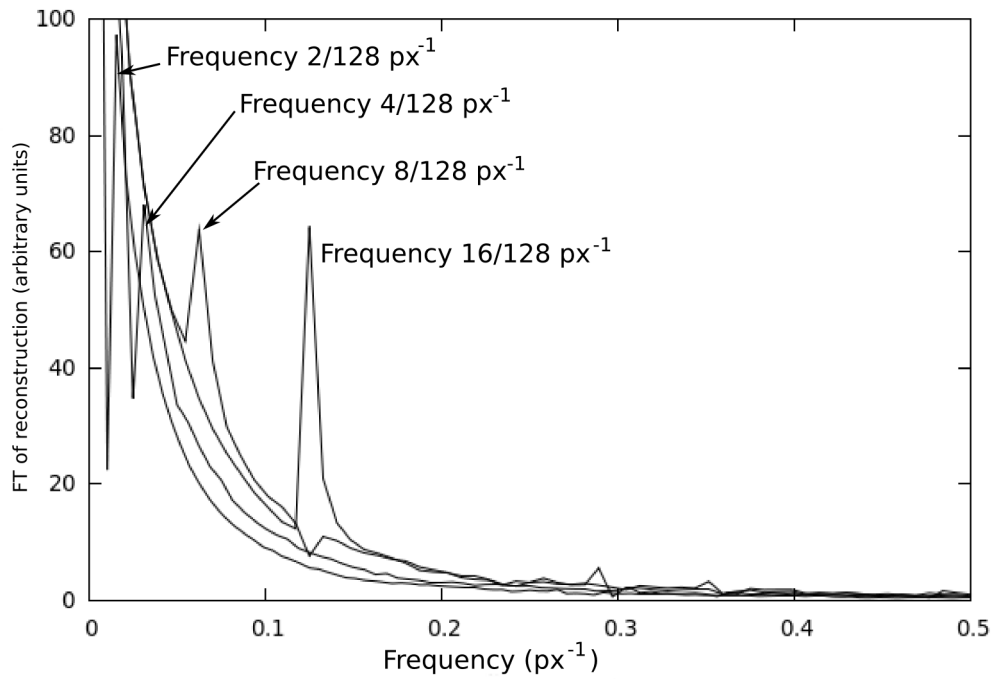


Figure 2.11: The Fourier transforms of the four cosines in the reconstruction, superimposed on the same axes. The peaks corresponding to increasing cosine frequencies fall off rapidly in magnitude and then level off; this form is as expected from Norton's transfer function, but the rate at which it occurs is not. The small peak at $\sim 0.28 \text{ px}^{-1}$ probably corresponds to the fringes introduced near the boundaries of the volume from the test object edges, seen at the sides and corners in Figure 2.10.

| m in $\cos(2\pi mx/128)$ | Frequency $\text{px}^{-1} \times 10^{-2}$ | Predicted ratio $I/I_{m=2}$ | Measured ratio $I/I_{m=2}$ |
|-------------------------------|--|--------------------------------|-------------------------------|
| 2 | 1.56 | 1.0 | 1.0 |
| 4 | 3.16 | 0.921 | 0.700 |
| 8 | 6.25 | 0.708 | 0.655 |
| 16 | 12.5 | 0.455 | 0.661 |

Table 2.1: Comparison of ratios between different frequency components after reconstruction of a test object with four cosine gratings of equal amplitudes and power-of-two frequencies. Ratios predicted by Norton’s transfer function penalise higher frequency components more than this test appears to show. The attenuation of higher frequencies appears to level off with a higher transfer coefficient than expected from the predicted transfer function, though this is too small a data set to be certain.

The conclusion from this test is that higher frequencies *are* attenuated by tomographic reconstruction, but (except for a rapid fall at low frequencies) not as much as predicted by Norton’s transfer function. The real transfer function appears to converge to ~ 0.66 for higher frequencies. The implication for dislocation tomography is that such small, finely-spaced objects as dislocations are unlikely to be attenuated as much as might be expected in a large reconstruction.

One reason for high frequencies being attenuated less than expected, could be that the initial estimate structure given to SIRT in the Inspect3DTM implementation is a backprojected reconstruction, not a uniform array of zero, as assumed in the derivation of the transfer function [72]; this difference in the method may give a strong improvement in the success in reconstructing small objects. This test only sampled four frequencies, however, and more rigorous tests could be done to check the results.

Chapter 3

Tomography of dislocations using weak-beam dark field images

3.1 Basis of the weak-beam dark field (WBDF) technique

The weak-beam dark field technique gives a narrower dislocation image than a dark field image made from a simple two-beam diffraction condition (with the bright field and one dark field reflection excited), so is commonly used to obtain the best resolution when imaging dislocations. Before this is explained in detail, the main theories of electron microscopy relevant to this work will be introduced.

3.1.1 Dislocations in the kinematical theory of electron diffraction

The kinematical theory of electron diffraction applies to a two-beam condition when the dark field beam does not return significant intensity to the bright field beam [3]. When using this theory to describe dislocation images, the column approximation is often assumed: the amplitude ϕ_g of

the electron wave at depth z is found by integrating the scattering from matter in a thin column reaching parallel to the incoming beam direction. It is assumed there is no dispersion of the beam out of this column — the **column approximation**. This is a valid assumption for a distorted crystal, if the displacement field \mathbf{R} changes only slowly across the image between columns.

If no electron flux is lost from the system by other excited beams that are stopped by an aperture (**absorption**), or through inelastic scattering, within a two-beam approximation the amplitude ϕ_g at the bottom surface of the TEM film with defects causing displacement field $\mathbf{R}(\mathbf{r})$, is then given by Equation 3.1 [3], [74]:

$$\phi_g = \frac{i\pi}{\xi_g} \int_0^t \exp(-2\pi i \mathbf{g} \cdot \mathbf{R}) \exp(-2\pi i s z) dz \quad (3.1)$$

Here t is the thickness of the film along the incident beam z , s is the excitation error, ξ_g is the extinction length for the beam \mathbf{g} . Qualitatively, a bright line is produced against a dark background, tracing a path to one side of the dislocation core. Some terms in the two-beam equation require further explanation as they are important concepts in the weak-beam dark field technique.

Excitation error

This is best illustrated using the Ewald sphere construction, shown in Figure 3.1. This sphere has a radius k related to the wavelength of the incident electrons, $k = 1/\lambda$; it is superimposed on the reciprocal lattice of the crystal structure, with the incident beam direction marked. The reciprocal lattice points are sinc functions in cross section; the central maxima of these, elongated by the shape factor of the very thin specimen, are referred to as reciprocal lattice rods. If the Ewald sphere passes through or close to them, they appear on a recorded diffraction pattern and can be used. The excitation error for a reflection \mathbf{g} , usually given the symbol s_g , is the vector joining the centre of the reciprocal lattice rod \mathbf{g} to the Ewald sphere. The scattering

wavevector relevant to that diffracted beam is then $\mathbf{K} = \mathbf{g} + \mathbf{s}$. If \mathbf{g} is ‘inside’ the Ewald sphere, i.e. \mathbf{s} points in the same direction as the incident beam, \mathbf{s} is positive [32]. As the z component of \mathbf{s} is by far the largest in most cases, it is often simplified to the scalar s_z or just s .

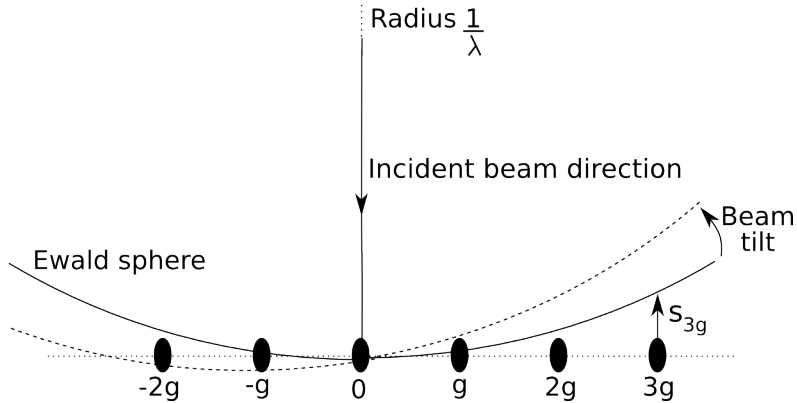


Figure 3.1: Section through the Ewald sphere reconstruction, taken along a systematic row of reciprocal lattice points: $0, \mathbf{g}, 2\mathbf{g}, 3\mathbf{g}, \dots$. The central maxima of the reciprocal lattice rods are drawn in cross-section at the lattice points, elongated in the foil normal direction due to the shape factor. Excitation error for $3\mathbf{g}$ is shown. As the beam is tilted with respect to the crystal, the Ewald sphere tilts with respect to the reciprocal lattice (dashed curve) and the excitation errors of the beams change.

Extinction length

The extinction length properly belongs to the dynamical model; the kinematical approximation is a simplified case that makes use of this parameter. In the dynamical two-beam approximation, as the electron wave propagates through the crystal, amplitude is transferred from the incident beam to the diffracted beam until it is mainly in the diffracted beam, then it is transferred back again, and the process repeats until the exit surface is reached. For diffracted beam \mathbf{g} , one cycle of this occurs while the beam travels over distance ξ_g within the crystal. It can be shown that the extinction length is given by Equation 3.2 [3] in which V_c is the unit cell volume and F_g

is the structure factor for reflection \mathbf{g} at Bragg angle θ_B from wavelength λ .

$$\xi_g = \frac{\pi V_c \cos \theta_B}{\lambda F_g} \quad (3.2)$$

If the specimen is significantly thinner than ξ_g , it can be assumed that intensity is not transferred back to the incident beam before the exit surface is reached ($I_o \gg I_g$) and the kinematical theory is reasonable.

3.1.2 Dislocations in the dynamical theory of electron diffraction

If intensity is redistributed from the incident to the diffracted beam(s) and back again, the kinematical theory is no longer accurate and the dynamical theory of electron diffraction must be used. This is the case if the excitation error s is small (the dark field imaging reflection is close to Bragg condition and strong), many diffracted beams are excited and can draw intensity from the incident beam, and/or the sample is thick. In reality all electron diffraction is dynamical, but the kinematical theory is a convenient simplification that can be used when s is large or the sample is much thinner than ξ_g . The dynamical theory treats the electron wave as entering wave states with the same periodicity as the crystal (**Bloch states**) as it passes through the sample, and being redistributed between states by the potential of the crystal and the defects within it, to produce exit wavefunctions characteristic of the sample.

In general, the dynamical dark field dislocation image appears similar to the kinematical dislocation image — a line to one side of the dislocation core, with a profile dependent on which dark-field reflection is used. The dynamical theory explains additional features not fully explained by the kinematical theory that are produced by the beating of different Bloch waves, such as fringe contrast in dislocations that are inclined to the crystal surface, and dislocations having different contrast where they meet the top and bottom surfaces [3].

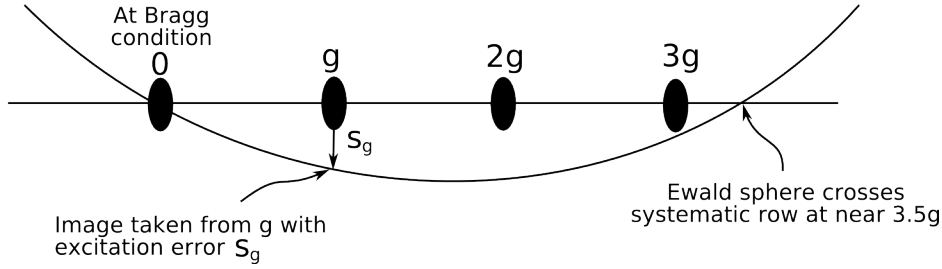


Figure 3.2: Intersection of the Ewald sphere with the plane containing the ng systematic row, showing the basis of the weak-beam dark-field technique for the case $n \approx 3.5$.

3.1.3 The weak-beam dark field technique

The weak-beam dark field (WBDF) technique was developed by Cockayne, Ray and Whelan in 1968 [75]. In this technique the crystal is tilted slightly away from a two-beam condition, so that higher order reflections of form $N\mathbf{g}$ are excited in a systematic row. The dark field image is taken from a weakly excited reflection in this row, see Figure 3.2. In this example the weak-beam condition would be expressed as $\mathbf{g}(3.5\mathbf{g})$: the term outside the brackets is the weak diffraction spot used to take the image, the term inside is the position along the systematic row that is at Bragg condition, i.e. where the Ewald sphere crosses the row.

WBDF images are more kinematical than simple two-beam dark field images, because the dark field imaging beam is not strongly excited. When the Bragg condition point $n\mathbf{g}$ is known, the deviation parameter s_g of the image beam \mathbf{g} can be calculated using Equation 3.3 [32, Ch.26]. The WBDF technique gives a narrower dislocation image and thus complex dislocation structures are better resolved [76].

$$s = \frac{1}{2}(n - 1)|g|^2\lambda \quad (3.3)$$

The position of a dislocation image from the dislocation core \mathbf{r}_0 can be approximated by Equations 3.4, which give the position where maximum

amplitude of the dark field beam g occurs, under kinematical conditions [75].

$$\begin{aligned}
 s_g + \mathbf{g} \cdot \frac{d\mathbf{R}}{dz} &= 0 \\
 \text{at the turning point in } \mathbf{g} \cdot \frac{d\mathbf{R}}{dz} & \\
 \text{i.e. where } \mathbf{g} \cdot \frac{d^2\mathbf{R}}{dz^2} &= 0
 \end{aligned}
 \tag{3.4}$$

Physically this corresponds to where the planes are bent in the dislocation displacement field just enough to bring them back into the Bragg condition, counteracting the excitation error in the perfect crystal s_g , so that they diffract strongly into the dark-field beam g . This gives a maximum value at that position for the kinematical integral contributing to the amplitude of the dark-field beam [76].

This kinematical approach is not, however, the whole story; in general more than two beams are excited, some of them not weakly, and this requires a ‘many-beam’ dynamical approach to describe the scattering accurately. The error in absolute position of a single dislocation when using the kinematic approximation is $\sim 10\text{\AA}$ in calculated images of dissociated $\mathbf{b} = \frac{1}{2}[1\bar{1}0]$ dislocations in Cu [75]; errors in spacing between two dislocations are relatively smaller because both images are displaced by a similar amount [77]. The larger s , the more appropriate is the kinematical approximation [76].

3.2 Using the WBDF technique for electron tomography

For WBDF tomography, the specimen is aligned in the holder so that the tilt axis of the holder is parallel to the systematic row used for WBDF imaging (Figure 3.3). This requires the use of a specimen holder that can rotate in the plane of the specimen (a tilt-rotate holder). The alignment of the tilt axis must be very fine; any small misalignment causes a change in the diffraction condition as the specimen is tilted. The feature of interest in the specimen must be set at eucentric height — the height at which the specimen can be tilted without the feature moving perpendicular to the tilt axis out of the

field of view. Images are then taken at small angular intervals along the tilt arc, giving a tilt series.

This process requires some interaction with the specimen height. When the specimen is tilted, the height of the feature of interest changes a little, because it is not always possible to get the feature exactly at eucentric height, especially if the dislocations are not all at the same height in the specimen. It is not practical to re-focus using the objective lens because a change in lens strength would rotate the image on the film/detector and change the magnification. Instead the specimen height is adjusted a small amount. This may displace the feature away from eucentric height; this causes a lateral shift of the feature during the next tilt. For WBDF tomography, unlike other imaging modes for electron tomography, shift and focus cannot yet be corrected automatically unless one is fortunate with the specimen, because features such as thickness contours greatly hinder cross-correlation; focus and shift must be adjusted manually at each tilt angle.

The requirement for manual adjustment at every angle, and the difficulty of initially aligning the specimen in the correct diffraction condition, makes WBDF tomography a very labour-intensive task. More images result in a more accurate reconstruction, but the number of images that can be taken is restricted by the stamina of the operator and microscope time available, and how long the specimen can be exposed to the beam before damage obscures the defect being observed. In addition the diffraction condition can only be aligned to limited accuracy and must be checked and restored throughout tilt series acquisition; the effects of misalignment will be explored later in this chapter.

3.2.1 Weak-beam dark-field contrast and the projection requirement

Using conventional backprojection algorithms, for images in a tilt series to be suitable for tomography, they must fulfil the projection requirement (Section 2.1.2): that the contrast is formed from a sum or integral through the specimen, or some other monotonic function of the desired property with

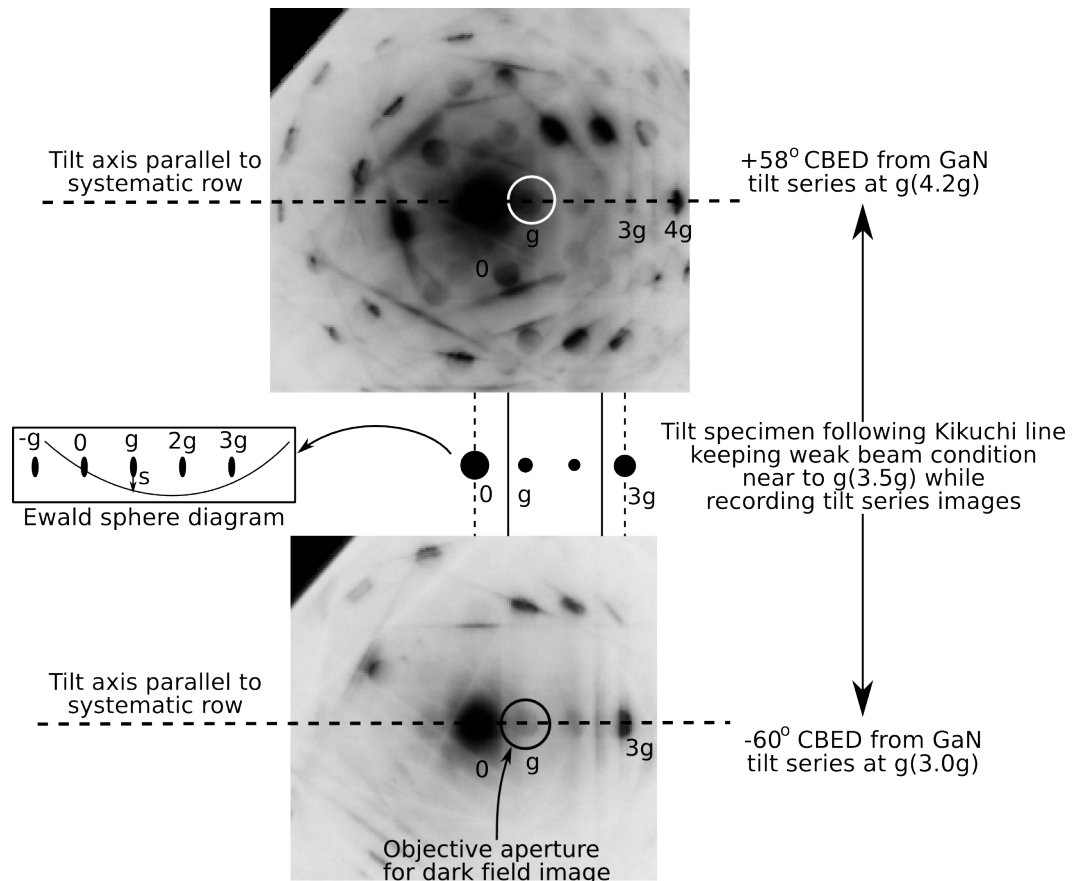


Figure 3.3: The geometry of WBDF tomography. The systematic row for which the weak-beam condition $\mathbf{g}(ng)$ will be set up is aligned parallel to the tilt axis using the rotation control of the tilt-rotate specimen holder, and the beam tilts in dark-field mode are used to set up the weak-beam condition. As the specimen is tilted about the tilt axis, ideally the weak-beam condition is kept and weak-beam dark-field images are recorded from \mathbf{g} at regular tilt angles. In practice the tilt axis and systematic row are not perfectly aligned; the CBED patterns shown here, from either end of the GaN WBDF tilt series, are not at precisely the same diffraction condition.

thickness. Weak-beam dark field contrast is usually modelled assuming the column approximation: the image intensity from a point on the exit surface is given by the square of an integral of the appropriate kinematical or dynamical functions, integrating down the column of crystal along the beam direction. Wherever the column approximation applies, the contrast is some projection, though as will be seen, not necessarily a projection of the intended object.

The column approximation is reasonable to describe weak-beam images of dislocations > 2.5 nm apart (i.e. there is little difference between images calculated with or without the column approximation [76]). For dislocation spacings of ≤ 2.5 nm this is not always the case; for $-\mathbf{g}(3\mathbf{g})$ weak beam conditions, there is a significant error introduced by using the column approximation, but for $\mathbf{g}(3\mathbf{g})$ (conditions used for our weak-beam work are closer to this case) there is only a small difference [78]; so even for a fine resolution WBDF images should be a proper projection.

Fulfilling the projection requirement is not, however, the same as being a projection of where the dislocation line runs; this is seen by referring to the kinematical expression for the dark field image from a general distorted crystal, Equation 3.1. It can be seen from this expression that the integral is not over the displacement field itself, but over $\exp(-2\pi i\mathbf{g}\cdot\mathbf{R})\exp(-2\pi isz)$, a function of the displacement field — and this integral is then squared to give intensity I_g . If we use a reconstruction process made with the assumption that the images are projections directly of the property we want to reconstruct, then we will not get a reconstruction of $|\mathbf{R}|$ but of $[\exp(-2\pi i\mathbf{g}\cdot\mathbf{R})\exp(-2\pi isz)]^2$. There are two approaches to this problem:

1. use an imaging mode that gives as little difference from a projection of the position of the core as possible, and use ordinary reconstruction processes with those images
2. make a reconstruction process that works on the basis of images being projections of this function, not of the displacement field itself, and work backwards to recover \mathbf{R} .

This thesis concentrates on the first approach, in the next chapter attempting ADF-STEM as a potential imaging mode of this kind; the second approach

is an opportunity for further work.

3.2.2 The Fourier slice theorem and WBDF dislocation tomography

In normal tomography terms, the Fourier transform of an image taken at tilt angle θ is equivalent to a slice, inclined by θ from the zero tilt position, through the Fourier transform of the sample (Figure 2.3). In the case of dislocation tomography, where we take not a projection of the relevant property of the sample but a projection of a function of it, it can be shown that:

The Fourier transform of an electron micrograph taken at a tilt angle θ is equivalent to a slice, inclined by θ from zero tilt, through a Fourier transform of the ‘object’ reconstructed from a tilt series of such images by an algorithm based on the conventional Fourier Slice Theorem.

Through physical intuition, this appears obvious; it has been checked algebraically in Appendix A.

It appears, however, that standard backprojection electron tomography methods based on the conventional Fourier Slice Theorem can meet with at least limited success in reconstructing dislocations: we have attempted the experiment using ordinary backprojection methods and produced reconstructions that are recognisable as the original structure, though iterative techniques starting from these backprojections produced much better results [42].

Figure 3.4 compares a projection of the magnitude of the displacement field of a screw dislocation calculated using a program written for this purpose by the author, and a dark-field image calculated using R. Schäublin’s CUFOUR program [79]. The magnitude of the displacement field is given in Equation 3.5.

$$|\mathbf{R}_\perp| = |u_{y'}| = \frac{0.816b_z}{2\pi} \tan^{-1} \left[\frac{y}{x} \right] \quad (3.5)$$

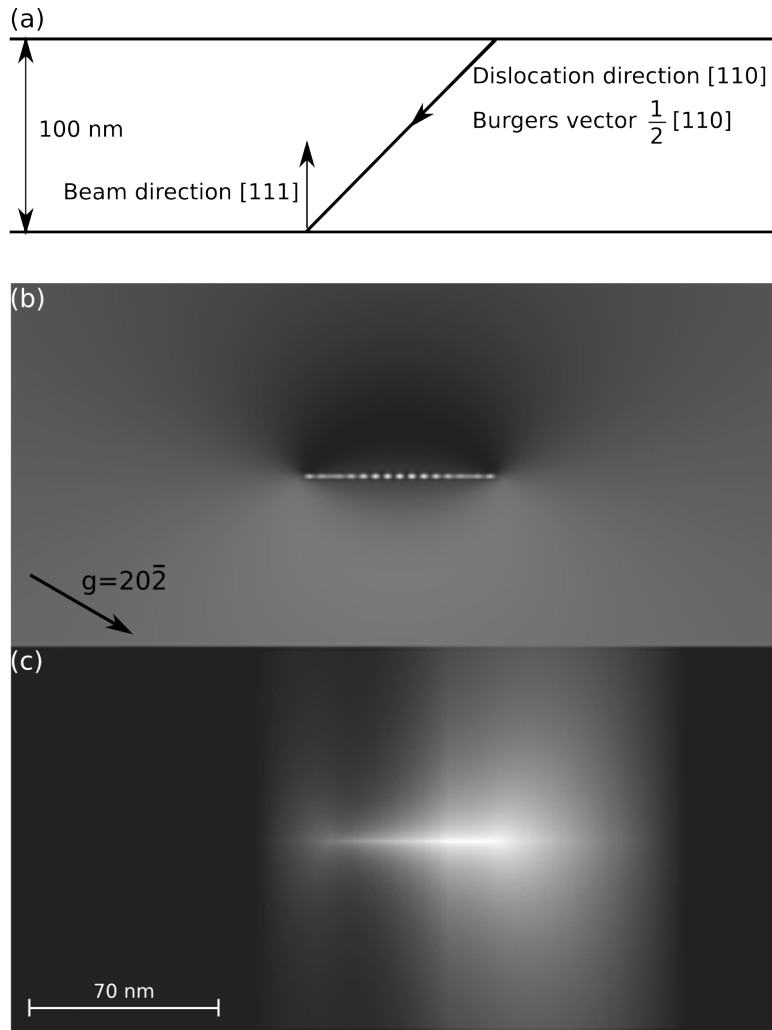


Figure 3.4: Projections through a crystal of Al, showing a screw dislocation running left to right from top to bottom of 100 nm thick film. (a) Sketch side view, showing the geometry of the simulations. (b) Simulated two-beam dynamical dark-field image at $\mathbf{g}(3.5\mathbf{g})$. (c) Projection of magnitude of in-plane component of displacement field in same orientation according to Equation 3.5. No background added to either calculation.

In Equation 3.5, non-primed dislocation coordinate z is the dislocation direction in this expression and b_z the Burgers vector pointing along it, x is in the plane of the foil and perpendicular to the dislocation line and y the direction perpendicular to these. The factor of 0.816 is $\sin 35^\circ$, the angle between the dislocation and the foil normal, from the coordinate transformation used to plot this on primed axes that correspond to the geometry of the crystal and beam; y' in the expression refers to the in-plane direction pointing along the projection of the dislocation line, z' in the beam direction (hence $u_{z'}$ not contributing to displacement perpendicular to the beam) and x' is the same as x . This echoes the system used by CUFOUR in the same situation.

The parallel-sided Al crystal is oriented with $[111]$ (the beam direction) pointing directly down; the screw dislocation intersects the top of the foil on the left and runs down with line direction $[110]$ and Burgers vector $\mathbf{b} = \frac{1}{2}[110]$. The dynamical image is calculated using the systematic row $n(20\bar{2})$ in $\mathbf{g}(3.5\mathbf{g})$ weak-beam condition, with image taken from $\mathbf{g} = 20\bar{2}$. The extinction length for this reflection in these conditions is 139 nm and the foil is 100 nm thick. Surfaces are not properly compensated in either image, the displacement field is merely stopped when the dislocation intersects the surface; the contrast at surfaces should not be relied on.

The dark-field image is evidently different from the simple projection of the displacement field's in-plane component. The dark-field image shows the familiar narrow line, dotted with oscillations (two diffracted beams and the bright field beam are included in the calculation, so some interference can occur to produce this). The projection of the displacement field gives an image that becomes thicker and more diffuse as the dislocation approaches the bottom surface, becoming a low intensity 'aura' around a high-intensity core. Reconstructed, this 'aura' would obscure the dislocation line. The dark-field image gives a **better** image than a simple projection of the displacement field, if the purpose of the study is to trace the path of the dislocation core; we do not want a projection of the displacement field. This demonstrates why using conventional tomography on dark-field images is successful; the 'object' being reconstructed looks more like the core than the displacement

field which initially might seem the best object to reconstruct.

3.3 The first test of weak-beam dark-field dislocation tomography: gallium nitride

Gallium nitride is a direct band gap III-V semiconductor; the band gap is 3.39 eV [80] which allows emission at the blue/ultraviolet end of the visible spectrum. If GaN is alloyed with indium or aluminium its band gap can be tuned to anywhere in the range 0.7 eV (near infrared) to 6.2 eV (UV), giving it potential for use in a wide variety of optoelectronic applications such as lighting, data storage and lasers. In materials normally used for LEDs, dislocations generally act as **non-radiative recombination centres**; that is, they allow electrons and holes to recombine without the emission of light. In GaAs red LEDs, the dislocation density must be less than 10^3 cm^{-2} for light emission to be possible. In GaN this is not the case; a film with 10^9 cm^{-2} can successfully be made to emit blue light [81] with an efficiency of 40-50%, which is sufficiently high efficiency for LEDs but not for lasers; the goal of most current GaN research is to reduce the dislocation density for this purpose.

GaN is hexagonal ($a = 0.319 \text{ nm}$ and $c = 0.518 \text{ nm}$) with a wurtzite structure (Figure 3.5). GaN is not found abundantly in nature and is usually grown by heteroepitaxy. The most common substrate is the (0001) plane of sapphire. The eventual orientation relationship between GaN and the sapphire substrate is $(0001)_{\text{sapphire}} // (0001)_{\text{GaN}}$ and $[10\bar{1}0]_{\text{sapphire}} // [11\bar{2}0]_{\text{GaN}}$. There is a 14.6% lattice misfit between the two structures [80]: a very large misfit for epitaxial growth, but it is the best achievable for GaN. At first, a nucleation layer of a cubic phase grows with the sphalerite structure; the wurtzite structure follows at a second growth stage. Threading dislocations propagate through the film from this interface, roughly 50% edge dislocations of Burgers vector $\mathbf{b} = 1/3 \langle 11\bar{2}0 \rangle$, < 1% screw and the rest mixed with $\mathbf{b} = 1/3 \langle 11\bar{2}3 \rangle$ [82], [83]. Some threading dislocations turn over into the basal plane due to stresses present

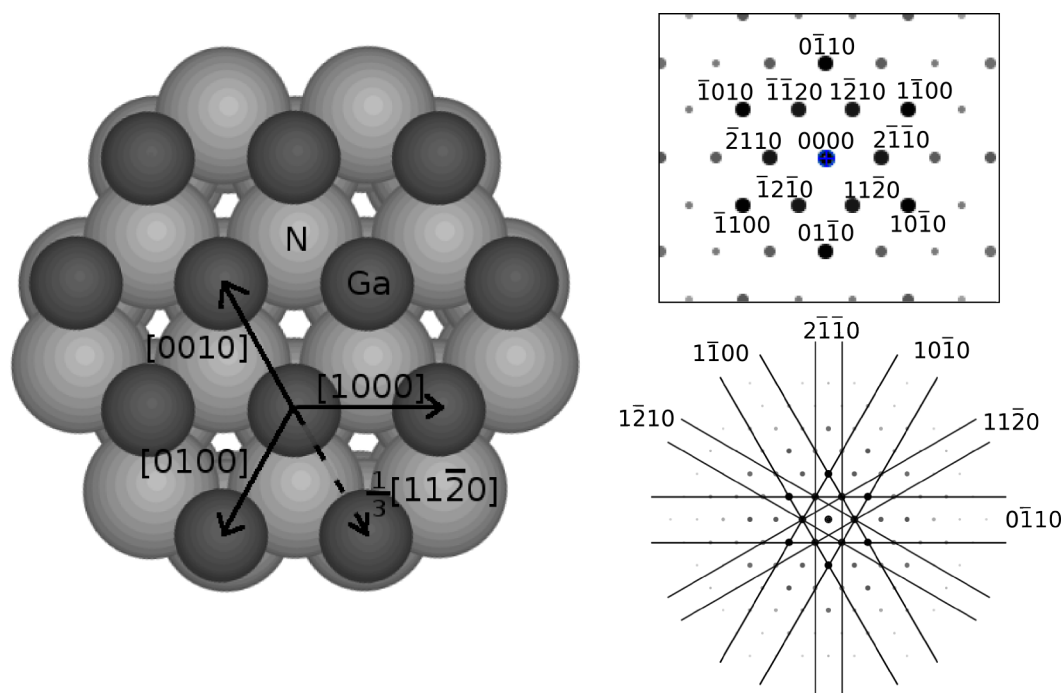


Figure 3.5: Left: the lattice of GaN in $[0001]$ projection, showing the lattice vectors (expressed in simple form of 4-index notation) and the vector $\frac{1}{3}[11\bar{2}0]$ in proper 4-index notation. Right, top: reciprocal lattice and diffraction pattern of GaN on $[0001]$ with reciprocal lattice vectors labelled; bottom: diffraction pattern at shorter camera length showing basic Kikuchi lines.

in the film. The in-plane dislocations interact with other threading dislocations they encounter [42] and can annihilate with them, which is taken advantage of in the epitaxial lateral overgrowth (ELOG) method for reducing the dislocation density of GaN films [84]. Interactions like this that occur during ELOG are an active area of research [85] and characterising the dislocation structure is therefore important.

3.3.1 Procedure

A WBDF tilt series was recorded using a Philips CM30 TEM at 300 kV, from a $[0001]$ plan view sample of Mg-doped GaN grown at the Cambridge Gallium Nitride Growth Facility. The tilt series was recorded from a region near a crack, where in-plane dislocations were abundant. Weak-beam imaging

conditions were $\mathbf{g}(n\mathbf{g})$ with $\mathbf{g} = 11\bar{2}0$; on analysing CBED patterns taken at either end of the tilt range, n varied from 4.2 ± 0.4 at $+58^\circ$ where $s = 0.1nm^{-1} \pm 0.01nm^{-1}$ to 3.0 ± 0.4 at -60° where $s = 0.04nm^{-1} \pm 0.01nm^{-1}$. The CBED pattern taken at $+58^\circ$ tilt was used because Kikuchi lines were too unclear to determine the diffraction condition in the CBED pattern from $+60^\circ$ where the final dark-field image was taken. Although it is best to keep \mathbf{s} constant, aligning the systematic row parallel to the specimen holder tilt axis, using rotation of the specimen in the tilt-rotate holder (β tilt) prior to achieving the weak-beam condition with the dark-field tilts, required great precision which was difficult to achieve even for an expert (fine alignment was done by JSB). Images were taken every 5° . Sample images can be seen in Figure 3.6.

The following processing techniques were tried on the images:

- a directional Fourier-space filter, first low- and high-pass filtered, and then a wedge-shaped mask applied to remove thickness fringes in a certain direction,
- sharpening (subtracting a multiply smoothed copy of the image),
- anisotropic line dilation.

Shift and tilt axis alignments were carried out and a reconstruction was made from images processed using each of the above techniques, using SIRT with 30 iterations — first using an in-house tomography algorithm written by M. Weyland, then (once a script was written to convert images into the correct file format) FEI's Inspect3D. The sample thickness was measured from the reconstruction to be 300-400 nm. 3D visualisation was carried out using Amira.

3.3.2 Results and discussion

The reconstructions from each set of processed images compare as follows (Figure 3.7):

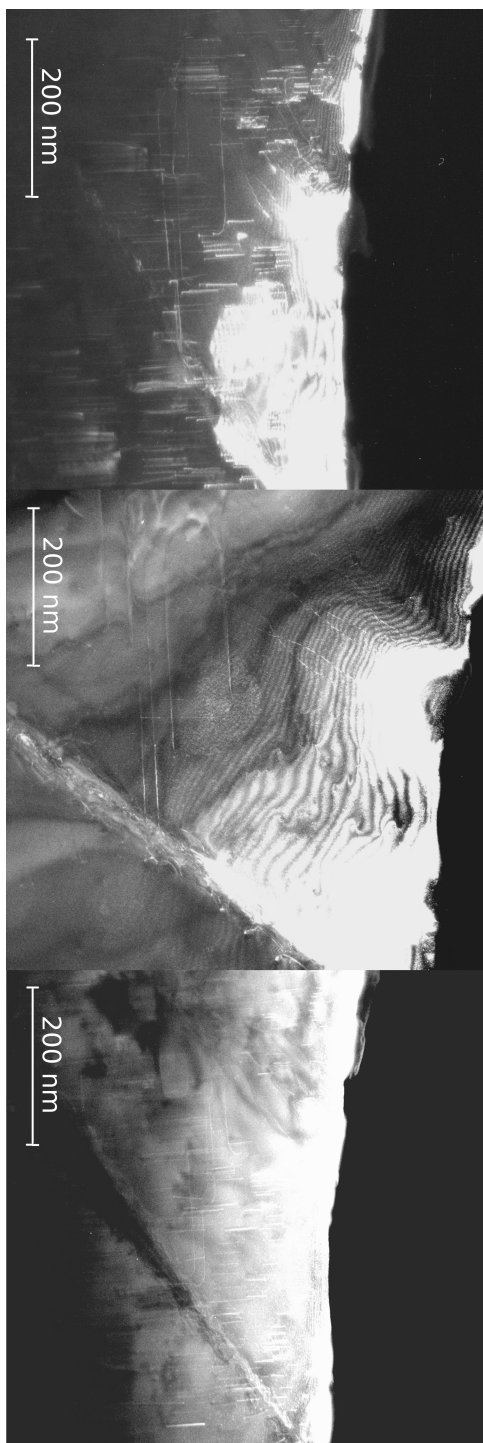


Figure 3.6: Images from weak-beam dark-field tilt series in GaN. Left: -60° image. Centre: 0° image. Right: $+60^\circ$ image.

- Fourier-space wedge filter: this produced a moderately successful reconstruction but with some gaps in the dislocation lines where parts parallel to the thickness fringes had also been removed. Removing features during noise reduction is not an acceptable compromise so this technique was abandoned.
- Sharpening: this produced a clear reconstruction with fewer unwanted artifacts
- Anisotropic line dilation: more speckle noise in the reconstruction, of comparable intensity as the dislocations, and fewer dislocations were visible (especially threading dislocations).

The reconstruction from the sharpened images was the best, without accidental breaks in the dislocation lines and with narrower lines and lower background than the reconstruction from anisotropically line dilated images. This reconstruction will be analysed for the remainder of the section. The sharpened reconstruction is shown in Figure 3.8 and on the enclosed DVD.

Elongation

The reconstructed in-plane dislocations are elongated perpendicular to the plane of the sample (Figure 3.9). This is partially an effect of the missing wedge (Section 2.6.1). According to Equation 2.5, for a maximum tilt of 60° the missing wedge should elongate the features by a factor of 1.55, but the straight in-plane dislocations have an average elongation factor of 2.2 ± 0.4 in the reconstruction.

Additional elongation arises because the effect of elastic anisotropy changes the distance of the dislocation image from the core position as the sample is tilted. The trace of the dislocation image in the reconstruction should therefore follow a partial arc of an ellipse, elongated in the direction of the film thickness, according to Equation 3.6 derived by JSB for in-plane dislocations of screw character, for distance $r_0(\theta)$ between the dislocation core and the position of the peak image, at tilt angle θ , in a material with

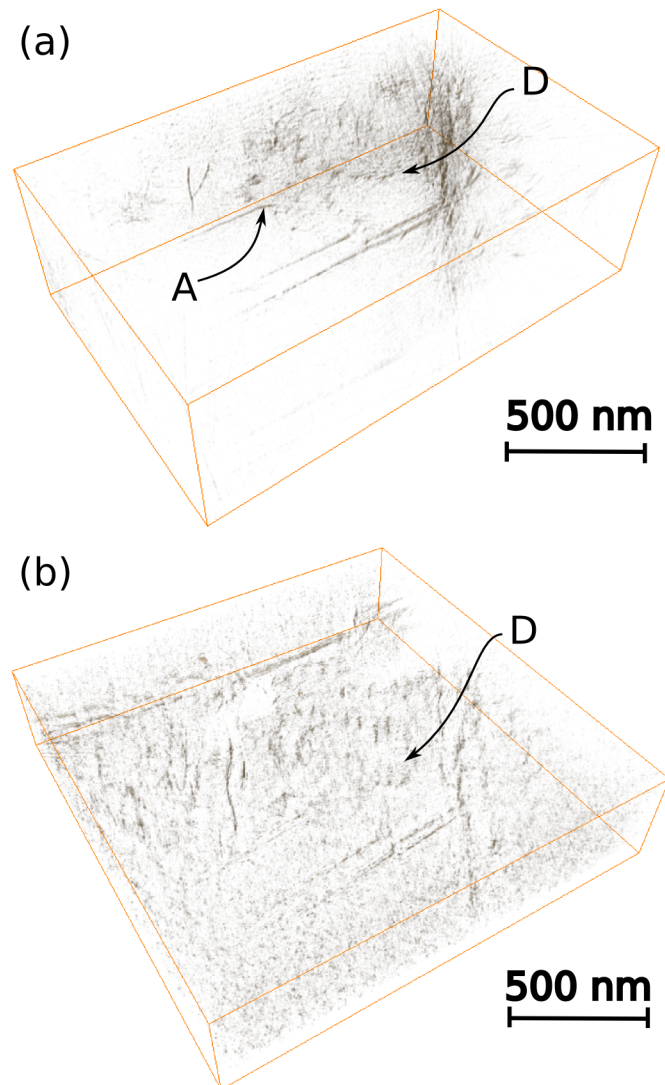


Figure 3.7: Reconstructions from images that have been processed by sharpening [42] (a) and anisotropic dilation (b). Sharpening produces the best reconstruction: anisotropic dilation of the images results in a reconstruction with a speckled background of comparable intensity to the dislocations, and more fragmentation of the dislocation lines; at worst, the dislocation marked A on the reconstruction from sharpened images is barely present in the reconstruction from anisotropically dilated images. The threading dislocations surrounding misorientation domains are reconstructed less completely in the reconstruction from sharpened images however, for example at D.

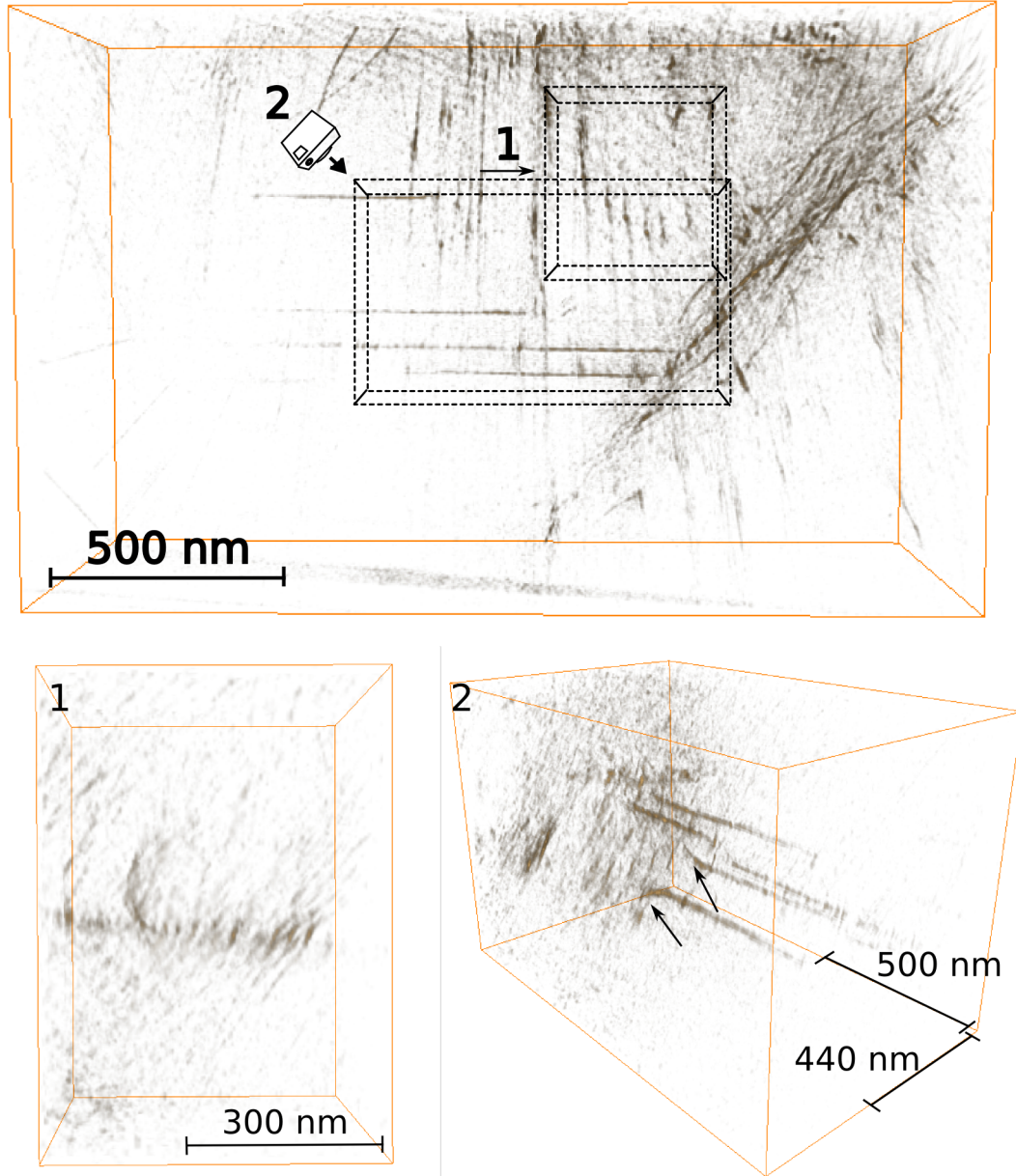


Figure 3.8: Top: reconstruction from GaN weak-beam tilt series, plan view. The view from 1 shows the side view of a ring of threading dislocations surrounding a misorientation domain; the threading dislocations have been reconstructed only in part, and inclined from their real vertical orientation. The view from 2 (viewing angle shown by the camera illustration) shows the long in-plane dislocations, showing their turnover from threading orientation (marked by arrows in 2).

anisotropic elastic constants c_{66} and c_{44} [42].

$$r_0(\theta) = \frac{\mathbf{g} \cdot \mathbf{b}}{2\pi s_g^{eff}} \frac{\sqrt{(c_{66}/c_{44})}}{1 + ((c_{66}/c_{44}) - 1) \sin^2 \theta} \quad (3.6)$$

Other parameters in Equation 3.6 are the dark-field imaging reflection \mathbf{g} , the Burgers vector of the dislocation \mathbf{b} , and s_g^{eff} the effective excitation error after bending of the atomic planes around the dislocation, $s_g^{eff} \approx s_g + g \cdot \frac{d\mathbf{R}}{dz} \Big|_{r_0}$. The elongation factor from this contribution is 3.5 in this orientation of GaN. The arcing caused by this effect is partially cancelled out by shift alignment of the images before reconstruction; however, dislocations with different Burgers vectors arc in different ways, so this does not wholly eliminate elongation from anisotropy, hence the additional elongation in this tilt series. Another contribution to elongation of the reconstructed dislocations can be error in the tilt axis supplied to the reconstruction algorithm; a point is elongated into an arc, as seen in Figure 2.2.

The effect of anisotropy on the peak position of threading dislocations with tilt is more challenging to find analytically; the case of in-plane dislocations is particularly amenable to simplification. An alternative route is to use Robin Schäublin's simulation program CUFOUR to calculate a tilt series and plot the position of the peak in the resulting images with tilt angle. This was done for a mixed threading dislocation ($\mathbf{b} = 1/3\langle 11\bar{2}3 \rangle$) of line direction $[0001]$ in plan view GaN. Screw dislocations account for less than 1% of threading dislocations and edge dislocations would have displacement components only in the basal plane, for which the anisotropy is minimal, so a mixed dislocation is the best case to analyse. The peak position was found to only vary between 1.4 and 1.5 nm from the dislocation position — a change of 1\AA over the tilt range compared to the in-plane case for which the peak position varied by 2.6 nm. The effect of anisotropy on the reconstruction of threading dislocations is therefore probably insignificant at this magnification.

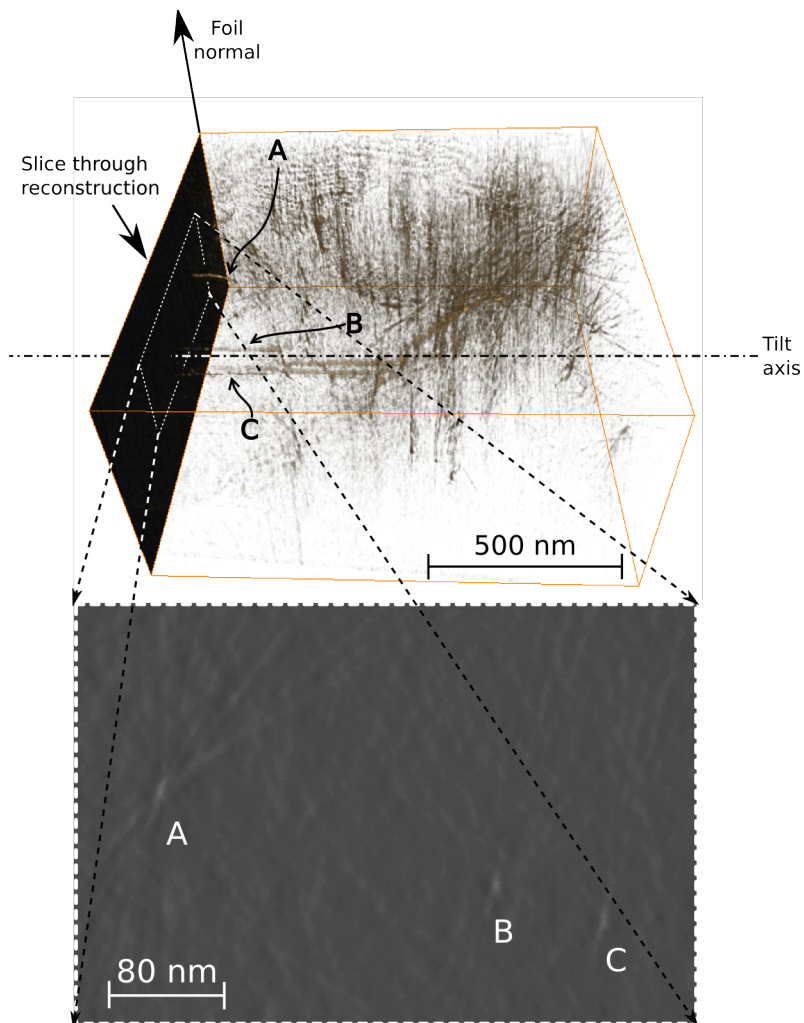


Figure 3.9: Section through in-plane dislocations from GaN weak-beam reconstruction showing elongation of the reconstructed dislocations along the foil normal. An orthoslice has been taken on the dotted rectangle shown, including dislocations A, B and C, viewed from outside the reconstruction bounding box.

Other features

In-plane dislocations in the reconstruction have higher intensity than threading dislocations. In addition, the threading dislocations appear inclined to the foil normal, though it is known that they follow the $[0001]$ axis and become points in the zero tilt image. There are several possible reasons for this:

- The threading dislocations disappear into noise at orientations close to zero tilt, whereas the in-plane dislocations are never seen ‘end-on’ in this way.
- When the threading dislocations do appear, they are inclined with respect to the beam direction and have oscillatory contrast from dynamical effects. This makes their images less consistent between tilt angles.
- The alignment procedures before reconstruction relied mainly on the clearly visible in-plane dislocations. If the in-plane dislocation images follow the locus of an ellipse due to elastic anisotropy [42]), then the position of the threading dislocations’ images will not be made more consistent by alignment.

3.4 Weak-beam dark-field tomography of a microcrack in Si using tilt series around multiple axes

The sample in this study is Czochralski-grown silicon and was supplied by Prof. K Kaneko of Kyushu University. The wafer had been nanoindented, then annealed to allow cracks to develop and FIB lift-out had been used to prepare a TEM sample with foil normal $[001]$ from the crack tip. The volume from which tilt series were taken contains a microcrack emanating from the primary crack tip. The original aim of the study was to observe the difference in dislocation behaviour when the sample contains Cu precipitates;

this data is from the control sample, because the precipitated sample was of a morphology unsuitable for tomography. However, this work led to some interesting opportunities for technique development.

Microcracks propagate during plastic deformation, from the ends of previously-formed brittle cracks. They produce moiré fringes as stacking faults do — there are two lattices with a small displacement between them, one overlapping the other in the beam direction. Unlike stacking faults, however, they do not have a displacement that is a predictable fraction of a lattice vector. Microcracks tend to propagate on easy cleavage planes, such as $\{111\}$ planes in Si. In a material such as Si at the ductile-brittle transition temperature, where cleavage is competing with plastic deformation, the dislocation structure along microcracks is the debris of dislocation propagation ceasing to adequately shield the end of the brittle crack from the applied stress, and being overtaken by a growing fracture surface [86].

It was possible to take four weak-beam dark-field tilt series using different, linearly independent \mathbf{g} ; this enables some exciting work. The Burgers vectors of dislocations can be determined using three images. More importantly, this provides an opportunity to attempt multiple-axis defect tomography. This may enable us to see dislocations that are absent in one diffraction condition but present in others, that would be missed in single-axis tomography; it should also alleviate elongation that occurs for linear features perpendicular to the single tilt-axis [87].

Conversely, multiple-axis dislocation tomography has some pessimistic implications; if \mathbf{g} is different, $\exp[2\pi i(\mathbf{g}\cdot\mathbf{R})]$ is different and the object being reconstructed is different in the different tilt series according to the dark-field interpretation of the Fourier Slice Theorem (Section 3.2.2). Not only is \mathbf{g} different but \mathbf{s} is likely to be different in the different tilt series as well as varying within each tilt series. The variation in $\exp[2\pi i(\mathbf{g}\cdot\mathbf{R})]$ and \mathbf{s} causes the dislocation image position to move and the form of the peak to change, so the likely effect of these problems is that the resolution in dislocation position will be degraded.

3.4.1 Tilt series acquisition

Acquisition of the tilt series was performed by J. S. Barnard, using a Philips CM300 TEM at 300keV, at 11500x magnification. The process was spread over two days with lens conditions replicated on the second day; fine focusing was done using specimen height. The images were energy-filtered to keep only the zero loss electrons, to improve image contrast. Four tilt series were acquired of the microcrack, using the diffraction conditions given in Table 3.1. The weak-beam condition and excitation error \mathbf{s}_g were calculated by the author for those cases where CBED patterns were recorded. Zero tilt images from these four tilt series are given in Figure 3.10. Fringes at the microcrack surfaces can be seen in all of them; the fringe spacing is different in the $\{220\}$ and $\{400\}$ images, and some areas show brighter contrast than others, depending on \mathbf{g} . At steps in the microcrack, contrast is either bright and block-like or fringed and complicated. The sample thickness in the region of interest was measured as $270nm$ by the energy-loss log-ratio method [88, p.301]; error of 5-20% is quoted in the literature for this technique [89].

3.4.2 Results and reconstruction

The microcrack is close to a $\{111\}$ plane; the closest such plane is $(\bar{1}\bar{1}\bar{1})$, found by considering the geometry with respect to the tilt axes of the four tilt series (Figure 3.11). Burgers vector analysis was attempted for the dislocations around the crack but the images were not all clear enough to say for certain whether dislocations were visible or invisible as they were in front of the heavily moiré fringed fracture surface.

Alignment and reconstruction were carried out using the SIRT algorithm with 30 iterations, in FEI's Inspect3D. The fringe contrast in series 4 was so inconsistent with tilt as to prevent automatic and manual alignment, so this tilt series was not reconstructed. Reconstructions from series 1, 2 and 3 are shown in Figure 3.12, Figure 3.13 and Figure 3.14 respectively. It can be seen that the microcrack is made of multiple steps on the same plane. The reconstructions reproduce the view from zero tilt well, and from edge-on the steps are roughly planar.

| Series | \mathbf{g} | s_g (nm^{-1}) at min tilt | Weak-beam condition at min tilt | s_g (nm^{-1}) at max tilt | Weak-beam condition at max tilt |
|--------|--------------|------------------------------------|--|------------------------------------|--|
| 1 | $2\bar{2}0$ | $0.04 \pm 6 \times 10^{-4}$ | $\mathbf{g}(2.6\mathbf{g}) \pm 0.04\mathbf{g}$ | $0.07 \pm 1 \times 10^{-3}$ | $\mathbf{g}(3.8\mathbf{g}) \pm 0.05\mathbf{g}$ |
| 2 | 220 | not found | not found | not found | not found |
| 3 | 400 | $0.1 \pm 3 \times 10^{-3}$ | $\mathbf{g}(2.8\mathbf{g}) \pm 0.09\mathbf{g}$ | not found | not found |
| 4 | 040 | not found | not found | not found | not found |

Table 3.1: Table of tilt series and diffraction conditions for weak-beam dark-field tilt series taken from Si sample

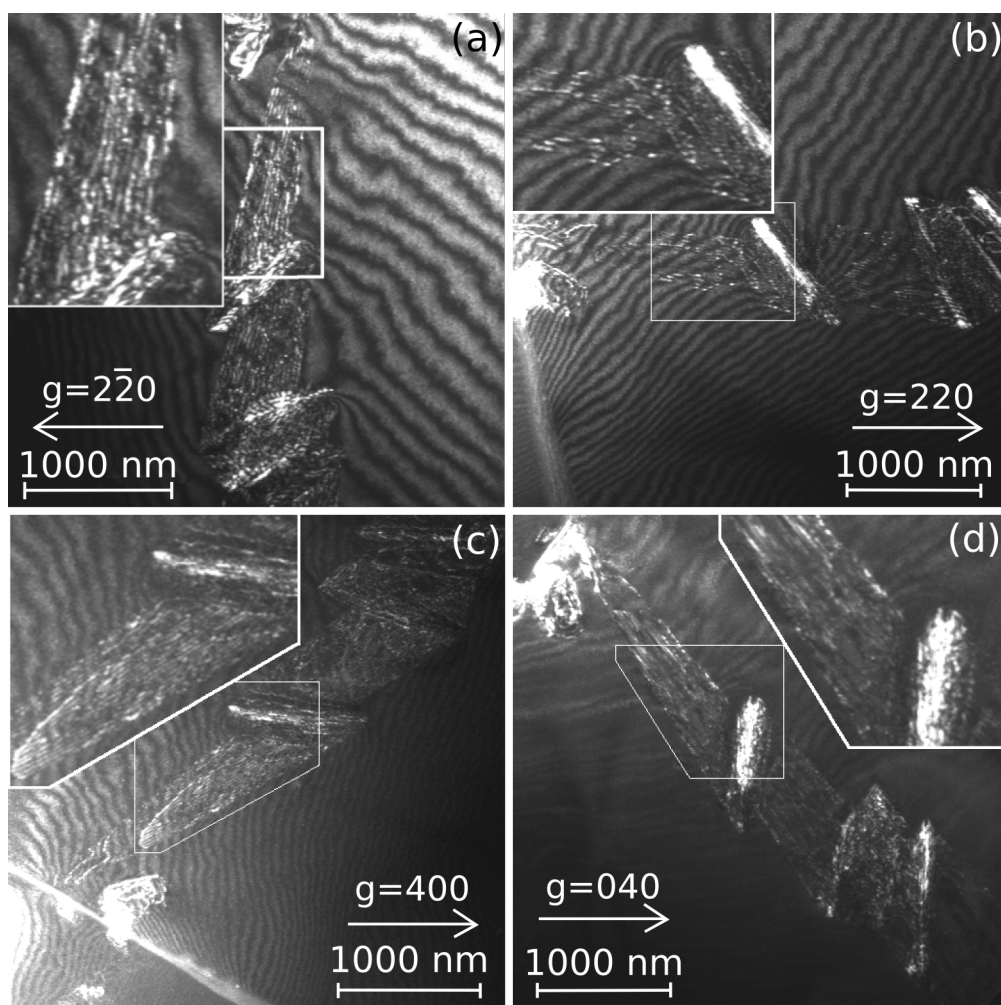


Figure 3.10: Zero tilt weak-beam dark-field images from: (a) series 1, taken using $\mathbf{g} = 2\bar{2}0$; (b) series 2, taken using $\mathbf{g} = 220$; (c) series 3, taken using $\mathbf{g} = 400$; (d) series 4, taken using $\mathbf{g} = 040$. Tilt axes are parallel to the \mathbf{g} shown on the images.

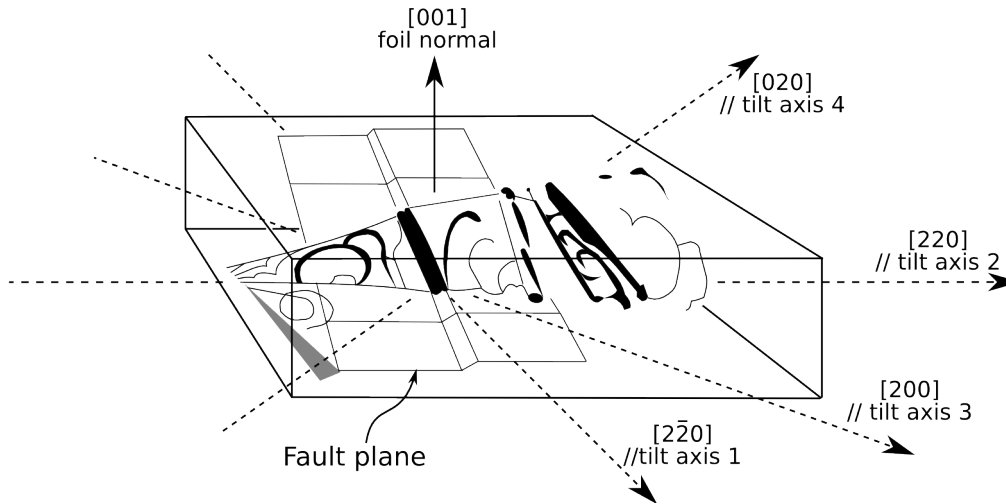


Figure 3.11: Sketch of main regions producing intensity in the microcrack in the Si sample with approximate orientation of crack plane. Tilt axes are marked on (see also Figure 3.10); according to the chosen orientation of the coordinate system, the $\{111\}$ plane of the crack is $(\bar{1}\bar{1}\bar{1})$.

From other directions, things are less optimistic. Series 1 ($g = 2\bar{2}0$) does not give a flat plane and dislocations close to the crack surfaces are not reproduced as continuous lines; dislocation B in Figures 3.13 and 3.14 shows this well. Also visible in the reconstruction of series 3 are traces of structure within the tangle at D, which is however heavily elongated perpendicular to the tilt axis. Series 2 ($g = 220$, tilt axis down centre of microcrack) and series 3 ($g = 400$) enable reconstruction of a flat plane. The angle of this plane with the horizontal axis is $45^\circ \pm 7^\circ$ in series 2; the error in measurements of the plane in the other two tilt series, from the very elongated dislocations, is too large to give a meaningful measurement. The angle that $(\bar{1}\bar{1}\bar{1})$ should make with (001) is 54.7° ; this is still outside the margin of error for the measured angle. As it is unlikely that the dislocations along the microcrack slipped on some plane 9° from a close-packed low energy slip plane, this is probably a misrepresentation of the real defect plane, with contributions from diffraction condition misalignment (to be covered in Section 3.6) and inaccuracies in shift alignment due to the moiré fringes.

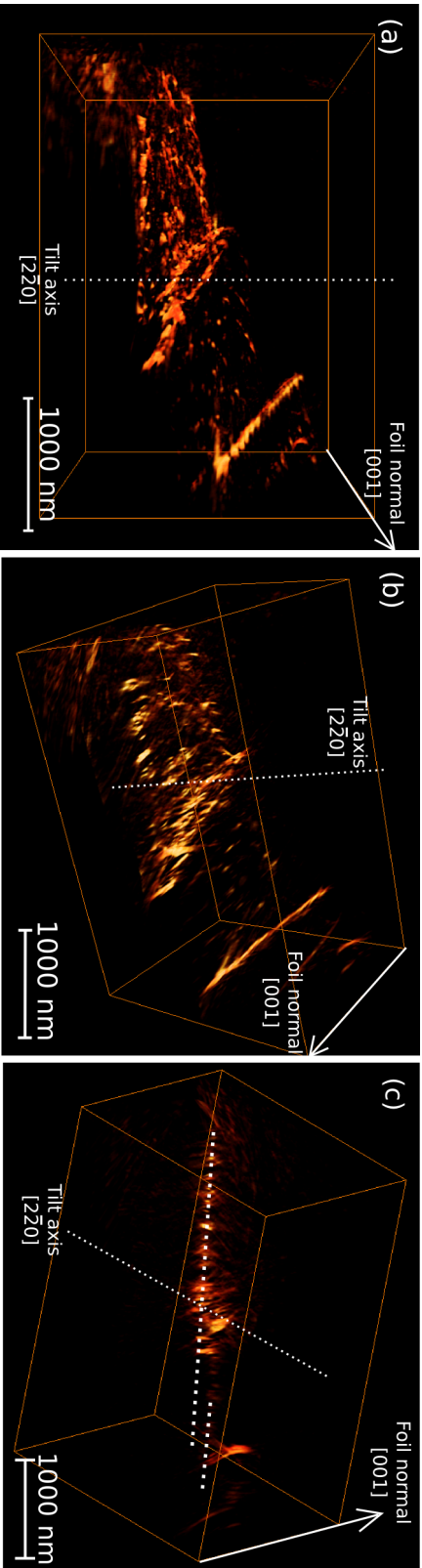


Figure 3.12: Views of the reconstruction from WBDF tilt series 1 ($\mathbf{g} = 220$, tilt axis roughly vertical in (a)) from Si sample. (a) from $[001]$ foil normal direction, perspective view. (b) from $[\bar{1}\bar{1}\bar{1}]$ looking onto the slip plane of the dislocations; dislocations are not reconstructed as continuous lines but as chains of broad points. (c) from $[1\bar{2}\bar{2}]$, looking at the slip plane side on. Distinct steps are visible (marked by dotted white lines) but points marking dislocations in the steps are elongated out-of-plane to a width comparable with the step height. Significant arcing is visible, partly due to imperfect tilt axis misalignment though this was optimised as far as possible.

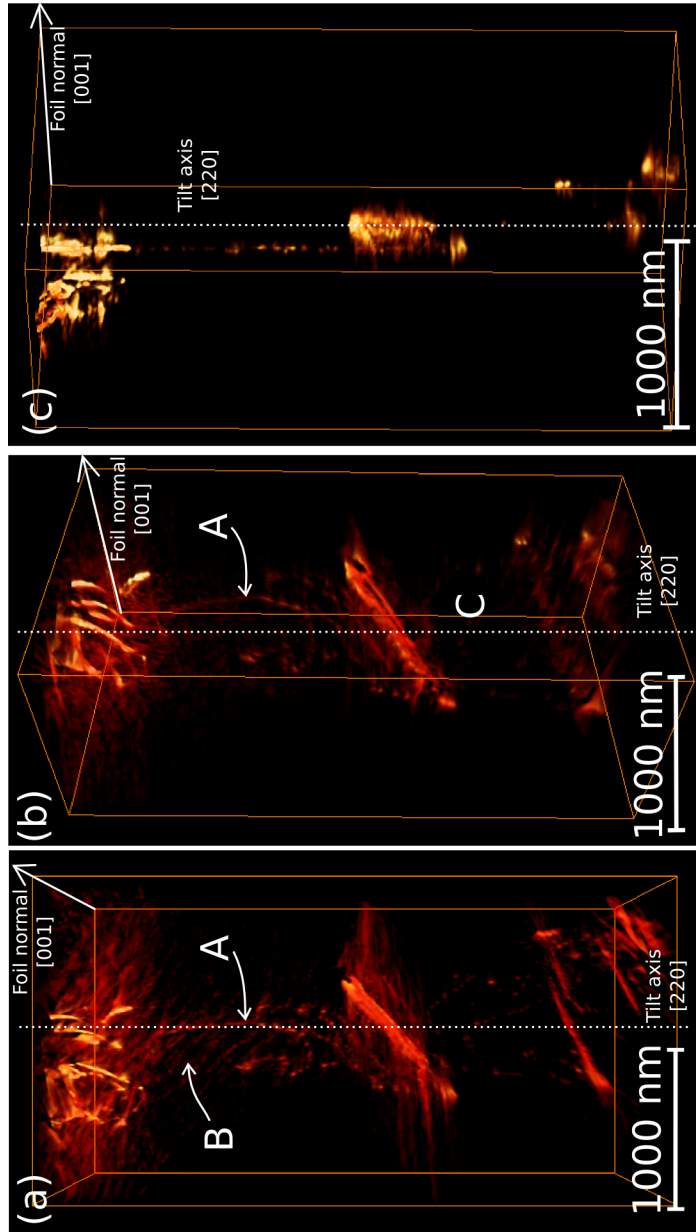


Figure 3.13: Views of the reconstruction from WBDF tilt series 2 ($g = 220$, tilt axis vertical in (a)) from Si sample. (a) from $[001]$ foil normal direction, perspective view; some thickness fringes remain at B. (b) from $[\bar{1}\bar{1}\bar{1}]$ looking onto the plane of the defect; dislocations are reconstructed more consistently than from series 1 but are still fragmented, e.g. at A. Dislocations in the weaker part of the defect (marked C) have not reconstructed successfully. (c) from $[1\bar{2}\bar{2}]$, looking at the microcrack plane from side on. Only one step can be seen, but reconstructed dislocations are less elongated of the slip plane than from series 1.

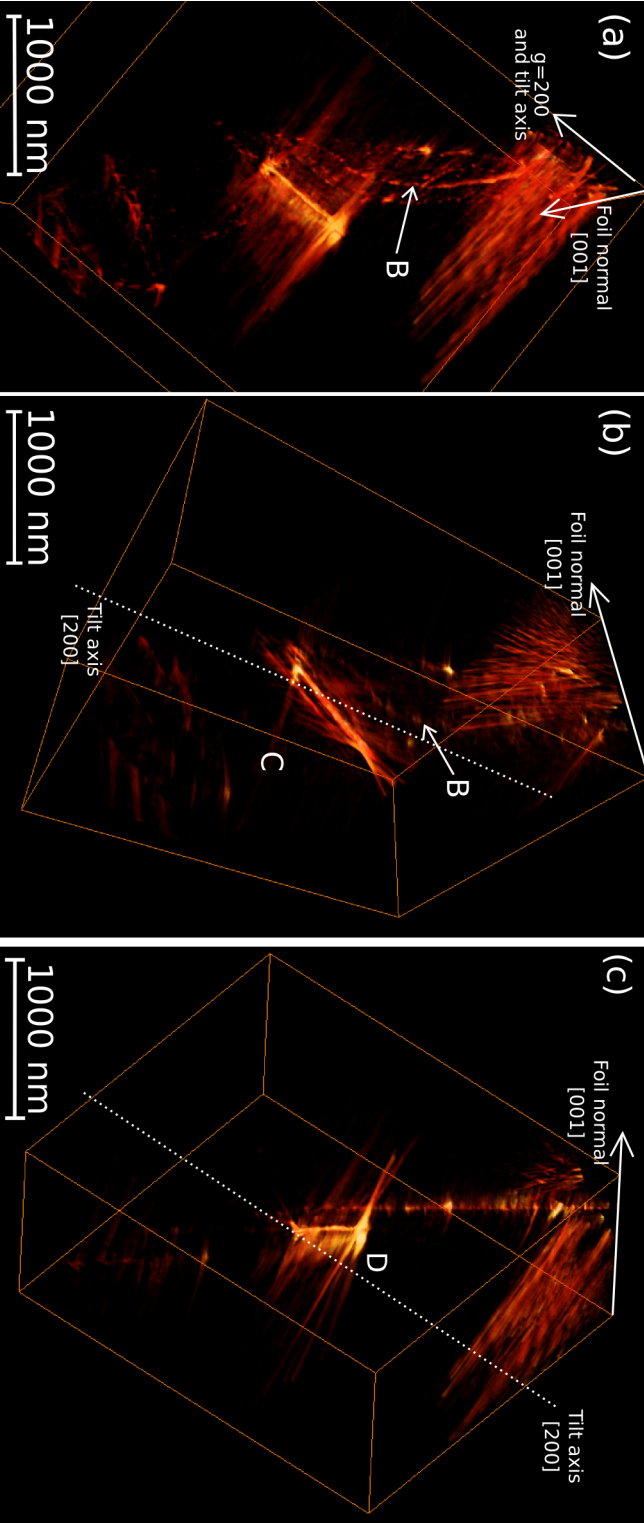


Figure 3.14: Views of the reconstruction from Si WBDF tilt series 3 ($g = 400$, tilt axis as shown on (a)). (a) Perspective view from [001] foil normal direction; dislocations appear to have reconstructed clearly. (b) View from $[111]$ looking onto the plane of the defect. (c) View from $[122]$, looking at the slip plane from the side. Only one step is seen as with series 2; the features on this step are elongated.

3.4.3 Discussion: implications for WBDF tomography of stacking faults

The main conclusion drawn from these results is that some choices of tilt axis and imaging reflection lead to a successful reconstruction and some do not. Possible reasons for failure include:

- Tilt series alignment was poor, but if it had been correct, tomography would have succeeded.
- Fringed contrast from the microcrack surfaces fails the projection requirement too badly to allow tomography to succeed, regardless of alignment. This would have significant implications for tomography of stacking faults also.

Alignment of the images was difficult; automatic alignment could only converge to corrections ~ 10 pixels (in 512×256 pixel images) before resulting in oscillations of the features from side to side between images, as the fringe contrast changed between tilt series images. Manual alignment was attempted for the reconstruction of series 4 but it too was unsuccessful at fine scale. The thickness contours apparent near the narrow end of the microcrack were mostly removed from the alignment operation by judicious application of a bandpass filter when calculating cross-correlations, so did not further degrade alignment.

In order to determine whether tomography of a planar defect producing fringe contrast would have succeeded with perfect alignment, two tilt series of $\mathbf{g}(3\mathbf{g})$ weak-beam images of a stacking fault were simulated using CUFOUR, keeping all parameters the same except changing the beam direction by adding a small vector perpendicular to the imaging vector each image. A stacking fault was used because this is an existing option in CUFOUR, whereas a microcrack is not. The chosen method of producing a tilt series means the angular tilt increment was not regular; $\Delta(\tan \theta)$ was regular but not $\Delta \theta$ itself. With the defect placed at the same point relative to the centre of the image every time, the simulated tilt series starts with perfect alignment. Images were simulated from 45° to -45° for $\mathbf{g} = 200$ and $\mathbf{g} = 020$.

The defect modelled was in aluminium (because a crystal data file was accessible), on a stacking fault with displacement $\frac{1}{3}[111]$ bounded by partial dislocations running along a $[0\bar{1}1]$ direction from bottom to top of the 100 nm thick crystal, with Burgers vectors $\frac{1}{6}[\bar{2}11]$ and $\frac{1}{6}[\bar{1}2\bar{1}]$ according to the Thompson tetrahedron convention for which Burgers vectors and stacking fault displacements are compatible in an fcc crystal [1]. A partial dislocation separation of 50 nm was used, which is larger than would ever be found in nature but allowed the fringes to be observed more easily.

For the series with $\mathbf{g} = 020$, the tilt axis was along the projected length of the stacking fault, so the projected width changed and the fringes did not appear to move along the length as the crystal tilted (Figure 3.15). When this tilt series was reconstructed using 30 iteration SIRT (same as the Si experimental tilt series), the stacking fault was reproduced as a flat, fringed plane whose tilt with respect to the sample axes could be seen easily (Figure 3.16). However, it is the wrong plane - the defect was on (111) but the reconstruction shows something closer to a $\{101\}$ plane. This is because of a limitation in the simulation: CUFOUR models defect images using a generalised cross section in which it calculates all possible slices that will be needed for the image, and integrates over the correct portion of this generalised cross-section for each row. The program does not ‘know’ there is a crystal, so when the crystal is turned about a tilt axis parallel to the dislocations, it does not compute the lateral movement between images from parts of the dislocation that are at different heights. The result is that the images do not show the dislocations’ change in lateral position with depth in the tilted sample, so their line direction in the reconstruction is brought closer to the plane of the sample. An adaptation to the image simulation technique is needed for defect tomography simulations to succeed with the tilt axis in an orientation that requires this effect.

For the series $\mathbf{g} = 200$, the tilt axis was across the projected width of the stacking fault, so the stacking fault tilted along its length and the fringes appeared to ‘move’ along the stacking fault through the tilt series (Figure 3.17). The simple projection object that would give this behaviour is an array of rods, and this is what is reconstructed (Figure 3.18). However,

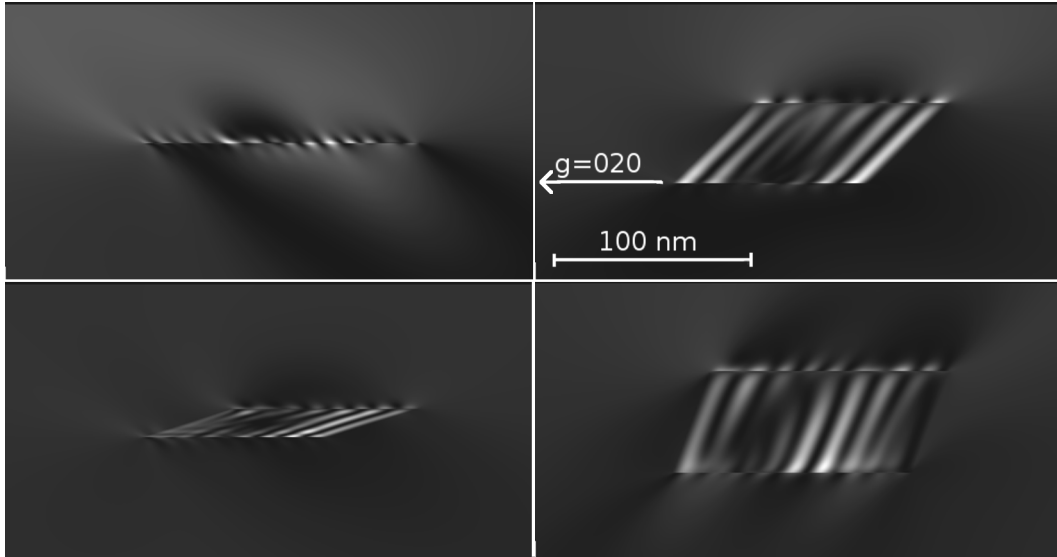


Figure 3.15: Images from tilt series of simulated images of stacking fault in Si, taken with $\mathbf{g}(3\mathbf{g})$ weak-beam condition for $\mathbf{g} = 020$. Tilt axis is parallel to \mathbf{g} . Top left: -24° . Bottom left: -12° . Top right: 0° . Bottom right: $+18^\circ$. Fringes do not move much along the length of the stacking fault through the tilt series.

for $\mathbf{g} = 200$ the reconstructed defect occupies the correct plane, even if it is not flat.

From the nature of the $\mathbf{g} = 200$ simulation, it would appear that to reconstruct a stacking fault as a flat object, it is necessary to choose a tilt axis orientation so that the fringes in weak-beam stacking fault contrast move as little as possible with tilt; but it is difficult to check this by simulation because of the aforementioned limitations in simulation software (which was not designed to model tomography in the first place). It has been attempted to find the optimal orientation for this mathematically but this is an extensive task for further work.

The Si microcrack tilt series do not appear to agree with this hypothesis. Series 2, for which the tilt axis is oriented parallel to the microcrack moiré fringes so should give maximum problems due to fringe movement, reconstructs to give dislocation lines and no microcrack plane in the thin end of the defect; series 1, for which the tilt axis is oriented perpendicular to the fringes where one would expect least fringe movement with tilt angle,

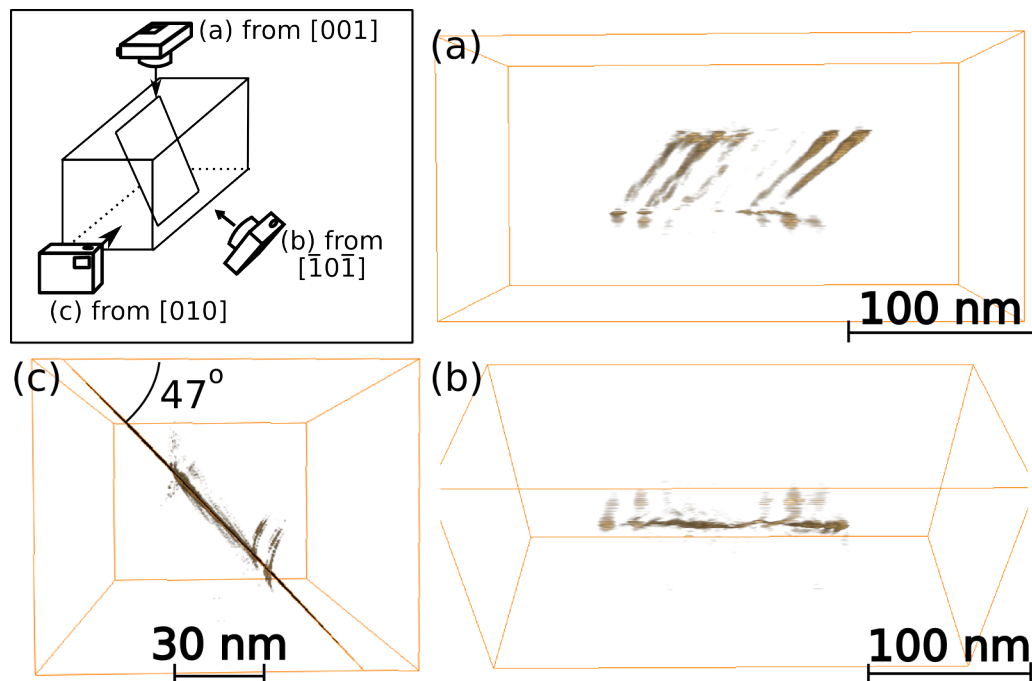


Figure 3.16: Reconstruction of simulated tilt series of (111) stacking fault from $g = 020$ simulated WBDF images. Viewing directions described correspond to the vector from the origin to the observer. (a) From $[001]$ (as zero tilt image). (b) View from $[\bar{1}0\bar{1}]$ showing the reconstruction is flat although it is not on the correct plane. (c) View from $[010]$, showing the plane of the reconstruction is actually close to $(\bar{1}01)$; the angle shown would be 45° for the $(\bar{1}01)$ plane. The error on the measurement of this angle in the reconstruction is $\pm 2^\circ$.

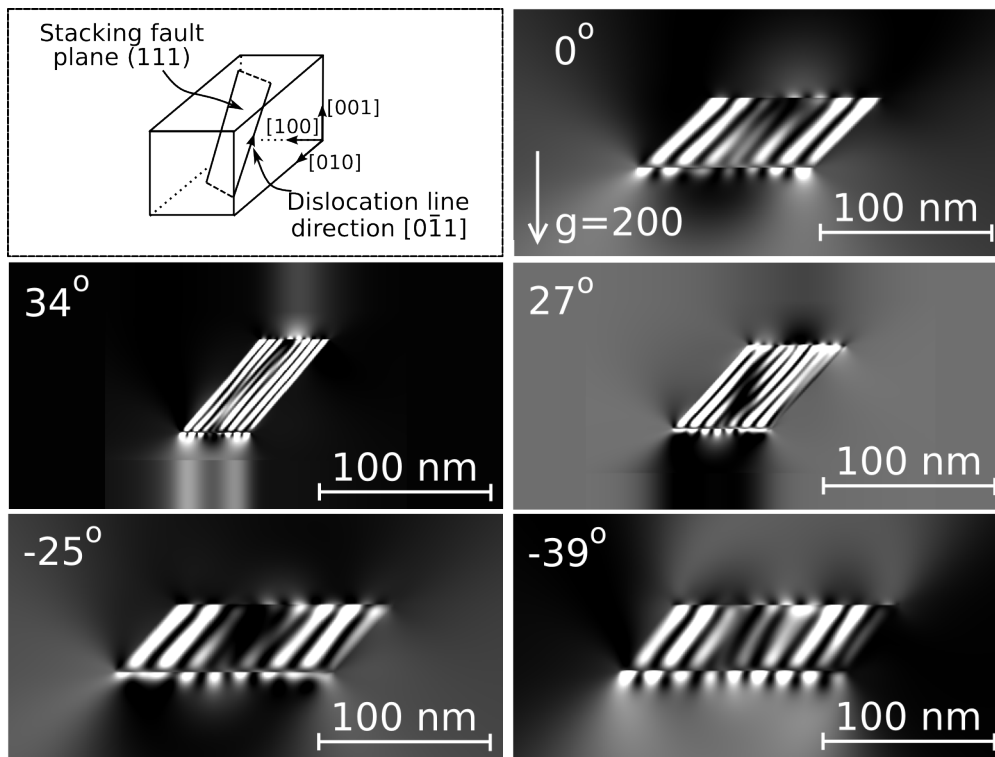


Figure 3.17: Images from simulated weak-beam tilt series of (111) stacking fault in Al, taken with $g = 200$. Simulated using CUFOUR; length then scaled for tilt angle. Diagram at top left shows the geometry of the simulation.

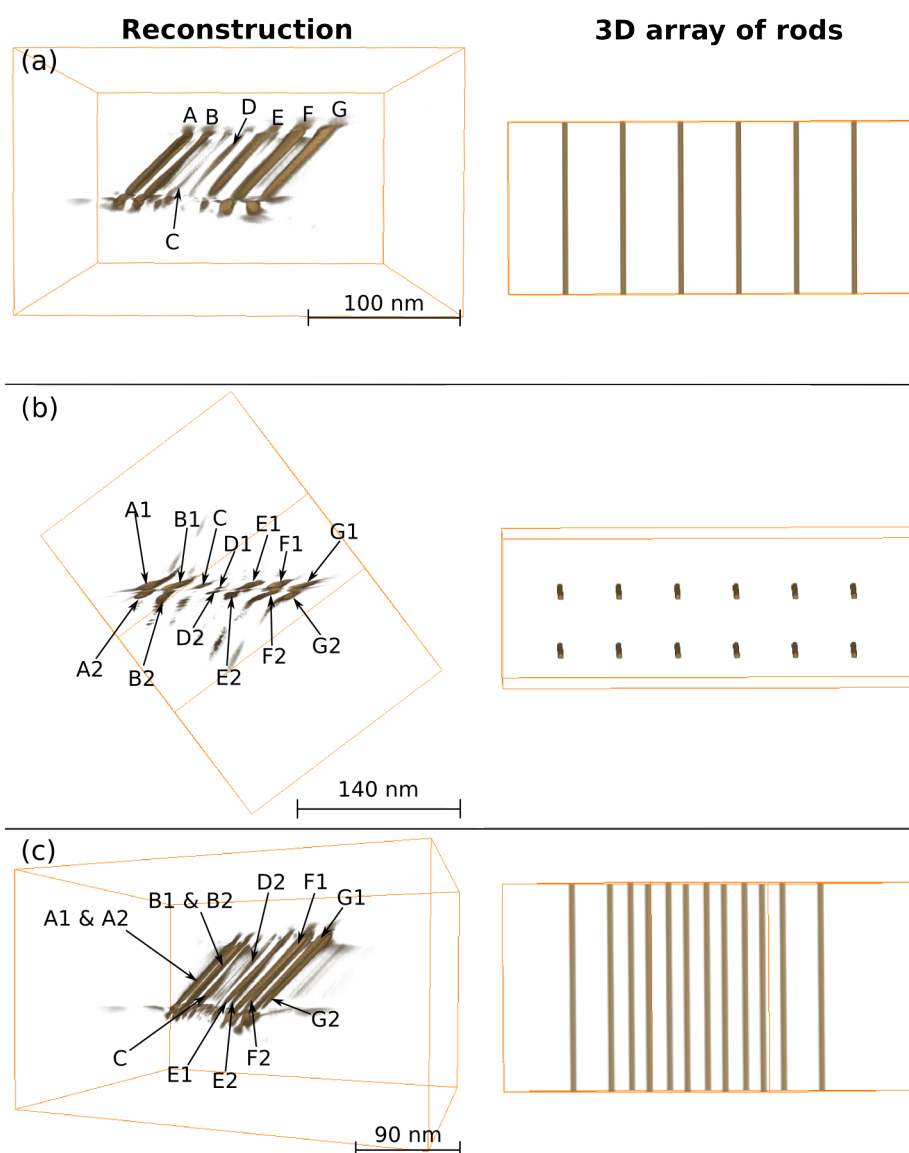


Figure 3.18: Reconstruction from simulated $g = 200$ weak-beam tilt series for a stacking fault on (111) with [001] foil normal, compared with a 3D array of rods. (a) From the zero-tilt position, with stacking fault fringes labelled; reconstruction seen in perspective view. (b) View of the reconstructed stacking fault from observation position at $[11\bar{2}]$ from the origin, seeing the (111) fault end-on; a truly planar representation of the fault would appear flat from this orientation. The reconstructed stacking fault has two layers of fringes. (c) View of reconstruction rotated 27° from (a) about the vertical axis, i.e. the same orientation as the 27° tilt series image in Figure 3.17. The change in periodicity of stacking fault fringes is reproduced by the two layers of fringes.

reconstructs to give a thick plane. The experiment and simulation are not completely comparable, however:

- The magnification of the experimental tilt series is much lower than in the simulation; a small misalignment in shift between two images can easily cover a whole fringe.
- In series 2 and 3 the microcrack areas near the thin end of the defect show little or no moiré fringe contrast (Figure 3.10).
- A stacking fault and a microcrack are different entities; the microcrack's displacement is larger and less predictable than that of a stacking fault.

In order to properly test this hypothesis more work is required — simulations and tilt series of the same stacking fault need to be obtained, and simulation of defect tilt series needs to be extended to any tilt axis.

This particular sample did not reveal anything about silicon. However, following this experiment, Prof. Kaneko performed the same ADF STEM tomography with a team in Kyushu, on a similar sample prepared from a crystal grown with a higher impurity concentration, in which the dislocations had interacted with Cu precipitates formed from solid solution as a result of the stress concentration at the crack tip [46]. The volume of interest in that sample did not contain large areas of fringed contrast so alignment and reconstruction were carried out much more accurately. The reconstruction was then used to find the slip planes of dislocations in the volume, which will facilitate research in the field of fatigue dislocation mechanics in which Si is often used to test theories.

3.5 Dislocations in a Ti-Al alloy reconstructed by weak-beam dark-field tomography

3.5.1 TiAl samples

This work was done in collaboration with Dr. Y. L. Chiu of Birmingham University. His sample was Ti-56at%Al, made largely of the TiAl phase which takes the $L1_0$ ordered crystal structure: atoms are arranged as in a face-centered cubic structure, but the (002) planes are layers of Ti and Al in an alternating pattern. The difference in sizes of the atoms makes the structure tetragonal, not cubic; the difference in structure factor between the Ti and Al layers allows reflections such as 001 that are systematically absent in the fcc diffraction pattern, to be present.

At this composition, to the Al-rich side of the stoichiometric composition for the TiAl phase, regions of the Al_5Ti_3 superstructure evolve, in which the atoms are distributed differently over the atom sites in the face-centered lattice — some of the sites in the Ti layers are occupied by Al atoms in a regular pattern. The unit cell of this Al_5Ti_3 superstructure spans four of the $L1_0$ unit cells in the (001) plane (the Al_5Ti_3 unit cell is at 45° to the $L1_0$ axes) but only one unit cell in the \mathbf{c} direction. Dislocations in the $L1_0$ structure therefore do not correspond to a whole dislocation in the Al_5Ti_3 regions, but cluster together in sets of four, with planes of antiphase boundary (for the Al_5Ti_3 superstructure) between them ≈ 25 nm wide; if they do not do this, an antiphase boundary is left trailing behind the single dislocations, which is energetically unfavourable [90].

There are two kinds of dislocations mainly present in the $L1_0$ matrix of this material, slipping primarily on $\{111\}$ planes: ‘ordinary’ dislocations with $\mathbf{b} = \frac{1}{2}\langle 110 \rangle$, and ‘superdislocations’ with $\mathbf{b} = \langle 101 \rangle$. (The half-and-half brackets indicate members of the restricted sets of vectors in this tetragonal structure; for example, $[101]$ and $[011]$ are equivalent but $[110]$ is not, because it is contained in an (002) plane of the same element.) Neither of these

types of dislocations are whole dislocations in the Al_5Ti_3 superstructure. The behaviour of these dislocations in the Al_5Ti_3 superstructure causes an abnormal rise in yield stress with temperature at 600-1000°C followed by a sudden decrease [91], which is a relevant temperature range for high-temperature mechanical applications such as turbines for power generation, so understanding this behaviour is important. Especially important is the cross-slip behaviour of the individual dislocations in the bundles of four within the Al_5Ti_3 regions; if one cross-slips and the others do not, which is reasonable as the three antiphase boundaries between the four dislocations in a bundle are not all equivalent, mobility is markedly reduced. The purpose of using electron tomography to characterise this sample was to inspect bundles in which it was suspected that cross-slip of some dislocations within the four-bundle had occurred, to determine which of the four it was and on which plane.

3.5.2 Tilt series collection

The sample of Ti-56%Al, grown using the arc melting method and subsequently made into a single crystal using the floating zone method [90] had been cut on the (111) plane, in which slip is expected to occur, and jet electropolished to electron transparency.

A WBDF tilt series was taken on a Philips CM30 at 300kV, using a weak-beam condition that varied from $\mathbf{g}(2.9\mathbf{g}) \pm 0.03\mathbf{g}$ to $\mathbf{g}(4.3\mathbf{g}) \pm 0.1\mathbf{g}$ at the ends of the tilt range, with $\mathbf{g} = \bar{2}20$. Images were taken from -60° to $+59^\circ$ every 4° ; specimen tilt was adjusted by as much as 1° for images at the highest positive tilts when the contrast deteriorated due to unfavourable diffraction conditions. Images from the tilt series are shown in Figure 3.19.

The images in this tilt series have much better contrast for tomography than those in previous weak-beam tilt series. There are fewer thickness and bend contours in the background to dominate the cross-correlation function instead of the dislocations, and the dislocation contrast itself is more consistent. Because of the quality of the images, this tilt series could easily be aligned automatically before reconstruction. The cross-correlation

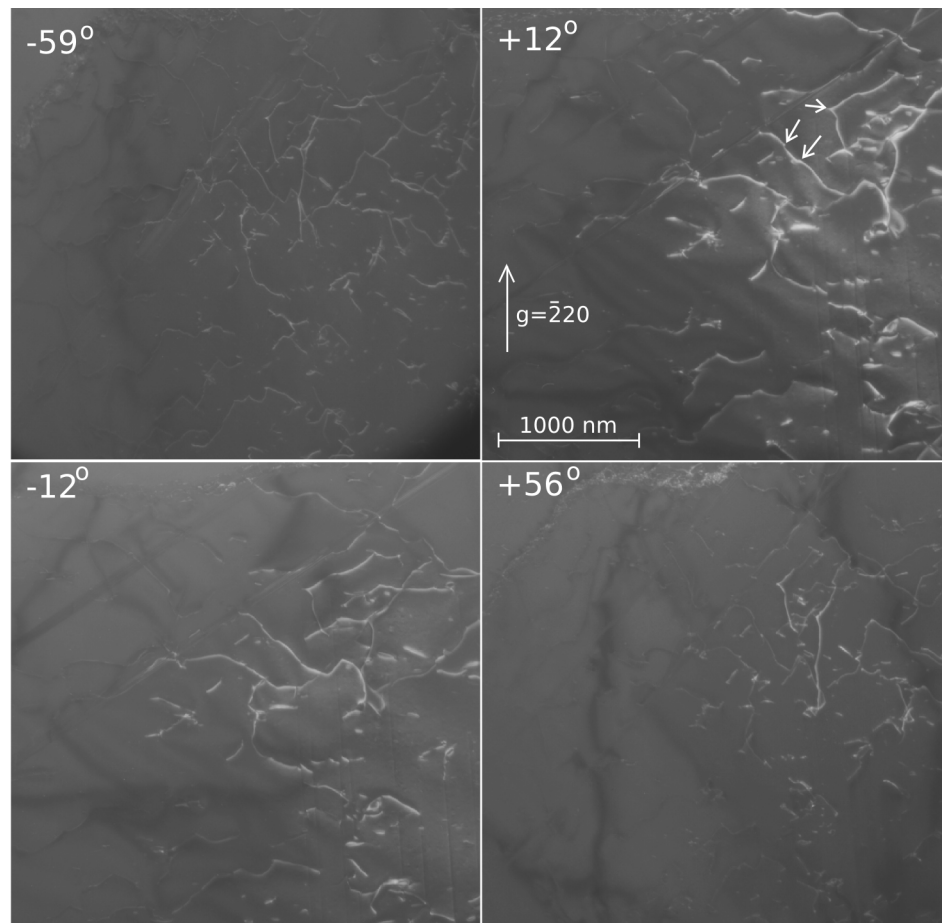


Figure 3.19: Examples of images from WBDF tilt series from TiAl specimen. At this magnification the typical separation between dislocations in a four-bundle should be just visible; these dislocations are in the $L1_0$ matrix. Arrows mark examples of cusps where part of the dislocation has cross-slipped out of the slip plane. Finding the plane onto which this cross-slip occurs is also an unsolved problem for this material. [90]

between adjacent images was accurately based on the dislocations' shift, not on thickness fringes that needed to be filtered out. Reconstruction was then carried out using SIRT with 30 iterations in Inspect3DTM.

3.5.3 Reconstruction

The reconstruction from this tilt series gives very good contrast with barely any background noise. This prevents direct observation of sample thickness from the reconstruction, previously done by measuring between step changes in the low-intensity background of the reconstruction, but improves clarity of the dislocations. The dislocations are distributed mostly in the centre of the foil (Figure 3.20), which could be expected, because dislocations in the L1₀ matrix are quite mobile so dislocations close to the surfaces of the sample will have escaped during sample preparation. They are also less elongated perpendicular to the sample plane than in other tilt series; this was probably from the improvement in achievable alignment quality.

A convenient feature is seen at A in Figure 3.20 — two dislocations moving in different directions (indicated by the bowing in the dislocation line) approach very closely in depth (Figure 3.21). In the reconstruction, these sections are separated by $54nm \pm 4nm$. The separation at this point appears close to the practical depth resolving power of the technique - there is some high value part between the two dislocation sections that does not reach the background elsewhere, so the two features are close to overlapping. This appears to be a relatively poor resolution figure, but the magnification chosen was low.

The out-of-plane elongation of the dislocations in this tilt series is interesting. Though the dislocations are not straight and their cross section cannot be conveniently sampled by summing along their length as those in the GaN tilt series, cross sections of the two clearest dislocations at single points are shown in Figure 3.22. The elongations of these dislocations out-of-plane are 1.5 for B and 1.9 for A. The error in these elongations, from error in calibrating the scale and in measuring the widths, is 0.4. The missing wedge elongation (Equation 2.5) for this tilt range is 1.57; these elongations

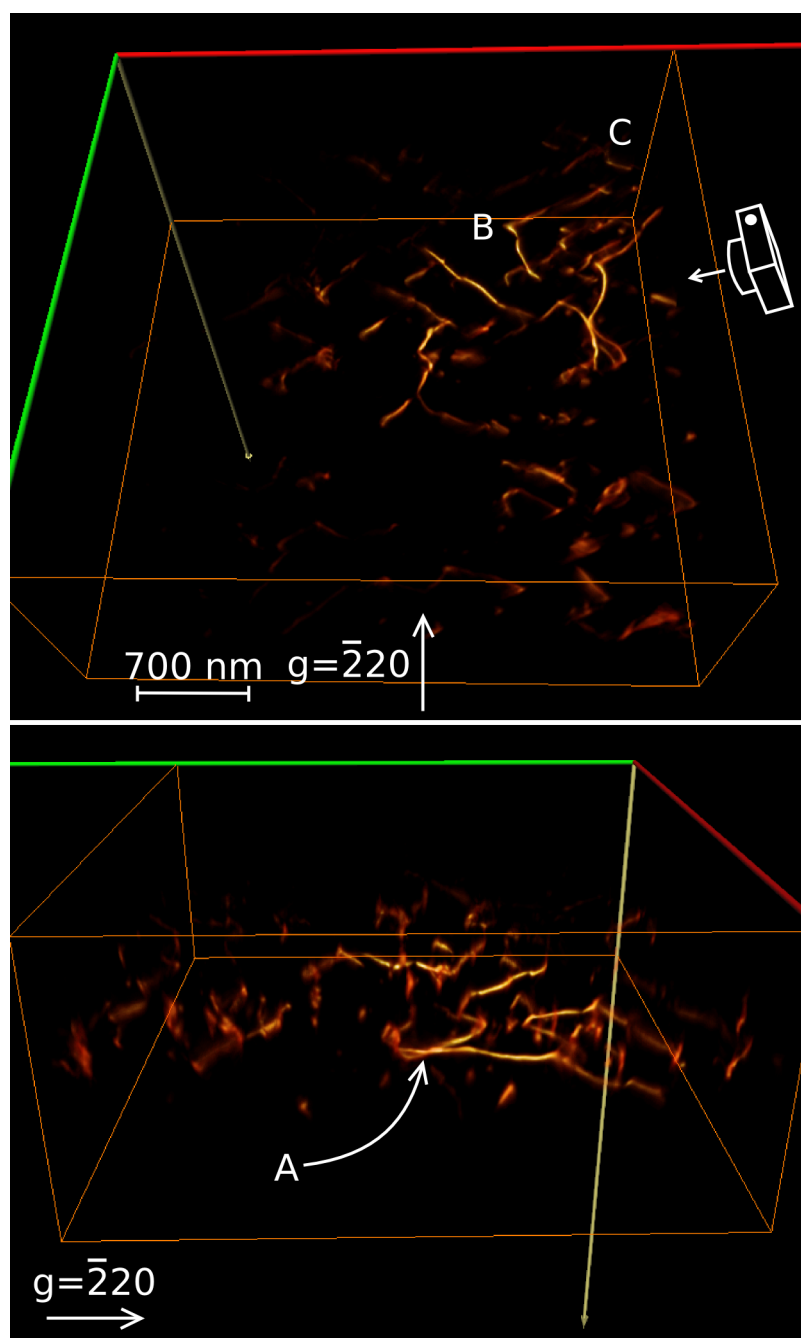


Figure 3.20: Top: plan view of TiAl weak-beam reconstruction. Bottom: inclined view from camera position marked on plan, showing dislocations with little elongation perpendicular to the foil plane. Movie of tilt series is also found on DVD supplied.



Figure 3.21: Closer view of the feature marked A in Figure 3.20 seen from side of reconstruction. The marked point shows two dislocations approaching, separated by close to the resolution of this reconstruction.

are within the margin of error of this figure. It appears that anisotropy elongation has a negligible effect in this tetragonal material compared to the missing wedge effect. As an example of dislocation tomography, this shows how clear the contrast can be if the area and weak-beam diffraction condition are carefully chosen and aligned to minimise background variation and optimise contrast.

In terms of material properties this reconstruction is intriguing. The dislocations present are in the $L1_0$ matrix, not in a region of Al_5Ti_3 superstructure; the ≈ 25 nm spacing of dislocations in a four-bundle would translate to ≈ 5 pixels in the images in Figure 3.19, comparable to the image width of a dislocation, and the lines would certainly be broader if they were four-bundles. The cusped appearance of these dislocations is familiar in the literature, and the cusps are where small sections have cross-slipped out of the slip plane. Finding the plane onto which they cross-slip from conventional 2D images has been problematic [92], but with a 3D dataset this could be measured directly. On attempting to measure this, however, it was found that most of the cusps appear to lie in the (111) plane of the sample; the few that do not (such as the dislocations approaching point A in Figure 3.21) are too wide and too few in number to measure the plane they lie in with

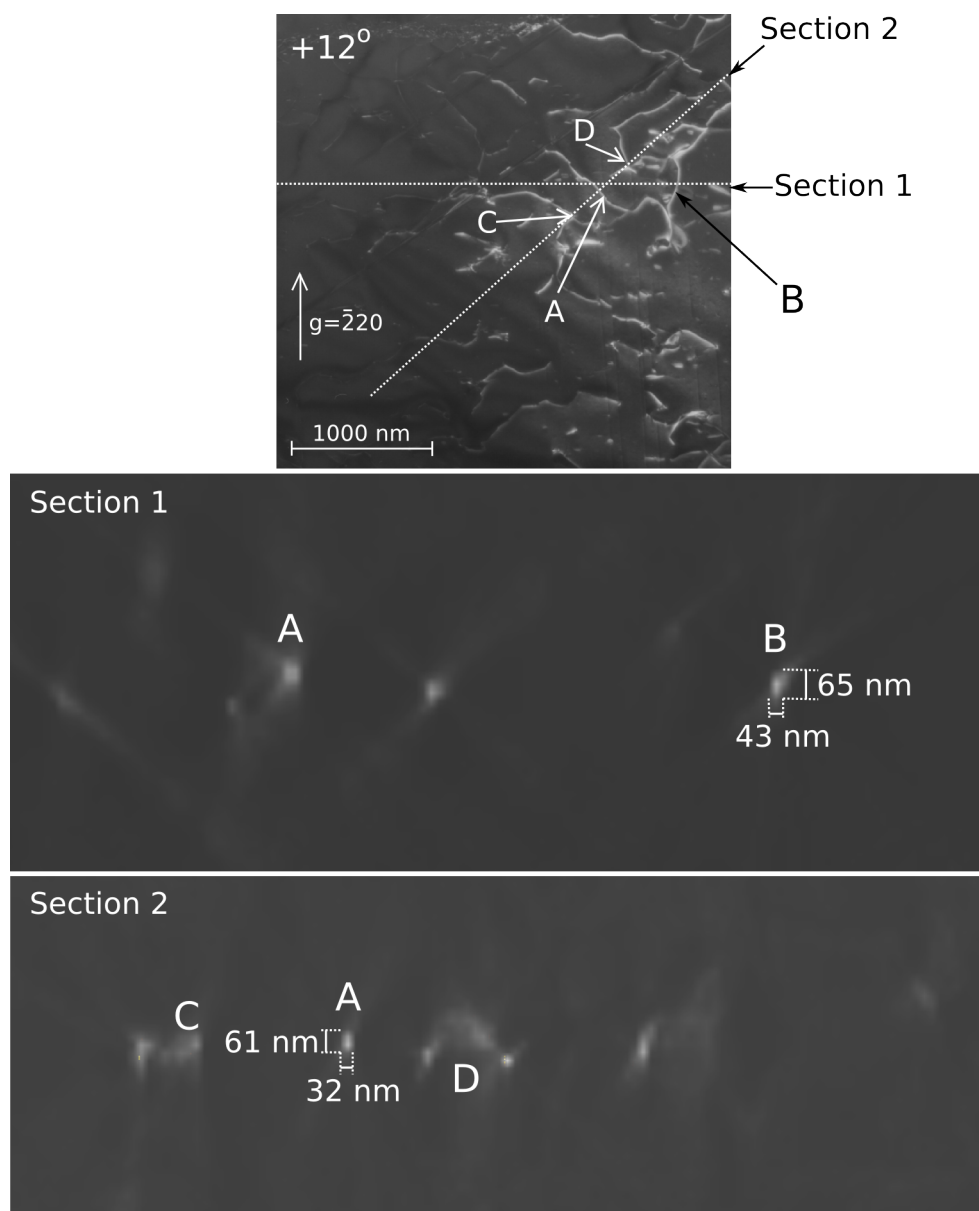


Figure 3.22: Sections of the TiAl WBDF reconstruction showing dislocation widths. The elongations for dislocations A and B are 1.9 and 1.5 respectively (± 0.4); this is attributable to the elongation factor from the missing wedge for this tilt range.

reasonable accuracy. Higher magnification tilt series from different regions of the sample, however, could be promising for this purpose.

3.6 Problems in using WBDF images for dislocation tomography

The main experimental problem in WBDF tomography is keeping the diffraction condition as constant as possible over the tilt range. To test the effect of misaligning this, three tilt series of weak-beam images of a dislocation were modelled using the dislocation image simulation program CUFOUR, applying different amounts of misalignment by moving the Laue circle centre (the centre of the circle where the Ewald sphere intersects the reciprocal lattice plane perpendicular to the beam) along the systematic row with tilt. The measure of tilt axis misalignment for weak-beam condition $\mathbf{g}(n\mathbf{g})$ is the difference in n between the two ends of the tilt series; for the initial condition of $\mathbf{g}(3.5\mathbf{g})$, a misalignment Δn of 1 would give $\mathbf{g}(3.0\mathbf{g})$ at the negative end of the tilt range and $\mathbf{g}(4.0\mathbf{g})$ at the positive end. Simulations were done for $\Delta n = 1$, $\Delta n = 2$ and $\Delta n = 0$ (perfectly aligned). As the diffraction condition is changed, the excitation errors for the beams in the calculation must change also, so these were calculated for each new tilt angle using a program adapted from the part of CUFOUR that calculates excitation errors for a single image. The dislocation modelled was a mixed dislocation, $\mathbf{b} = \frac{1}{2}[1\bar{1}0]$ with line direction $[0\bar{1}1]$ in an Al crystal of foil normal $[001]$; it passed through the crystal at 45° to the surfaces. A tilt range of -45° to $+45^\circ$ was used, to make the simulation and reconstruction process simple; the tilt angle was changed by lengthening the zero tilt beam direction, and adding integer multiples of a small vector perpendicular to the tilt axis to it (or subtracting, to achieve negative tilt). This gave a non-uniform distribution of tilt angles following the Saxton scheme [93]; future versions of the script should allow uniform distribution of tilt angles also.

To avoid the incorrect tilting problem encountered in the stacking fault simulation, the sample was ‘tilted’ along the projection of the dislocation

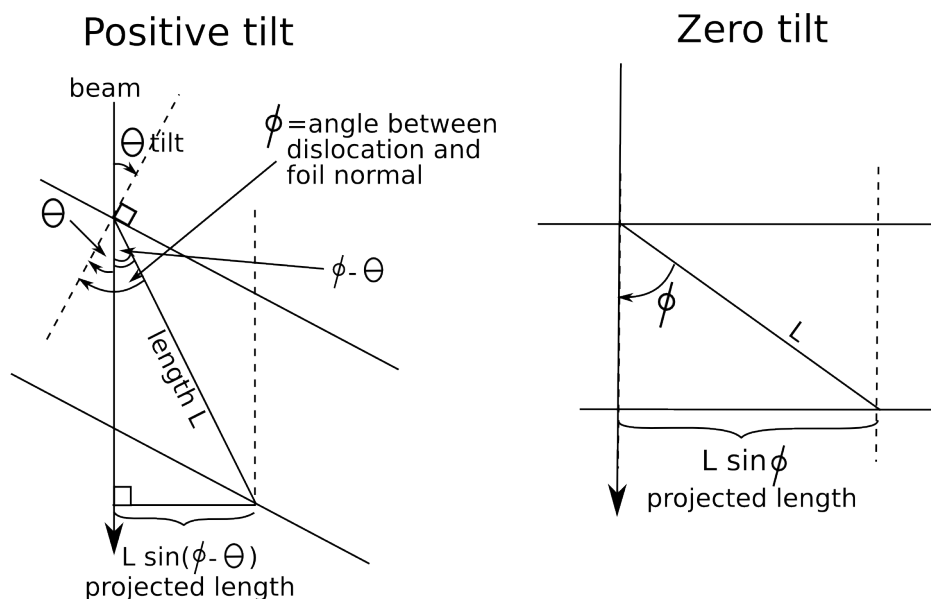


Figure 3.23: Projected length of dislocation inclined at ϕ to the foil normal, at tilt θ . At negative tilt (not shown) the expression still holds; angle $\phi - \theta$ becomes larger as tilt becomes more negative and projected length increases.

direction (horizontal axis of the image) — [010] in this case — so that the tilt axis and \mathbf{g} lie perpendicular to the dislocation direction, so $\mathbf{g} = [200]$ must be chosen. In this orientation, the dislocation should get shorter and longer as it is rotated closer to, or further from the foil normal respectively; the projected length of the dislocation should scale as in Figure 3.23 giving Equation 3.7 for the projected length.

$$L_{proj} = \frac{L \sin(\phi - \theta)}{L \sin \phi} = \frac{\sin(\phi - \theta)}{\sin \phi} \quad (3.7)$$

However, CUFOUR scales the dislocation image to take up a specific fraction of the image; it stretches or shrinks the image to fit. The solution to this problem is elaborated on here; it was implemented retrospectively for the $\mathbf{g} = 200$ stacking fault tilt series after the problem was realised.

An initial attempt was made to correct for this by asking CUFOUR to allocate a different fraction of the image (scaled by the factor in Equation 3.7) to the dislocation, but this scaled the width of the dislocation by the

same factor, equivalent to changing the magnification, which is not what happens in a real experiment. Instead CUFOUR was allowed to allocate the central quarter of the image to the dislocation, and the calculated images were then stretched or squashed in the length direction only according to Equation 3.7 before reconstruction. Examples of images from the final tilt series are sampled in Figure 3.24. The images do not include thermal diffuse background, which is enhanced around defects [94] and adds a less oscillatory increase in intensity around the dislocation — explored more fully in the next two chapters. Reconstruction was carried out using conventional SIRT with 30 iterations, using FEI’s Inspect3DTM.

The results, shown in Figure 3.25, show that misalignment of the tilt axis has a profound effect on the reconstruction. The perfectly aligned tilt series produces a thin dislocation with dynamical fringes, though not at the correct inclination to the surface; as the misalignment increases, the shape and inclination deviate more, and it becomes more difficult to see the path of the dislocation. This distortion from the expected inclination and shape is also seen in the threading dislocations in the GaN WBDF reconstruction; the misorientation of $\Delta n = 1.2$ in that tilt series probably contributes to their poor representation in the reconstruction. It is therefore important to carefully align the tilt axis with the systematic row before acquiring a tilt series. It is also worth noting that the same limitations in simulation software that apply to this tilt series, also apply to the tilt series of a stacking fault in Section 3.4, in particular when the stacking fault is turned in the direction parallel to the dislocations bounding it and the contrast is held to produce a misleading reconstruction because the fringes move along the tilt direction. A similar correction was therefore applied, also taking account of the change in projected distance between intersection points of the dislocations with the surfaces; this is included by CUFOUR when an image with two dislocations is rescaled to the required proportion.

The displacement of the weak-beam image to one side of the dislocation core by 1-5 nm [76] would be a problem at higher resolution and small dislocation spacing. This displacement is affected by changes in the excitation error s and sample tilt [42]. At the low magnifications so far used for

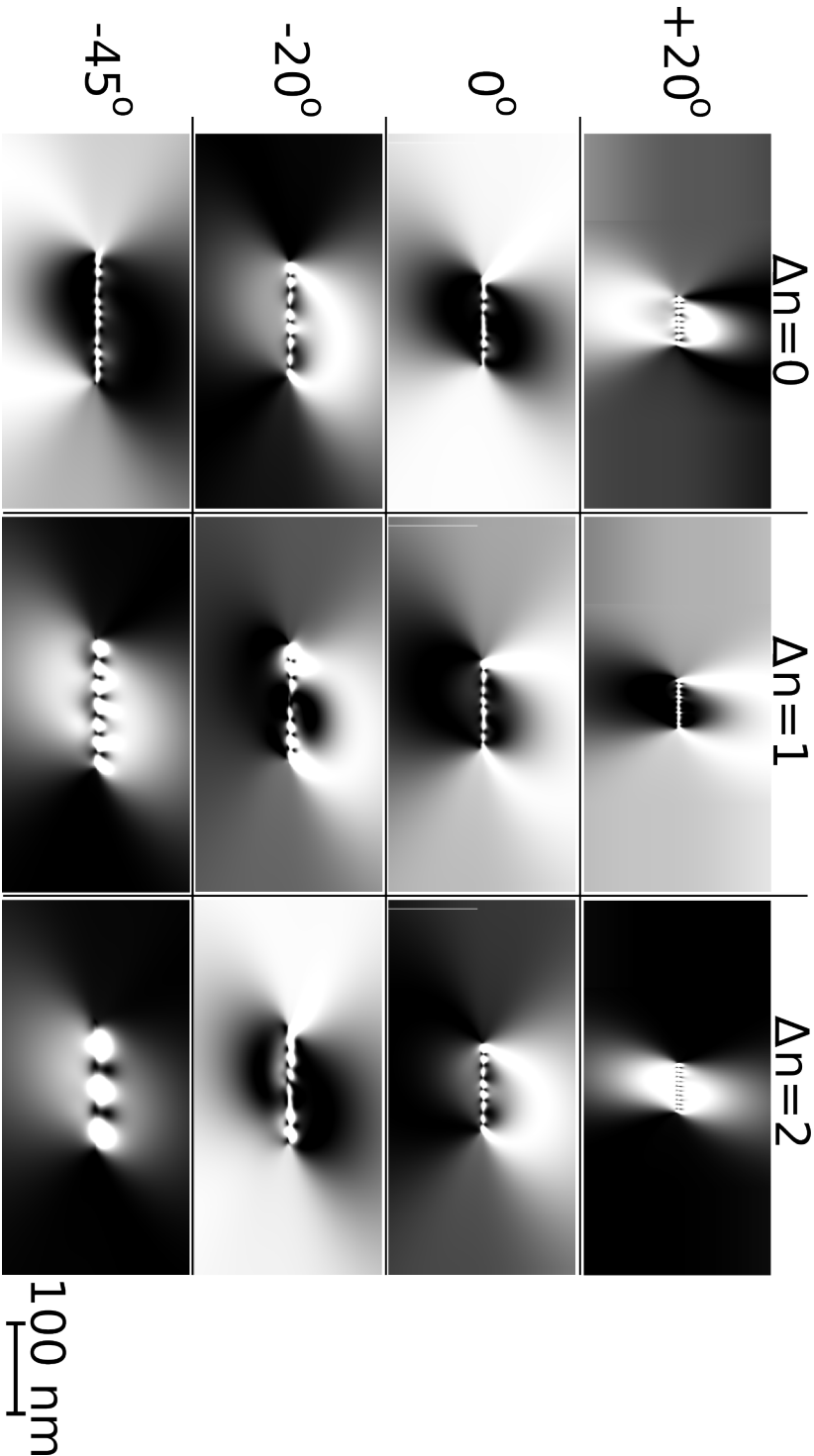


Figure 3.24: Images from the simulated tilt series to study tilt axis misalignment: left, aligned; centre, diffraction condition differing by \mathbf{g} from one end of the tilt range to another; right, diffraction condition differing by $2\mathbf{g}$ from one end to another, i.e. each end is \mathbf{g} away from the condition at the middle.

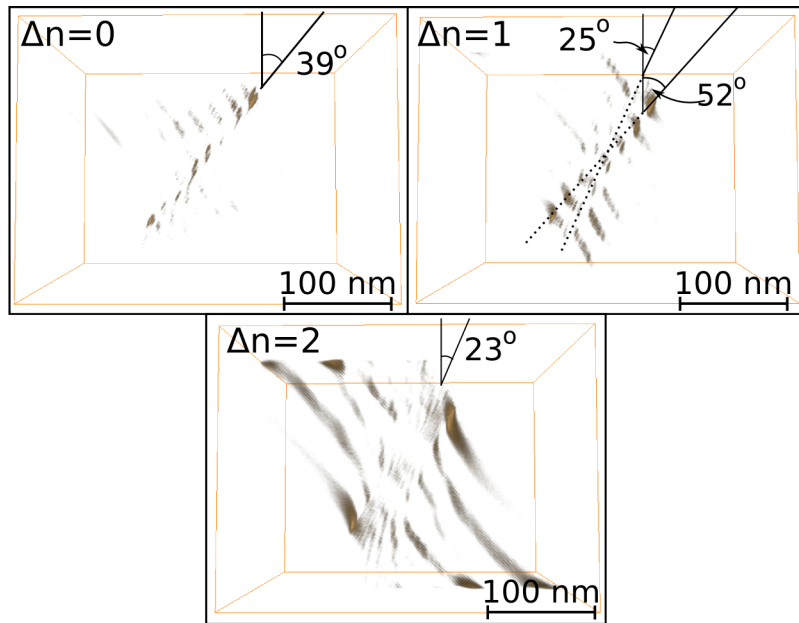


Figure 3.25: Side views of reconstructions of misaligned weak-beam dark-field tilt series of a single dislocation inclined at 45° to the foil plane, for misalignments given at top left of images.

WBDF dislocation tomography this is not a significant error except where dislocations approach closely; at these points the **separation** of the two dislocations is not as much in error as the positions of the images, with error of the order 1 nm [76], because the image in \mathbf{g} will be displaced to the same side of each dislocation.

3.7 Conclusions and further work

The experiments in this chapter show that weak-beam dark field tomography can be practically achieved to recover the 3D distribution of dislocations. The results for defects with parts that give fringed contrast such as stacking faults or microcracks are not so promising; alignment is difficult and the success of reconstructions is variable. The reason for this variability in reconstruction has been analysed and the hypothesis put forward that the reconstruction quality is impaired by movement of fringes along the image as

the tilt angle changes; however, more work is needed to test this. The effect of misorientation between the tilt axis and the systematic row was explored in simulation and the misorientation was found to affect dramatically the inclination and shape of reconstructed dislocations, making this an important additional alignment to perform correctly during WBDF tomography.

Further work required to advance the material presented in this chapter is as follows:

- Derive a theoretical criterion for the best orientation to choose for stacking fault tomography if fringe movement is to be as similar as possible to the movement expected from a flat striated plane.
- Adapt current simulation tools to rotate the sample realistically and enable modelling of arbitrary tilt axis orientations — if the theoretical criterion has errors in, the simulations will highlight this and ensure experiments can be carried out based on a correct theoretical prediction. Also during this step, the method of changing the beam direction, for tilt series modelling, needs to be improved to achieve regular angular increments and arbitrary tilt range.
- Stacking fault WBDF tilt series should be acquired, at a higher magnification such that they are comparable with simulations and suitable for testing the hypothesis.

Chapter 4

ADF STEM for dislocation tomography

4.1 Basic concept

While weak-beam dark-field tomography of defects has been shown to work in some cases, the technique has a number of flaws. As reported in the Chapter 3, dynamical effects cause problems in reconstructing microcracks, stacking faults and steeply inclined dislocations, and thickness fringes impair alignment to some degree. It was pointed out by Prof. Midgley that scanning transmission electron microscopy (STEM) might give defect contrast with fewer dynamical features [32, Chapter 22], so this avenue was explored experimentally and the results are reported in this chapter. Additionally, with WBDF images it has not been possible to use the standard acquisition software for electron tomography, FEI's Xplore3DTM, because a fringed background prevents automatic relocation of the area of interest after any sample drift that occurs when tilting; this problem conveniently does not occur with STEM defect images.

In STEM, the electron beam is converged typically to a point of the order 0.3-30 Å in diameter, illuminating only a small number of crystal unit cells at once. In dynamical terms, this excites mainly localised states [95] which at a zone axis can result in preferential channeling down atomic columns [96].

This small convergent beam is scanned across the sample. The exit wave in the far field forms a CBED pattern that is constantly evolving as the beam scans; thermal diffuse scattering is also present. The STEM detector(s) are placed in the diffraction plane (in the far field), and not the image plane as for conventional TEM. The pixel intensity in the resultant image is equivalent to the total diffraction pattern intensity falling on the relevant detector as the beam passes through that point on the sample.

A STEM usually has two configurations of STEM detector to choose from. The bright field detector is circular and centred on the optic axis to receive intensity predominantly from the bright field disc; in some microscopes the beam can be tilted to allow the bright field detector to receive intensity from a dark field beam instead. The other choice is an annular dark field (ADF) detector centred on the optic axis; this is the detector used for imaging in this chapter and the geometry is illustrated in Figure 4.1. As the camera length of the imaging system is varied, the range of scattering angle received by the detectors changes. Features in the specimen can change the ADF signal by changing the angular distribution of scattered intensity, so that more or less intensity falls into the angular range collected by the ADF detector. Dislocations are an example of a feature that can redistribute intensity in this way. In a dark-field STEM image from one spot, dislocations give images broader and more diffuse than WBDF images, but the image has less diffraction contrast than conventional dark-field images [32, Chapter 22]. When an ADF detector is used, all spots for which the dislocation is in contrast contribute to image intensity. Defects also affect thermal scattering in a number of ways. The atom sites in the strain field have different environments in which to vibrate [79]. The static displacement around the dislocation also contributes TDS-like scattering, sometimes referred to as Huang scattering [94], and the net effect is to redistribute intensity to higher angles. As shown in Figure 4.2, the balance between elastic and TDS/Huang scattering contrast depends on the angle subtended by the annular detector. For tomography based on mass-thickness contrast, the ADF detector is placed to collect intensity at scattering semiangles greater than 30 mrad, entirely in the TDS regime; at these angles, Rutherford scattering is also

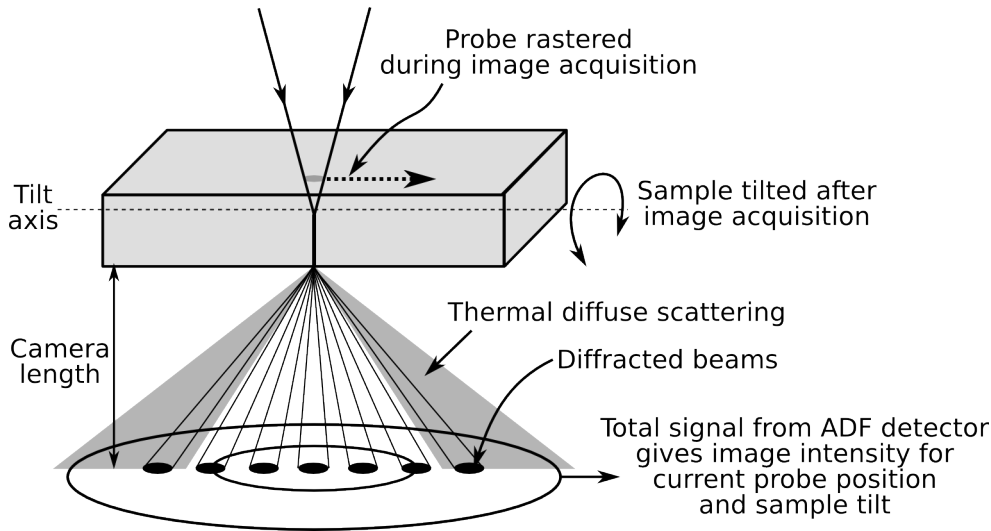


Figure 4.1: Schematic showing the geometry of the ADF STEM approach to dark-field tomography.

significant and useful for mass-thickness contrast since $I_R \propto Z^2$ [97].

For our tomography of defects, the ADF detector has been used at collection semiangles much closer to the threshold at which elastic and thermal scattering cross in Figure 4.2. The tilt axis was always set parallel to a systematic row, as for the weak-beam dark-field tilt series, to ensure that some \mathbf{g} was kept excited throughout the tilt series, but the sample was not tilted to achieve a strict weak-beam condition as before. This chapter summarises the results of three ADF STEM defect tomography experiments; the discussion is kept brief here. The theoretical basis of ADF STEM defect contrast and the implications for tomography are explored properly in Chapter 5.

4.2 STEM tomography of GaN

Dislocation tomography using ADF STEM was first attempted using the same GaN sample as used in Chapter 3. At first, in-house tomography programs were used but little success was achieved in alignment and reconstruction. In the course of developing WBDF tomography, a program

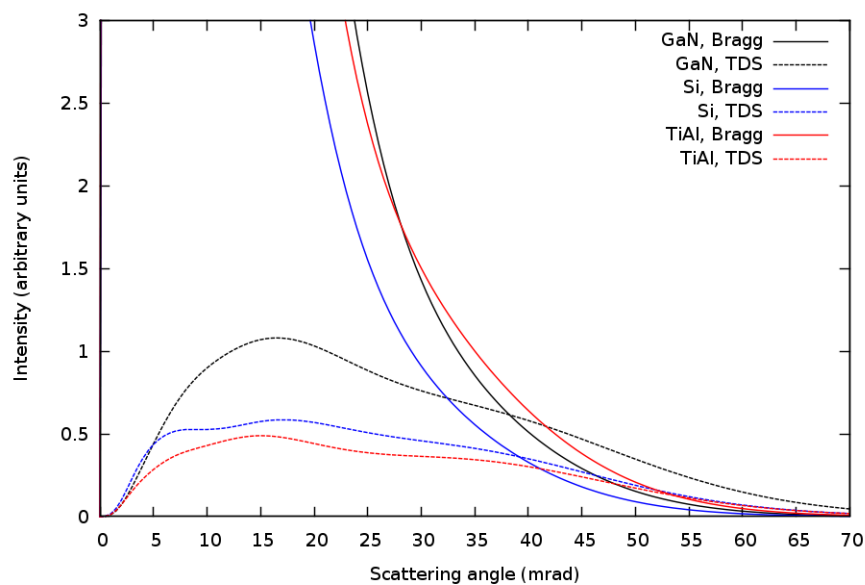


Figure 4.2: Plot showing angular distribution of intensity from elastic and thermal diffuse scattering for the three materials used in these experiments, from expressions in [98]. Thermal diffuse scattering becomes dominant once elastic scattering has experienced a sharp decrease as scattering semiangle increases; the angle at which this occurs depends on the material. The crossover between Bragg and TDS intensity being greater occurs at 38.2 mrad for GaN, 39.0 mrad for Si and 53.6 mrad for TiAl. More details will be given in Section 5.2.2.

was written to convert tilt series from open source formats into the mrc format used by FEI's standard tomography software; a successful reconstruction was achieved using this software.

4.2.1 Procedure

A Tecnai F20 FEGTEM fitted with a STEM BF/DF detector pair (diameter of BF detector and inner diameter of DF detector 7 mm, outer diameter of DF detector 21 mm) was used by the author and JSB to collect STEM tilt series at 200 keV. Dislocations near a crack in the sample of relaxed GaN were imaged at an angular interval of 2.5° over the range $\pm 60^\circ$, giving 49 images in a series. The convergence angle (from CBED patterns taken at five different tilt angles over the tilt range) was $6.18 \text{ mrad} \pm 0.04 \text{ mrad}$. Three tilt series were taken over this range:

- bright field images with camera length of 680 mm (collection angles 0-5.1 mrad)
- bright field images with camera length of 100 mm (collection angles range 0-34.0 mrad)
- dark field images with camera length of 100 mm (collection angles 34.0-105.0 mrad)

These camera lengths were chosen heuristically for optimal clarity of images, from a preliminary survey of different camera lengths at zero tilt and high tilt. Images were taken manually using the Tecnai Imaging and Analysis (TIA)TM software; examples are shown in Figure 4.3. The ADF images were sharpened with a 20-pixel kernel (Section 1.4). Alignment and reconstruction were carried out using Inspect3DTM and a successful reconstruction was achieved using SIRT with 30 iterations.

4.2.2 Results

The ADF STEM reconstruction (in voltex representation, where the value of a volume pixel is rendered by colour and transparency with a range from

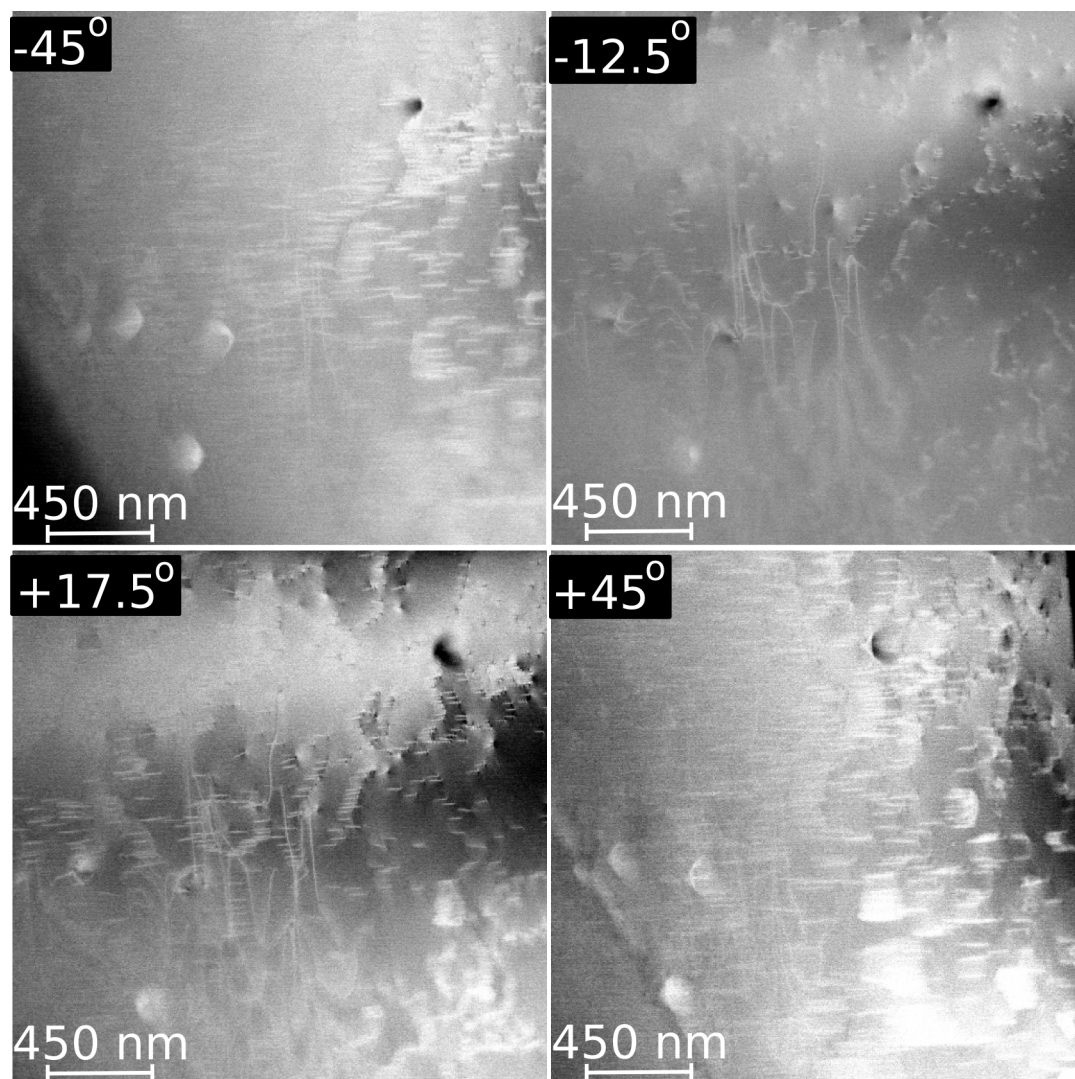


Figure 4.3: Images from GaN ADF STEM tilt series, before processing. Contrast is sharper in a band across the centre of the image. In-plane dislocations appear more diffuse than threading dislocations.

black and transparent at the lowest value, through reds and oranges, to white and opaque for the highest values) is shown in Figure 4.4 and compares quite favourably to the WBDF reconstruction from the same sample. Threading dislocations are reproduced very clearly; they are not striated along their length, and appear to thread straight through parallel to the foil normal (Figure 4.5), both problems that were present in the WBDF reconstruction. The threading dislocations are lenticular in shape and, in cross section, are revealed to have an intense core with a weaker region around them, of 16×80 nm at the thickest point (an elongation of $5\times$ in the direction perpendicular to the tilt axis).

In-plane dislocations are also present as lines, even when viewed from in the foil plane (Figure 4.6). They are thicker than in the WBDF reconstruction, with elliptical axes of 22×60 nm (elongation of 2.7 in the out-of-plane direction). The same structure is present as for the threading dislocations: an intense core and a diffuse surrounding region, but surrounded by the characteristic X-shaped cross section imparted to pointlike objects after backprojection as an effect of the missing wedge, not entirely removed by SIRT.

4.2.3 Discussion

The elongation factor of in-plane dislocations in this STEM ADF reconstruction is greater than the elongation factor of 1.55 predicted from the missing wedge, as was found for the WBDF GaN reconstruction. This suggests that additional elongation due to anisotropy operates in the STEM case as well as in WBDF; however, the widths of these dislocations in the reconstructions are very small, on the scale of 5-30 volume pixels, so small variations in image width will have a proportionally large effect on the measured elongation. To further investigate this elongation, a higher magnification tilt series would be more appropriate.

In-plane dislocations are 2-3 times as wide in this STEM tilt series as in the WBDF tilt series from this sample. In many images from the tilt series, in-plane dislocations appear wide and fuzzy; this is a known disadvantage

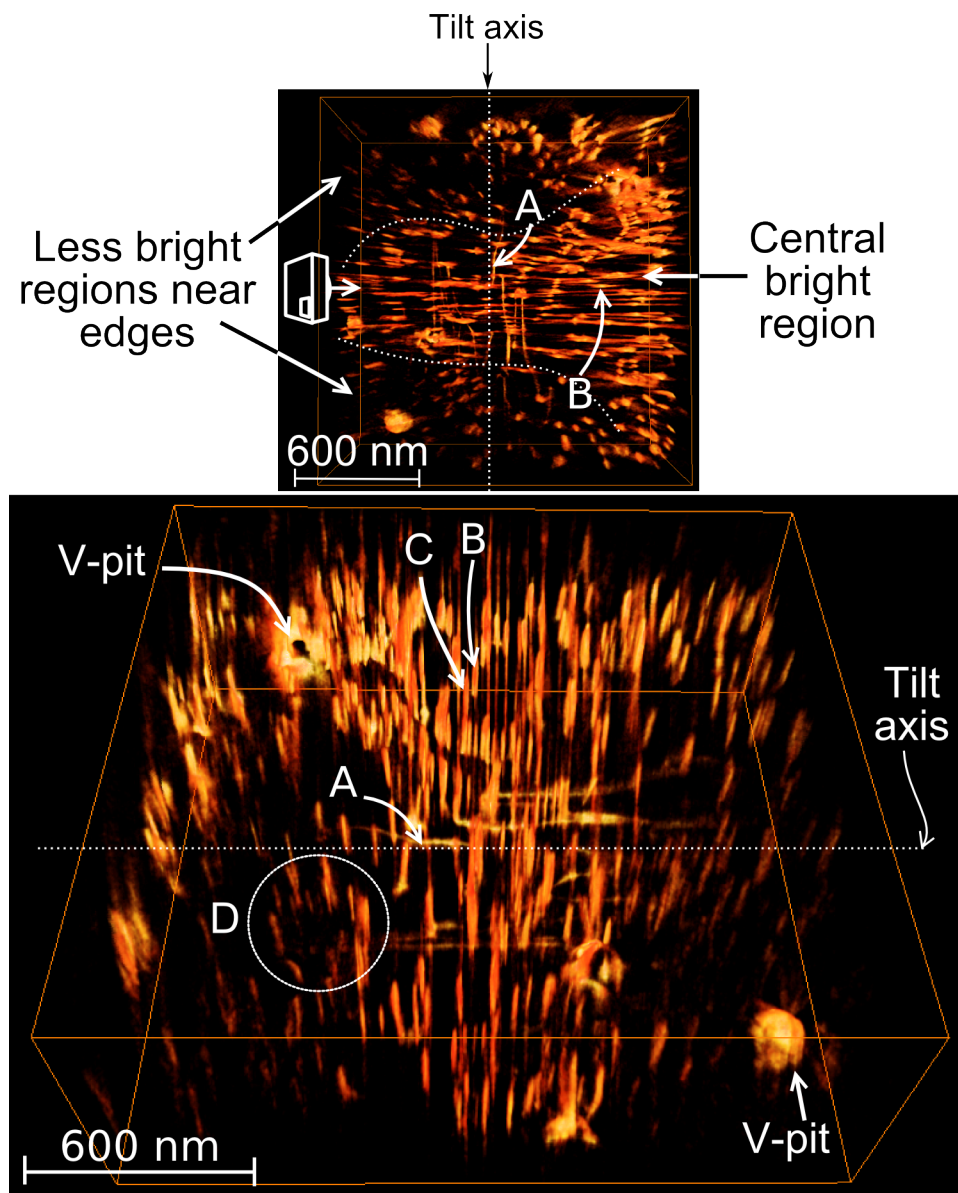


Figure 4.4: Overviews of GaN ADF STEM reconstruction in voltex representation. Top: plan view. Bottom: oblique view, taken from camera position shown in top image. Labels A, B and C refer to dislocations further analysed in the text, and D indicates a ring of threading dislocations nucleated at a misalignment domain during growth of the original GaN film. In-plane dislocations are more intense and well-defined in the central band of the reconstruction than the sides (indicated by the dotted line in the top view). The tilt axis position is also indicated. The objects labelled are V-pits that are known to develop at threading dislocations of screw character in GaN [99].

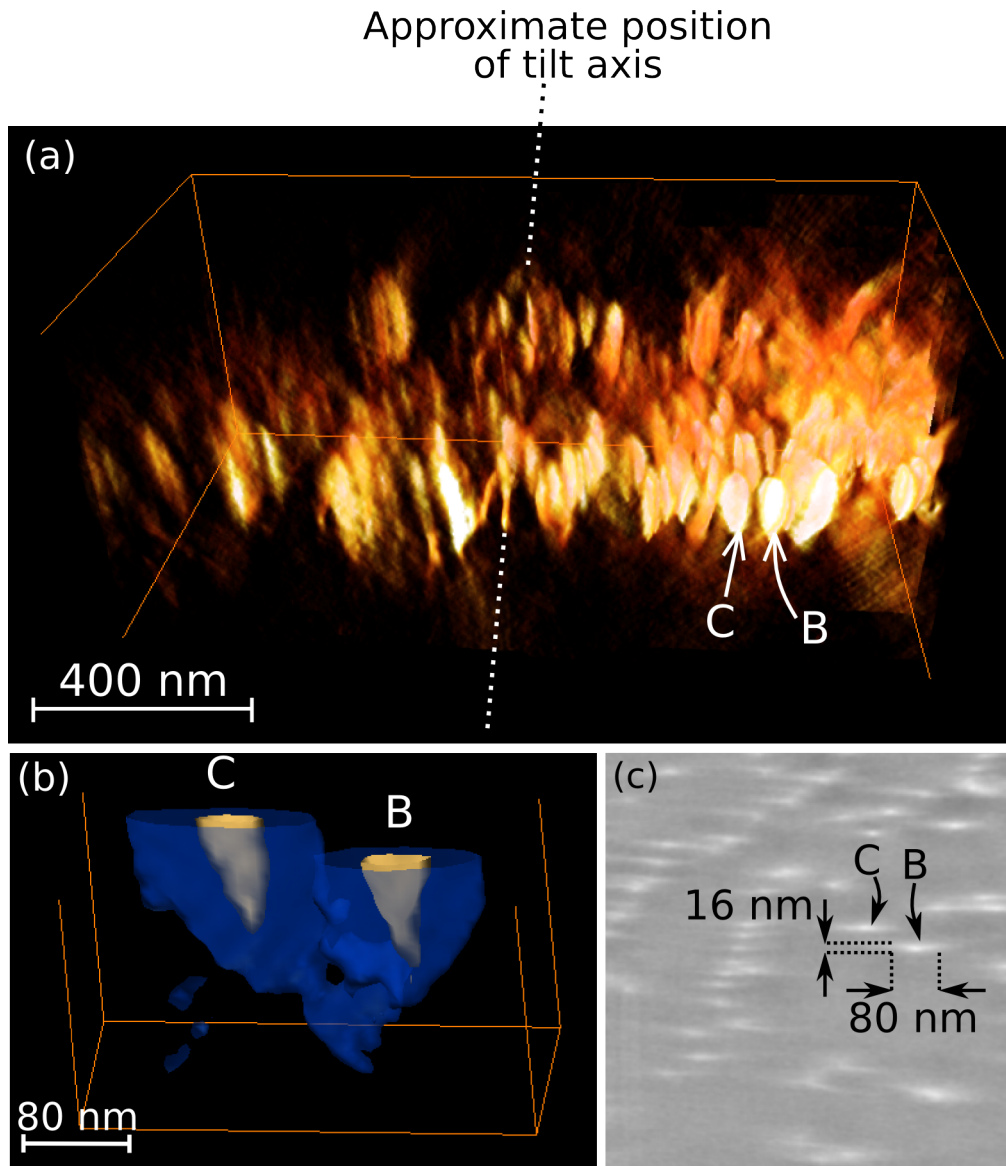


Figure 4.5: Threading dislocations in the GaN ADF STEM reconstruction. (a) Reconstruction seen obliquely in voltex representation, with the near portion of the reconstruction cut away to show the lenticular shape of the threading dislocations. (b) Threading dislocations B and C in isosurface representation; the blue shell is close to the edge of the diffuse surrounding region, the yellow shell marks the approximate boundary of the central high-value part. The dislocations have been cut in half to show the cross-section more clearly. (c) Orthoslice through the same dislocations in the foil plane.

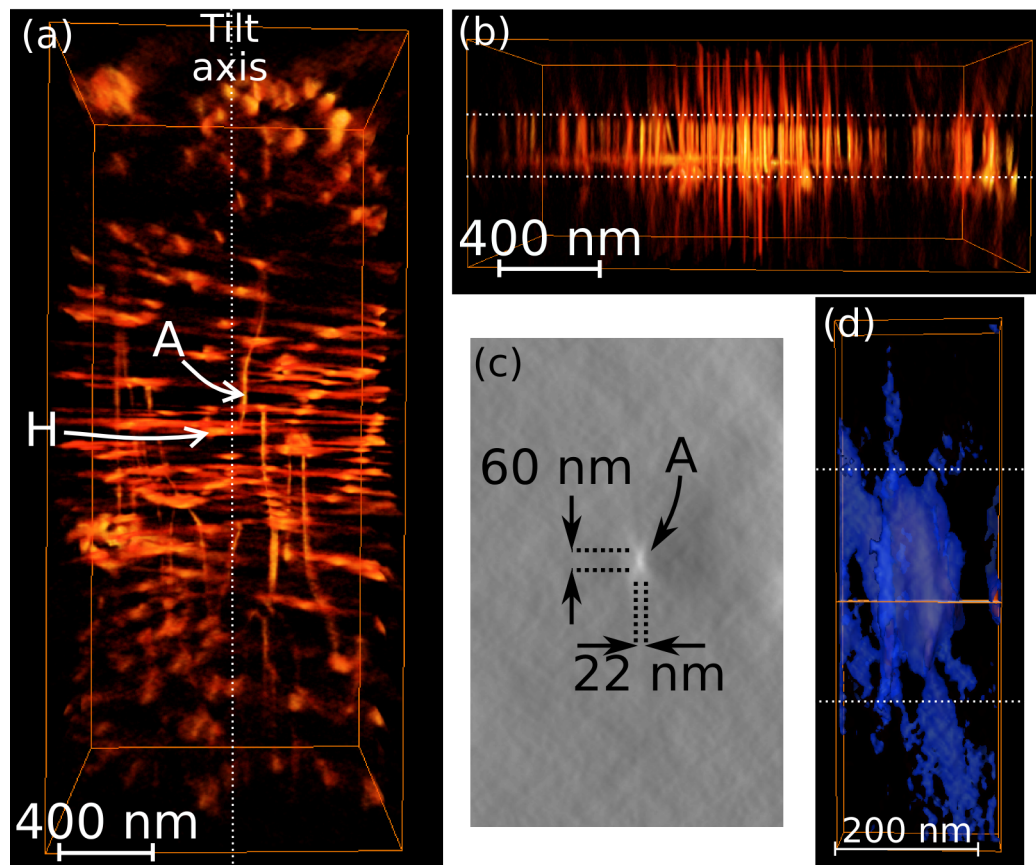


Figure 4.6: (a) Subsection of reconstruction containing the in-plane dislocations, in voltex representation. (b) Side view of the same subsection, showing that the in-plane dislocations experience little enough elongation to appear as lines. The white dotted lines in (b) show the approximate locations of the sample surfaces. The central bright region contains vertical striations that extend beyond the surfaces of the sample. (c) Vertical orthoslice through the subsection, intersecting dislocation A at the point indicated by the label in (a). (d) One of the vertical striations that extend beyond the sample boundaries (approximately shown), in isosurface representation. The intensity at which the isosurface is taken is close to the intensity at the edge of the broad diffuse intensity surrounding the dislocations, i.e. these striations are of moderately low intensity when taken individually. Their positions coincide with dislocations at which black-white lobes of surface relaxation at occur in images close to zero tilt, an effect that occurs for dislocations with some screw component [1].

of STEM compared to WBDF dislocation tomography [32, Chapter 22]. The threading dislocations are reconstructed better in STEM than WBDF, without fringing or changes in inclination. These phenomena are caused by dynamical contrast, directly in the case of fringe contrast and indirectly through the effects of tilt axis misorientation and changes in \mathbf{s} for inclination. For STEM, changes in \mathbf{s} will be less important because the excitation errors for each diffraction spot falling on the ADF detector are different already, and therefore small changes in \mathbf{s} will lead to only marginal changes in STEM contrast.

Features at the edges of the reconstruction are less sharp and less intense than those in a horizontal band of best contrast across the centre. For these conditions, where d is the smallest distance resolvable, say the width of a threading dislocation 16 nm, and α is the convergence angle, 6 mrad, the depth of field should be $\approx 2.6 \mu\text{m}$ according to $D = d/\alpha$ [32]. A sample of ≈ 200 nm thick cannot bend this far over a distance of 450 nm, so it is unlikely that the sample is bent enough to take the top and bottom of the images out of focus.

In some images, for example the $+17.5^\circ$ image in Figure 4.3, the background intensity is higher in these less sharp regions, indicating that between these regions and the good contrast region in the centre there is a thickness difference. This is a familiar shape of thickness variation to expect from the ‘curtaining’ effect seen in ion-milled TEM specimens of semiconductors such as GaN [100]. If there is some aggregate thickness fringe effect for this ADF STEM image, the pattern of thickness fringes will depend on the DF reflections excited at that angle and some combination of their two-beam extinction distances determined by their excitation errors (depth periodicity $\Delta z \propto s_{eff}^{-1}$ [32]). The projected lengths of threading dislocations in these regions are longer than in the sharp region, and since these dislocations are known to run down [0001], the approximate difference in thickness can be calculated from this difference in projected length.

The thickness of the specimen in the thin sharp region can be measured as $160 \text{ nm} \pm 10 \text{ nm}$ from the reconstruction as the points where the threading dislocations terminate. Because they are parallel and are tilted by the same

angle, the lengths of two dislocations L_1 and L_2 and their projected lengths in an image P_1 and P_2 are related by $\frac{L_1}{L_2} = \frac{P_1}{P_2}$. Three dislocations were chosen in the thin zone and three dislocations at the boundary of the thick zone at approximately the same background intensity, and their projected thicknesses compared for three images at large tilts; the thickness at the boundary of the thick zone was then computed to be $250 \text{ nm} \pm 16 \text{ nm}$. The contrast of dislocations in conventional DF images deteriorates with increasing specimen thickness because of thermal diffuse scattering (anomalous absorption); as the ADF STEM detector is positioned to receive the thermal diffuse scattered electrons toward the outer collection angle of the detector, it is reasonable to expect thermal diffuse scattering to not only degrade diffraction contrast from the dislocations, but to raise the background intensity proportionally more than for a simple DF image. This tilt series uses the largest selection of detector collection angle of the three ADF STEM tilt series; this enhancement of the degradation of dislocation contrast with thickness may be an example of what occurs when the collection angle is too large.

The origin of the lenticular shape of the threading dislocations in the STEM reconstruction demands further investigation. Elastic anisotropy is unlikely to contribute to the lenticular shape of the threading dislocations, since it was found in Section 3.3.2 to have an insignificant effect on the peak positions of threading dislocations in reconstructions from WBDF images.

To concentrate on the two dislocations B and C, it can be seen that at most larger tilts they appear contracted at the top and bottom of the foil, though at occasional tilt angles they are thin along their whole length (Figure 4.7). This is a more obvious cause of their lenticular shape. The origin of this shape is yet to be explored rigorously; a strong possibility is some thickness-dependent cancelling effect between the fringing along the dislocation images contributed from each dark-field disc. This would be more severe at surfaces where the fringing is more pronounced [3], giving a lenticular shape in the resulting ADF STEM dislocation image.

Relaxation contrast where dislocations with some screw component meet the sample surface is another possible contributor to the lenticular reconstructed dislocations. In conventional dark-field images, lattice relaxation

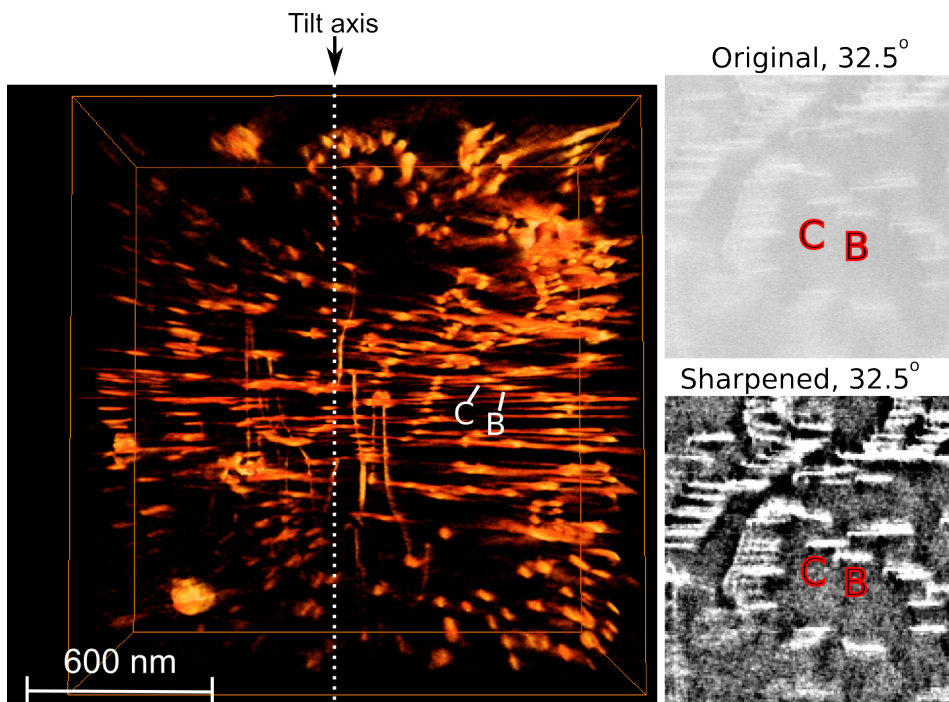


Figure 4.7: Threading dislocations in the STEM GaN tilt series appear thin and of roughly uniform length at some tilt angles, but at most tilt angles above 15° the dislocation images are wider in the centre and contracted near the surfaces, though it can be seen that they are only ≈ 5 -15 pixels wide at this magnification. This effect is present in the original and sharpened images, shown for -32.5° on the right, but the wide contrast in the centre fades smoothly into the background in the original images.

where a threading dislocation with some screw character intersects the surface appears as a pair of bright and dark lobes extending perpendicular to \mathbf{g} [101]. The tilt axis is oriented with respect to the crystallographic axis such that $\mathbf{g} = 11\bar{2}0$ dark field images should contain lobes extending perpendicular to the tilt axis, i.e. along the long axis of the elliptical cross-section of the threading dislocations. On observing the tilt series images as used for reconstruction, however, this appears not to be the cause; for most dislocations the relaxation contrast does not extend as far as the long axis of their reconstructed cross section. Further, in some dislocations the lobed surface contrast appears parallel to the tilt axis (i.e. the wrong direction to cause the non-uniform cross-section), contributed from dark-field discs out of the $11\bar{2}0$ row. The dislocations that show strong surface relaxation contrast in images close to zero tilt, appear to correspond to the dislocations that have the worst out-of-plane streaking, however, especially in the central bright region. This is shown in Figure 4.8.

4.3 ADF STEM tomography of silicon

The sample of indented Si supplied by Prof. Kaneko (Kyushu University), used for WBDF tomography in Chapter 3, was used for STEM tomography. Fortunately, the same microcrack could be located so there was an opportunity to compare directly the two techniques on the same defect.

4.3.1 Sample and experimental details

The sample was from a slice of p-doped single crystal silicon, made using the Czochralski method [102], micro-indented and then deformed in three-point bending at 800°C, resulting in emission of microcracks along $\langle 110 \rangle$ directions that preceded cracks around the indentation [103]. A TEM sample with foil normal [001] had been prepared by those in Kyushu University using ion milling.

A tilt series of ADF images with tilt axis parallel to [220] were taken by JSB and the author, on the Tecnai F20 operating in STEM mode at 200kV.

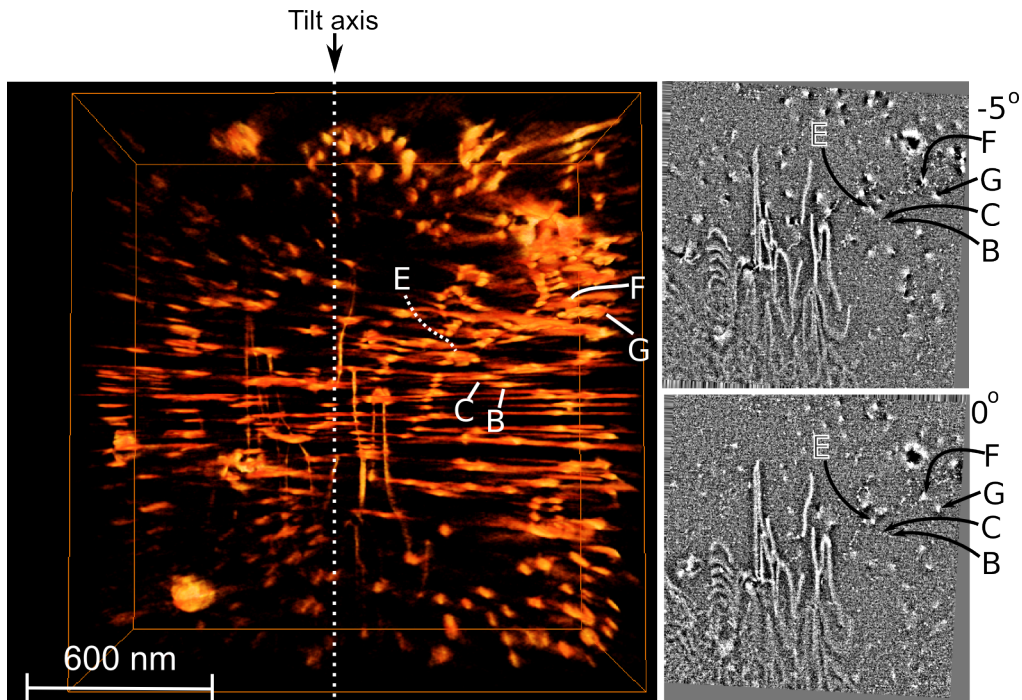


Figure 4.8: The effect of surface relaxation contrast on reconstruction of threading dislocations in GaN. Dislocations such as B and C are reconstructed with a lenticular shape, but do not show significant surface relaxation contrast (they have little or no screw character); this indicates that surface relaxation contrast is not a necessary cause of the lenticular shape. Dislocations such as E, F and G which do show significant surface relaxation contrast in images close to zero tilt such as those shown here from 0° and 5° , show the most streaking in the reconstruction. The surface relaxation is stronger in the sharpened images used for reconstruction (shown here) than in the original images, in which it fades smoothly into the background, similarly to the wide dislocation contrast in Figure 4.7.

An annular dark field detector of inner radius 3.5 mm and outer radius of 10.5 mm was used (same detector as for GaN STEM tilt series), with camera length 200 mm chosen empirically for best dislocation contrast. This angular range of 17.5–52.5 mrad corresponds to 2.7–8.1 $\theta_{B(220)}$ or 3.8–11.4 $\theta_{B(200)}$. A probe of maximum width 4 Å (measured by JSB by taking an image of the probe and calibrating its scale using Si lattice fringes of known orientation) and convergence angle 5 mrad was used. Images were taken every 2° over the tilt range -70° to $+70^\circ$. FEI’s Xplore3DTM software was used to acquire the images; automatic correction of specimen drift was possible, but automatic focusing failed. Image alignment and reconstruction was carried out using FEI’s Inspect3DTM software using SIRT with 30 iterations.

4.3.2 Results

An image from the ADF STEM tilt series is given in Figure 4.9. Image contrast was much more consistent over the specimen tilt range than in WBDF imaging. Automatic acquisition software could thus restore the correct region of interest to the field of view at each tilt angle, though manual focusing was still required. This is a significant improvement in the ease of obtaining a tilt series.

The reconstruction obtained is shown in Figure 4.10. Individual dislocations could be seen on areas of the microcrack away from steps, with the narrowest distinguishable feature in the out-of-plane direction having width of 33 nm \pm 5 nm. There were no moiré fringes visible in the image or the reconstruction, and all dislocations appeared to be present (no extinctions) in the images and reconstruction. The angle of the plane with the foil normal was 52.0°, compared to 54.7° for the angle $(\bar{1}1\bar{1})$ should form with (001). Even though the images had been processed to reduce long-range intensity variations, there was a low intensity extension out of the defect plane around the bright steps in the microcrack.

The dislocation width in the plane could be measured as also 33 nm \pm 5 nm — narrower than could be achieved with the WBDF images due to the problems introduced by the moiré fringes for the WBDF tilt series. The

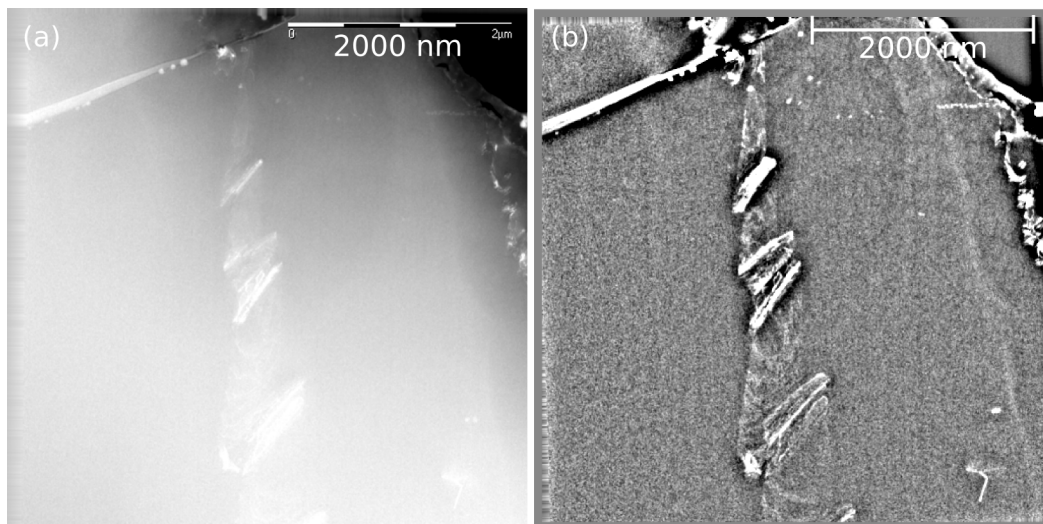


Figure 4.9: ADF-STEM images from Si tilt series, at -4° tilt. (a) Original image; (b) sharpened image, showing dislocations more clearly, especially in the lower portion of the image which formerly had a more intense background level. Oxide precipitates are also visible [104].

distances between steps of the microcrack could also be measured: they are not regular, varying by 150 nm (Figure 4.11).

4.3.3 Discussion

In the case of this extended defect, ADF STEM gave a great improvement over WBDF images for tomography. There were no moiré fringes or thickness contours in the ADF STEM images, so alignment was more accurate. The reconstruction shows all the dislocations from the four WBDF tilt series as shown in Figure 4.12. The dislocations in the WBDF tilt series were reconstructed only in fragments, so a figure of reconstructed dislocation line width for those reconstructions cannot be meaningfully obtained for comparison with this STEM reconstruction. The angular range of the detector in this tilt series corresponds to that in which thermal diffuse scattering becomes strong and elastic scattering becomes weak in Si(100) [105].

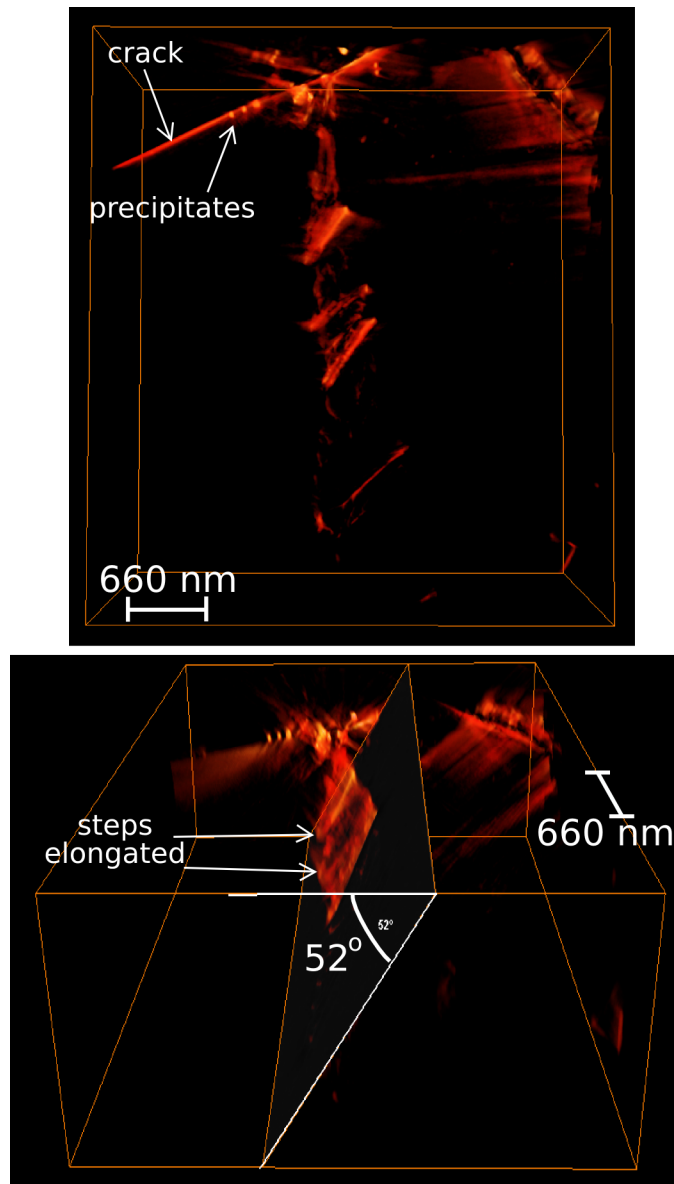


Figure 4.10: Top: plan view of Si STEM reconstruction. Individual dislocations are reconstructed in areas between steps, even where background intensity in the images was high. The microcrack surfaces do not give strong contrast; the positions of sections between steps are indicated only by the dislocations on them. Bottom: The slip plane of the dislocations forms an angle of 52.0° with the foil plane at zero tilt.

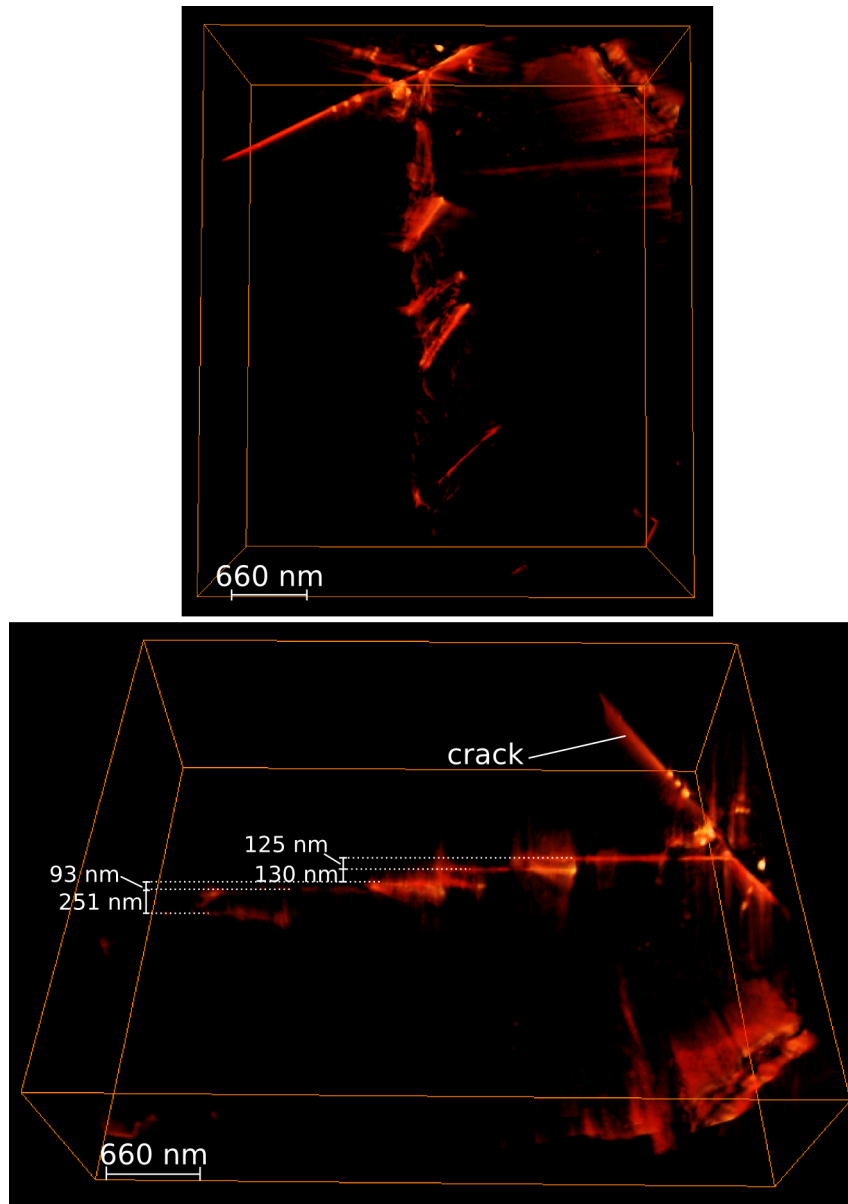


Figure 4.11: Top: plan view showing the dislocations for which widths were measured, both $33 \text{ nm} \pm 5 \text{ nm}$. Bottom: viewed from the side of the dislocation slip plane, showing the spacings between steps. Distances are $\pm 5\%$.

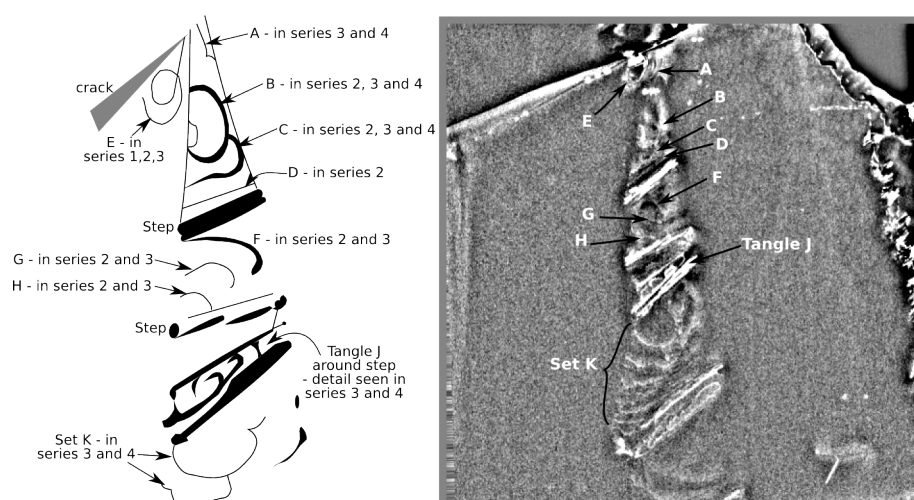


Figure 4.12: Left: schematic showing dislocations seen in the four weak-beam dark-field tilt series of the microcrack in Si. Right: image at 22° from the STEM tilt series of the same region. The area around C and D is unclear in this image but clearer at other images in the STEM tilt series. All four WBDF tilt series and the STEM tilt series are given as movies on the attached DVD.

4.4 ADF STEM tomography of dislocations in TiAl

This reconstruction uses the same TiAl sample as in Section 3.5, but is taken in a region of Al_5Ti_3 superstructure where bundles of four dislocations are found. This reconstruction provides another example in which automated specimen drift correction was possible.

4.4.1 Experiment

The sample of Ti-56%Al alloy, of $\langle 111 \rangle$ foil normal, was mounted in a Fischione dual axis (tilt rotate) holder. A tilt series of images with the tilt axis parallel to $[2\bar{2}0]$ were taken at 200kV in the Tecnai F20 using the Fischione HAADF detector with a camera length of 490 mm, which gives collection angles $14.1 \text{ mrad} < \beta < 70.6 \text{ mrad}$. This is a different detector to that used for previous ADF STEM defect tomography in this chapter; its angular range overlaps with that of the previous detector. This detector

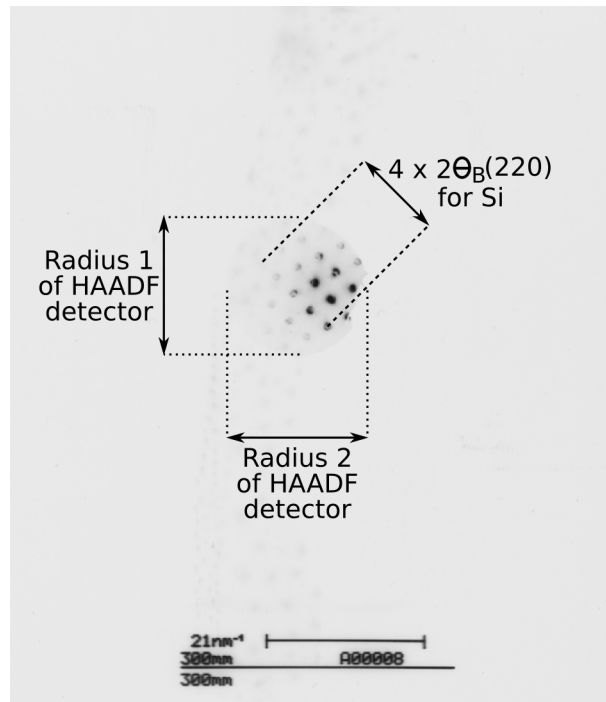


Figure 4.13: Calibration of the angular range of the Fischione HAADF detector on the Tecnai F20. A diffraction pattern was formed from a test sample of (220) Si and the HAADF detector inserted, blocking the outer part of the diffraction pattern and creating a shadow in the image (in this negative, the diffraction discs appear black and the shadow is white). The inner angle of the HAADF detector can then be calculated by measuring the inner radius of the shadow and calibrating it against the known Bragg angle $2\theta_B$ for the (220) reflections.

was used because it was possible to first calibrate the collection angles for each camera length, by superimposing the shadow of the detector onto the diffraction pattern from a calibration sample of single crystal Si (Figure 4.13).

Images in the TiAl tilt series were taken every 2.5° between $\pm 60^\circ$, as a compromise between time constraints and taking the maximum number of images possible, using FEI's Explore3DTM tomography software with automatic specimen drift correction. Data collection was done by JSB, Y.L. Chiu (owner of the sample) and the author.

After the first reconstruction attempt, images were sharpened to eliminate a background ramp of intensity under the clear dislocation images, which in the first attempt gave a background ramp to the reconstruction that obscured

the dislocations. Inspect3DTM was used for alignment and reconstruction by SIRT (30 iterations).

4.4.2 Results

Unlike previous ADF STEM experiments, defect contrast varies considerably throughout the tilt series. At some angles the dislocations appear significantly more broad and diffuse than others; focusing was done to the best of operator ability for every image, so it may be that the images are genuinely broad and diffuse, or focusing may have still been suboptimal. The dislocations and background are also quite grainy; this may be due to surface roughness from sample preparation, or surface contamination. Surface roughness affects low-angle ADF STEM strongly if it is $\approx 10\%$ of the sample thickness, depending on beam strength (JSB, pers. comm.); in Figure 4.15, scratch-like features are seen parallel to the vertical axis. Surface contamination may be important: plasma cleaning of the sample was mistakenly omitted, whereas the sample was plasma cleaned before taking the WBDF tilt series which did not display this problem. The Si sample, however, was not plasma cleaned for either the WBDF or STEM tilt series, because the potential for surface damage during plasma cleaning was judged to be too great, and this type of artifact was not seen. Either or both of these effects may be responsible.

In the centre of the reconstruction there is a band of four dislocations, indicating that this part of the region of interest has the Al_5Ti_3 superstructure. At some angles, only the four-band is seen clearly; at some angles, additional dislocations are visible (Figure 4.14), presumably because they have different Burgers vectors. Extinction like this has not been observed in the other ADF STEM tilt series.

In terms of the $L1_0$ structure, possible Burgers vectors are $\frac{1}{2}\langle 110 \rangle$ (ordinary dislocations) and $\langle 101 \rangle$ (superdislocations with Burgers vector spanning two Ti layers), both of which congregate in fours in the Al_5Ti_3 superstructure, as its unit cell is four times the size of that in $L1_0$. Four-bands of ordinary dislocations have uniform spacings, whereas one of the

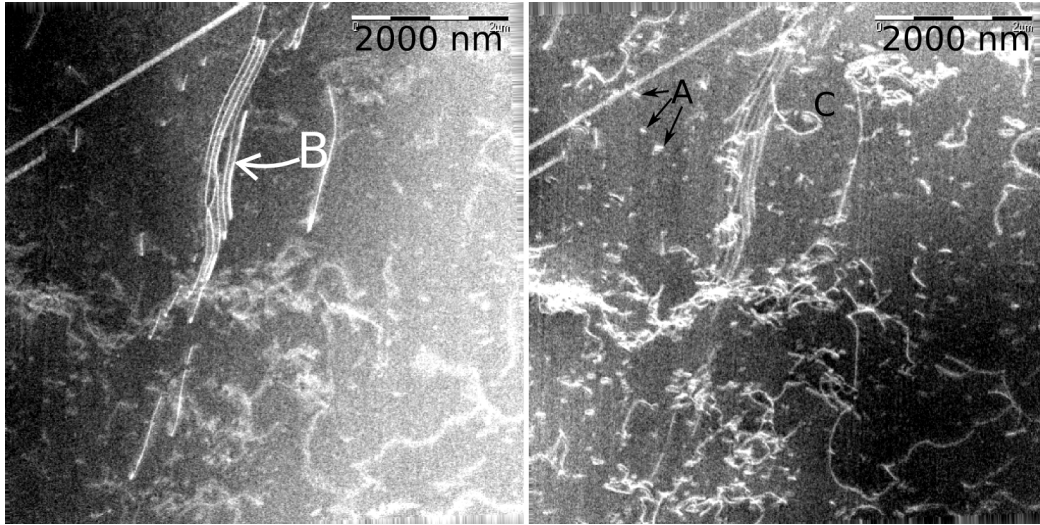


Figure 4.14: Images from STEM tilt series of TiAl, showing partial extinction. Left: -20° tilt; a four-band of defects (labelled B) is clearly visible, some others are out of contrast and others faint and diffuse. Right: -15° tilt; band B now appears fainter, others are now in sharp contrast, notably a spiral at C. Band B is absent in most of the tilt series, while the others are present in almost all images. Small points can be seen, such as those at A; these are probably prismatic loops from rows left where two screw dislocations of opposite sign have interacted [90].

outer spacings in a four-band of superdislocations is expected to be greater and more variable along the length of the band than the other two, as this kind of antiphase boundary has lower energy than the others [90]. Band B in Figure 4.14 appears to have one dislocation that wanders away from the other three, indicating that this may be a band of $\mathbf{b} = \langle 101 \rangle$ superdislocations.

In some images the dislocation lines appear double, as shown in Figure 4.15. The scale bar on this image is rather approximate, but the spacing between the two lines at a double line is comparable to the partial spacing within the four-band, which in studies of this material has been reported as typically 25 nm [90]. It has been reported that outside the Al_5Ti_3 superstructure, superdislocations of Burgers vector $\langle 101 \rangle$ can decompose into two dislocations with spacing of this order according to $\langle 101 \rangle \rightarrow \frac{1}{2}\langle 110 \rangle + \frac{1}{2}\langle 112 \rangle$ [90]; this is probably what is observed here, and not a false double line produced at a strong diffraction condition.

These features are reproduced in the reconstruction with varying intensity

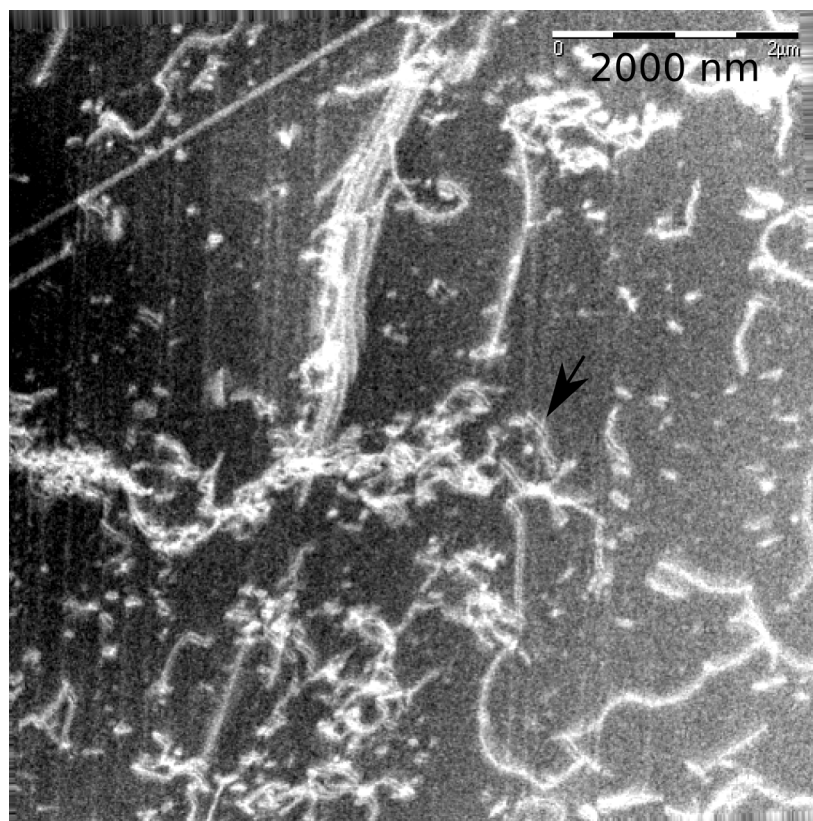


Figure 4.15: Image from STEM tilt series of TiAl, tilt angle -17.5° , between the two images in Figure 4.14. Double dislocation images are visible, for example at the arrow and around it; these are probably dissociated superdislocations.

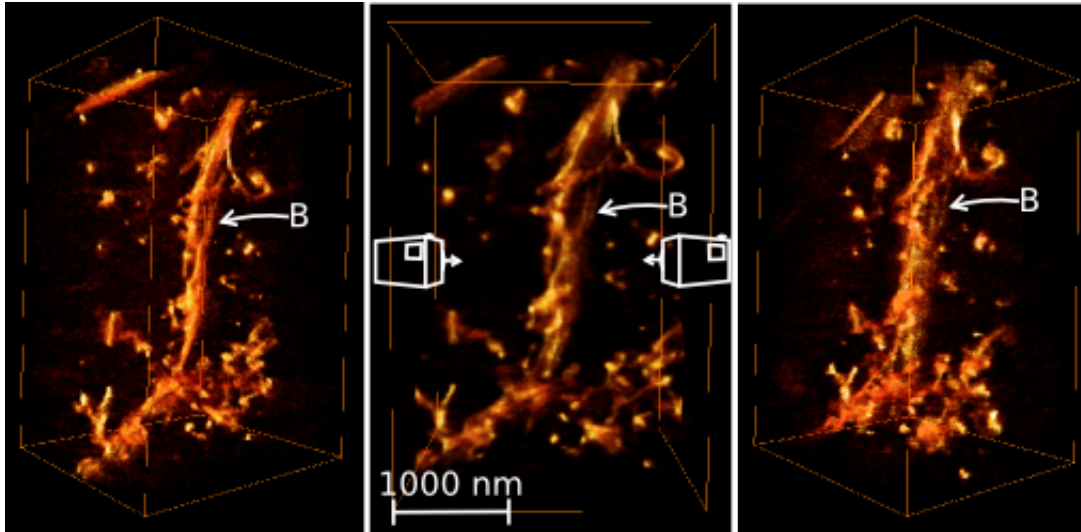


Figure 4.16: Reconstruction from ADF STEM TiAl tilt series. Centre: plan view with camera positions showing viewing direction of left and right images. Band B is reconstructed as a faint translucent feature.

(Figure 4.16). The dislocations that are nearly always visible (such as C in Figure 4.14) are reproduced as broad lines, compromising between the images with fine detail and the fuzzy images. Four-band B, visible in fewer images, is reproduced as a faint plane; dislocations that overlap with band B in the tilt series images are reproduced slightly less accurately, but are not absent. Unfortunately the grainy quality of the images is carried through to the reconstruction.

The spiral C and band B overlap in the images, which seems paradoxical — the Al_5Ti_3 superstructure should only allow dislocations in fours, and generally they are close to straight, and spiral C (and the dislocation leading into it) are single and curved, as should appear only in the $L1_0$ matrix. In the reconstruction, however, it can be seen that band B inclines down into the sample and the dislocation leading into spiral C bypasses it parallel to this incline (Figure 4.17). It is probable that the boundary between Al_5Ti_3 superstructure and $L1_0$ matrix is between B and C.

In cross section, the dislocations in the $L1_0$ matrix have the same structure as seen in the GaN STEM reconstruction: an intense core and a diffuse

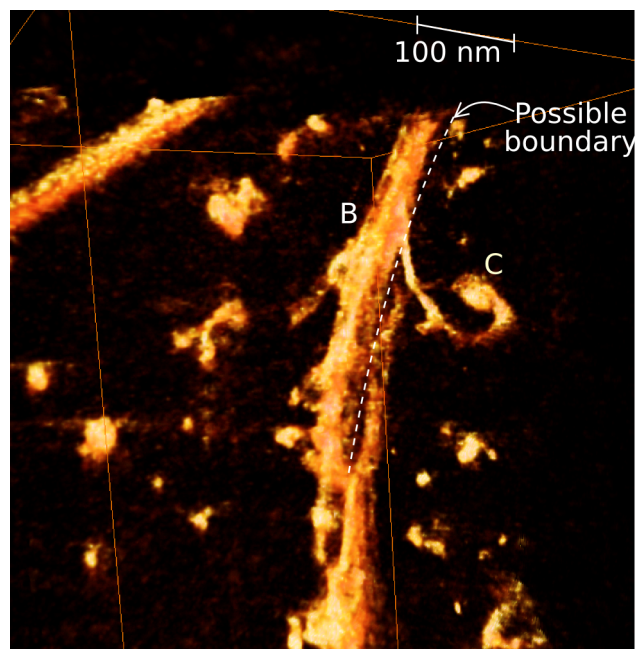


Figure 4.17: Closeup of band B and spiral C, at around 45° from zero tilt, with B edge on. As band B is inclined down into the foil, the dislocation leading into spiral C skirts the plane of this incline. The boundary between Al_5Ti_3 superstructure and $L1_0$ matrix is likely to be somewhere between B (showing four-band behaviour) and C (showing behaviour atypical of dislocations in the Al_5Ti_3 superstructure).

surrounding intensity, as shown in Figure 4.18 for the straight portion leading into spiral C. This is elongated by a factor 1.5 ± 0.4 (the uncertainty is large because the measured lengths are only 4-6 pixels), which matches the missing wedge factor of 1.55 for the tilt range used and the elongations of 1.5-1.9 for the weak-beam dark-field tilt reconstruction of dislocations in another L1₀ region of the same sample. The dislocations in Al_5Ti_3 are too close together to analyse their individual cross sections; in Figure 4.19, the cross section of the four-band B is seen. A number of intense parts can be seen, but their separation is close to the limit of resolution in the reconstruction.

4.4.3 Discussion

This reconstruction has little advantage over the WBDF reconstruction from the same material; the contrast is more inconsistent and the dislocations are harder to resolve, though this is partly because the area chosen was more dense in dislocations. An approximate calculation (using the microscope scale bar on the diffraction pattern and a correctly calibrated β_{in} and β_{out} for the HAADF detector) gives the angular range of the detector as $1.5\theta_B - 7.7\theta_B$ for $\mathbf{g} = 2\bar{2}0$. This comes closer to the bright field beam than the previous two ADF STEM tilt series, which may explain why this tilt series showed extinction, a signature feature of dark-field defect contrast, where the other two tilt series did not.

In terms of material properties, this technique has potential to reveal a great deal. The original goal of tomography was to determine whether the dislocations in a four-band can cross-slip onto different planes; however, the individual dislocations in band B are not reconstructed accurately, partly because of the effect of sample contamination or roughness observed in the images which is carried through as a grainy texture in the reconstruction. If the contamination/roughness could be removed or avoided, and the experiment repeated at a higher magnification, tomography could still discover this.

The imaging conditions for the three ADF STEM data sets are summarised in Table 4.1. With reference to the plot of angular distribution for

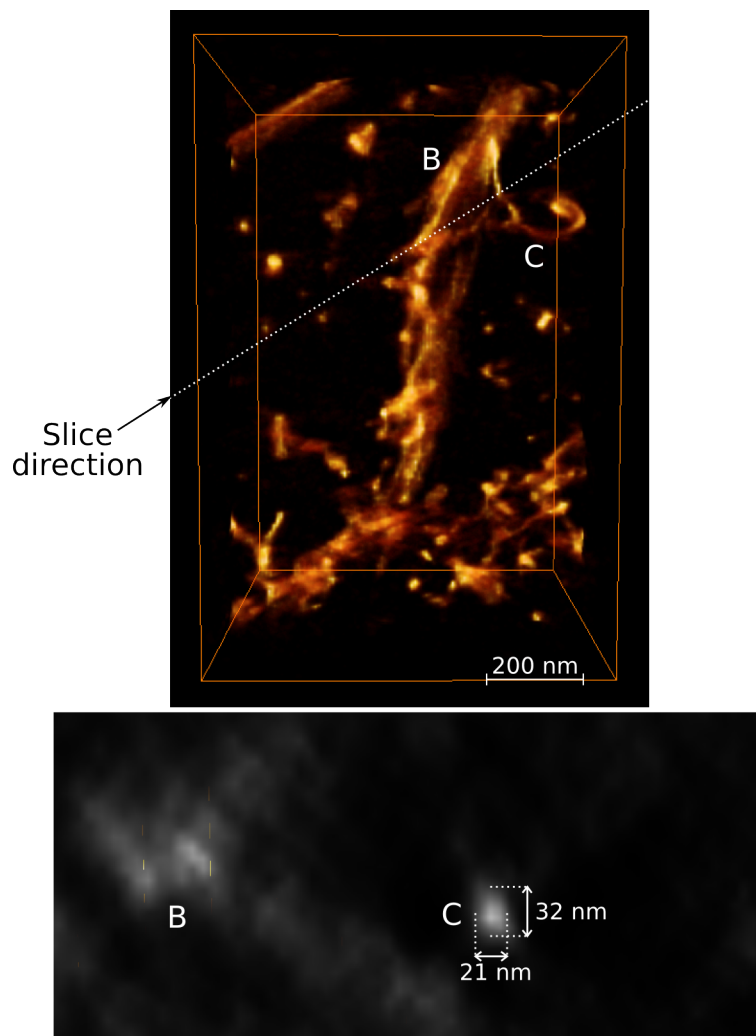


Figure 4.18: Section of the dislocation approaching spiral C in the $L1_0$ matrix. The out-of-plane elongation factor is 1.5, which matches the expected elongation due to the missing wedge. Lengths in this image have uncertainty of ± 6 nm.

| Material | Detector | Camera length | Angular range | |
|----------|----------|--------------------|---------------|------------------|
| | | | mrad | θ_B |
| GaN | ADF | 100mm | 34.0-105.0 | 4.4-13.1 |
| Si | ADF | 200mm | 17.5-52.5 | 2.7-8.1 |
| TiAl | HAADF | 490mm (calibrated) | 14.1-70.6 | 1.5-7.7 (approx) |

Table 4.1: Table of collection angles for STEM tilt series in this chapter

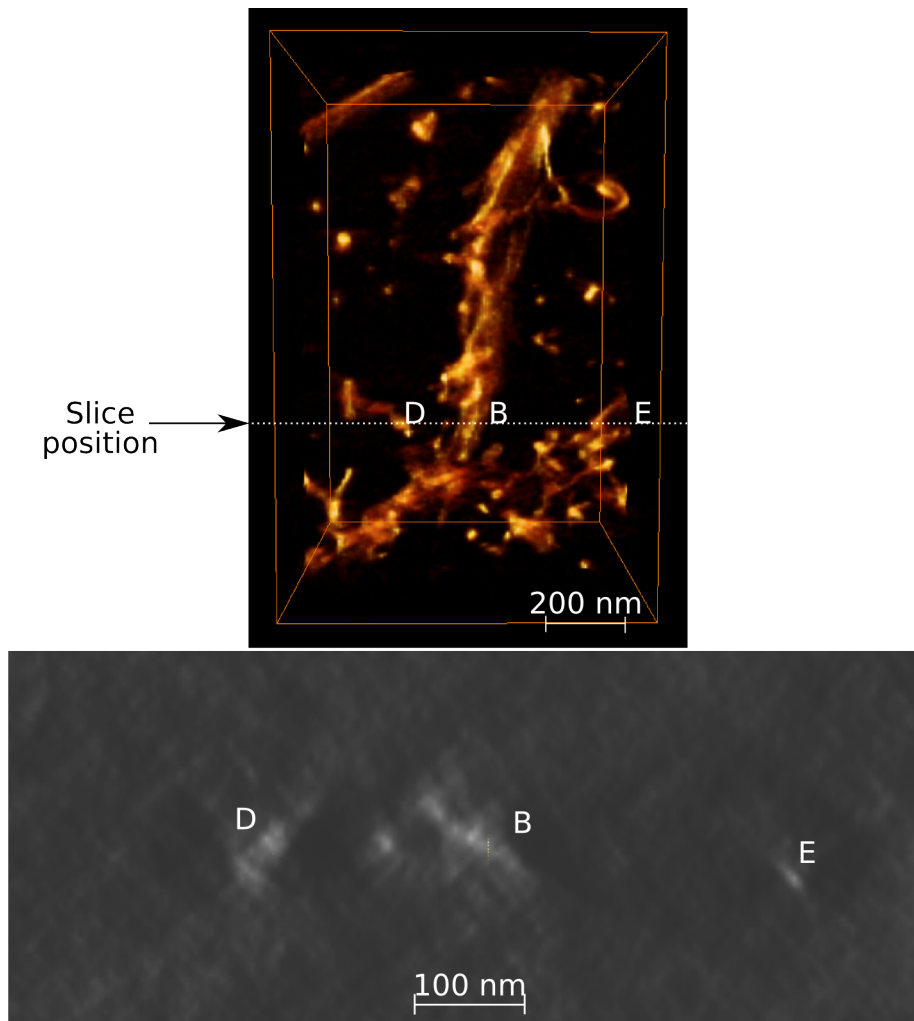


Figure 4.19: Section of the four-band B in the Al_5Ti_3 superstructure. Bright points can be seen in the cross section, but they are not large or distinct enough to be sure that they are the four dislocations sought.

Bragg scattered intensity and TDS intensity for these materials (Figure 4.2), the crossover for TDS being dominant falls just above the inner detector angle β_{in} for GaN, midway between β_{in} and β_{out} for Si but beyond the outer detector angle for TiAl. That is, the intensity collected should be dominated by TDS for GaN, by Bragg scattering for TiAl and shared between Bragg and TDS for Si. Partial extinction (i.e. becoming faint but not absent) was observed in the TiAl ADF STEM tilt series but not the others; an interesting feature of this material is that the Al_5Ti_3 superstructure contributes extra diffraction spots halfway between the spots of the $L1_0$ matrix [90], which is where the ADF detector inner angle should fall if the diffraction pattern is centrally aligned. The band of four dislocations in the Al_5Ti_3 superstructure is the part that experiences partial extinction at the majority of angles; it could be that when the innermost superstructure spots fall on the annular detector during tilt series collection, the four-band becomes bright, but when the innermost superstructure spots miss the annular detector (at most tilt angles), they are less bright. The effect of this should be tested experimentally.

Interestingly, despite the intensity being in theory predominantly TDS for the GaN tilt series, at several images in the tilt series the threading dislocation images are fringed. This has been observed in zone axis ADF dislocation images observed from higher collection angles [95] ($\beta_{in} = 105$ mrad there); the explanation was that Bloch wave transitions occurring at the dislocation could be seen second-hand, as some Bloch states have a higher probability of TDS than others due to their positions with respect to atom strings, and the dislocation line at depths where those ‘s-type’ states are highly occupied gives a brighter intensity than at depths where they are empty. This is explored in more detail in Chapter 5.

4.5 Conclusions and further work

The experiments in this chapter show that ADF STEM is a technique that holds potential for defect tomography, especially when there are fringed features such as microcracks or stacking faults present that impair

tomography from WBDF images. For the TiAl tilt series in which scattered intensity was taken from a smaller detector inner angle, closer to the bright field spot, there is extinction of the four-band dislocations, which results in low reconstructed intensity for the affected dislocations. The nature of ADF STEM contrast depends on detector collection angle, but the literature mainly concentrates on high collection angles. The next chapter, part literature review and part development, will address this and set down directions for further work that is needed to understand this contrast and optimise ADF STEM defect tomography.

Chapter 5

Theoretical considerations for ADF STEM tomography of defects

5.1 Introduction

In order to optimise ADF STEM tomography, we must understand which kinds of scattering contribute to the image and the factors that affect it as the sample is tilted. This is a greater challenge than optimising WBDF tomography; STEM is a relatively new technique that involves a number of complicated mechanisms working simultaneously and interacting, and there are no widespread programs known to the author for simulating ADF STEM defect images at arbitrary orientations and collection angles. The literature on ADF STEM contrast mainly discusses high-resolution lattice imaging under zone axis diffraction conditions. Those researchers who have tilted the sample significantly away from zone axis orientation, have done it to use mass-thickness (Rutherford) contrast for HAADF STEM tomography (e.g. [97]) and coherent contrast mechanisms that contribute to defect contrast in ADF STEM have been irrelevant except as a source of unwanted artifacts. Further, most ADF STEM is performed at high detector inner collection angle (>40 mrad, beyond the edge of the zero-order Laue

zone [106]) for which thermal diffuse scattering and Rutherford scattering are the most important processes (Figure 4.2); in choosing the camera length empirically, we have used smaller collection angles that include some of the zero order Laue zone Bragg spots. This chapter surveys the limits of previous work, and advances the borders a little.

5.2 Contributions to ADF-STEM defect images

Defects have been proposed to contribute to ADF-STEM images through more than one scattering process; in this section they will be summarised and the significance of the defect's effect on each process will be assessed.

5.2.1 Differences in Bragg scattering

Elastic Bragg scattering contributes to low-angle ADF STEM defect images in the same general manner as conventional DF TEM imaging, described in Section 1.2. A more convergent probe in conventional DF imaging appears to dampen or even out the characteristic oscillations of a dark-field dislocation image [107]. In that study, dark-field images from a range of angles corresponding to the convergence profile of the beam were incoherently added to simulate the effect of convergence, which reproduced the effect in experimental images. With a high convergence angle (6 mrad in the experiments presented in Chapter 4; convergence angles of up to 10 mrad were used in [107]) the defect images in dark-field discs falling on the ADF detector should also be less fragmented, as is found for most ADF-STEM images in these experiments.

The shape of the annular detector itself also filters out contrast from some Bloch states, so that only states concentrated closely around the atoms are seen strongly [108]. This gives slight differences in the details of contrast from a DF TEM image in which effects from all excited Bloch states are included [95]; this effect is most severe for inner detector angles larger than those used in these studies, i.e. in HAADF [109].

If Bragg scattering is the main contribution to the ADF STEM dislocation image, and the Bloch-state selecting effect of the annular detector is not too significant for the small angles we are using, the contrast can be simulated by incoherently adding all relevant dark-field images under the correct diffraction conditions. An initial attempt at this was carried out using CUFOUR; unfortunately this could not be done for GaN, for which we have obtained good clear ADF STEM images of single dislocations, because a relevant part of the program does not work for hexagonal crystals. A calculation for Al at $[214]$ zone axis orientation (containing only six significantly excited diffraction spots, which simplifies the calculation) produced Figure 5.1. The dislocation runs along $[\bar{1}12]$ with Burgers vector $\frac{1}{2}[110]$.

The two most apparent features in Figure 5.1 are that there are lines of contrast either side of the core, and that the whole bright region is very narrow, around 20 nm. Some ADF STEM dislocation images in the tilt series presented here are this narrow. The double line is not present in the Si or GaN tilt series but is recognisable from the TiAl ADF STEM tilt series in which some images showed double lines; however, dislocations in this material are known to dissociate with a partial spacing of around 25 nm.

A limiting factor in this calculation is that convergence was not included. The effect of convergence is to blur the thickness oscillations along the length of the dislocation image, giving a more continuous line, though not completely devoid of intensity oscillation [107]. It is possible to incorporate convergence under a systematic row diffraction condition using CUFOUR, but further adaptation is needed to apply it in this zone axis condition.

A first hypothesis might be that the ADF STEM dislocation image may be dominated by an incoherent sum of dark-field images if the detector angle includes the innermost Bragg reflections, but other scattering mechanisms have a significant contribution if the innermost Bragg reflections are omitted, making the image wider and more diffuse. More experiments are needed to verify this; most obviously, obtaining and comparing sets of simulations and images that are of the same material and orientation, and incorporating convergence.

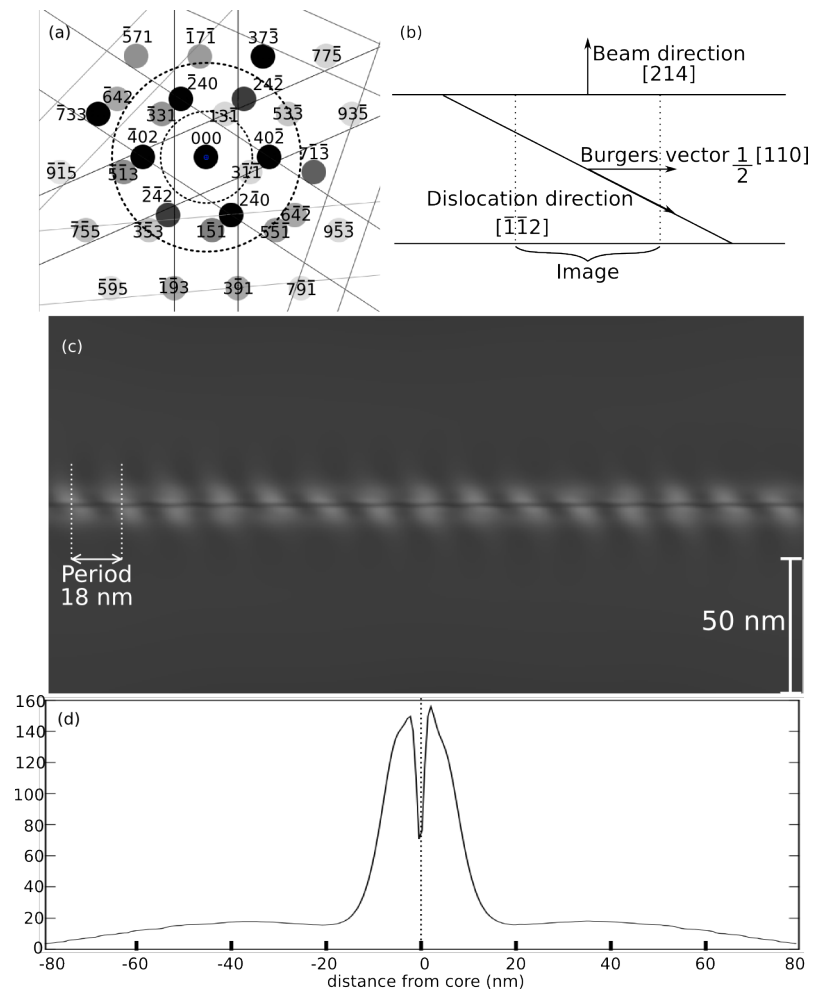


Figure 5.1: Image formed from incoherently adding all (420 type) dark-field images at [214] zone axis orientation of Al, to approximate the Bragg contribution to STEM image if the Bloch-state selecting effect of the annular detector is not strong at this small detector angle. (a) CBED pattern for this orientation and thickness, with angular collection range marked by the dotted circles. Only the six strongest reflections were included for simplicity of calculation. (b) Diagram showing the geometry of the crystal. (c) Multibeam image; the period of 18nm is taken over all fifteen oscillations. Compare with the results of a conventional dynamical dark-field defect image simulation, Figure 3.4. (d) Average image profile; dotted line marks the core position.

5.2.2 Thermal diffuse scattering

Physically, thermal diffuse scattering (TDS) is the result of scattering by atoms that are thermally displaced from their equilibrium positions, redirecting intensity from Bragg scattering to higher scattering angles [110]. Electrons lose a very small amount of energy when they are scattered to high angles by TDS; it is inelastic, but if the resulting energy distribution is not important it can be approximated as an elastic process [94]. TDS is conventionally accounted for in the dynamical theory as ‘anomalous absorption’, by making the crystal potential complex; adopting a model for TDS gives a form for the complex part of the potential $V \rightarrow V + iV'$ [111].

TDS attenuates the Bragg scattered intensity by the Debye-Waller factor, $\exp(-2M_s)$ where $s = \sin\theta/\lambda \approx \theta/\lambda$ for high energies [112]. Overall envelopes for the resulting distribution of Bragg and TDS intensities scattered from the incident beam are described by Equations 5.1 [98], assuming no intensity is lost to other processes. These expressions were used to plot Figure 4.2; Bragg scattering is seen only at Bragg peaks, but this distribution underlies the intensity at those peaks.

$$\begin{aligned}dI_{Bragg} &= 2\pi s f_e^2 \exp(-2M_s) ds \\dI_{TDS} &= 2\pi s f_e^2 [1 - \exp(-2M_s)] ds\end{aligned}\tag{5.1}$$

In diffraction patterns, TDS is seen as diffuse patches around the Bragg peaks, streaked as a result of phonon scattering, but distributed toward higher scattering angles than Bragg scattering [105]. At still higher scattering angles, contrast is dominated by TDS, now referred to as Rutherford-like Z contrast [113], often also called mass-thickness contrast [32, Chapter 22]. Z-contrast is not affected by defects unless the defects are decorated with impurity atoms or precipitates. For HAADF-STEM electron tomography using Z-contrast, the behaviour of TDS/Rutherford contrast is often approximated to a (σZ^2) dependence in the high-angle regime (σ is scattering cross section) since this simple dependence allows optimal

tomography when elemental contrast is important [97]. When an image is required that contains only these processes, for example a Z-contrast image with no artifacts from diffraction effects, a high angle annular detector is used [114], [106] with inner detector angle β_{in} between 30-50 mrad, depending on material [110]. Values of $\frac{\sin\theta}{\lambda}$ for the inner and outer detector angles in the experiments presented here are given in Table 5.1, along with the angles at which the higher intensity scattering mechanism switches from Bragg scattering to TDS according to Equations 5.1 in Figure 4.2.

| Material | Angular range (mrad) | $s = \frac{\sin\theta}{\lambda} \text{ \AA}^{-1}$ | Bragg-TDS changeover (mrad) |
|----------|----------------------|---|-----------------------------|
| GaN | 34.0-105.0 | 1.35-4.18 | 38.2 |
| Si | 17.5-52.5 | 0.70-2.09 | 39.0 |
| TiAl | 14.1-70.6 | 0.56-2.81 | 53.6 |

Table 5.1: Values of $s = \frac{\sin\theta}{\lambda}$ for STEM tilt series in this thesis. Bragg scattering dominates for only 5% of the collection range for the GaN tilt series, but 58% of the Si collection range and 70% of the TiAl collection range; however, the first set of DF Bragg reflections were missed by the detector for Si but collected for TiAl (Table 4.1).

The Einstein model

The simplest physical model for TDS is the Einstein model, in which there is no correlation between thermal vibrations of neighbouring atoms [115], [116]. A random walk model is used for the thermal displacement and each atom is assigned a mean squared thermal displacement. The Debye-Waller factor derived from the Einstein model is given in Equation 5.2 [111], where $\langle u^2 \rangle$ is mean squared thermal displacement.

$$\exp \left[-\langle u^2 \rangle (2\pi s)^2 \right] \quad (5.2)$$

This uncorrelated model of TDS can be incorporated into a multislice simulation by displacing the atoms by random amounts within a Gaussian distribution of displacements and averaging over many images calculated in

this way [114], [116]; this hinges on the *frozen phonon* approximation: the transit time of an electron through the specimen is much smaller than the period of thermal vibration, so the atoms act as stationary during the time in which the electron encounters them [116]. In a Bloch wave simulation, TDS is incorporated by using a complex potential to model the anomalous absorption, but this discards the information carried by the ‘absorbed’ intensity.

The phonon model

The Einstein model is a relatively simple approximation; in reality, thermal vibrations are not actually uncorrelated. Normal modes of vibration known as **phonons** exist in the crystal. The atom displacement at a site is the sum of the displacements imposed on it from each phonon. The wavelengths of normal modes are quantised, so phonons can be seen as a wave or a particle. TDS can therefore be seen as electrons being scattered by phonons; this allows for the possibility of:

- Multiphonon scattering, when an electron is scattered by more than one phonon at the same time,
- Multiple phonon scattering, when an electron is scattered by more than one phonon, one after another.

When the angular distribution of TDS is calculated based on the phonon scattering model, it transpires that multiphonon and multiple phonon scattering are most important at larger angles. If an annular detector that subtends a wide angle is used (HAADF), it is more important to use a phonon model that takes into account these events in calculating the total TDS intensity. At these high scattering angles, multiple and multi-phonon scattering tends to Einstein model behaviour; at lower scattering angles (less than ~ 50 mrad), single phonon scattering dominates [111].

The correlation of atom vibrations under long wavelength phonons also means that even if scattering to an annular detector is mainly TDS, it is not necessarily incoherent. It is estimated that the vibrations of atoms have a correlation length of 3-5 atoms in the beam direction [117].

The effect of defects

Since the intensity of TDS depends on the mean-squared vibration amplitude $\langle u^2 \rangle$, a defect whose strain field affects the atomic environment should change the TDS intensity from that region. To estimate this effect, the dilatation around an edge dislocation was calculated from the simplest isotropic elasticity model for the dislocation's strain field [1] and the vibration amplitude scaled by a third of this. This was done because volume of vibration scales as $V \propto u^3$; so $\frac{dV}{du} \propto 3u^2$ and $\frac{dV}{V} \propto \frac{3u^2 du}{u^3} = \frac{3du}{u}$ so $\frac{\Delta u}{u} \propto \frac{1}{3} \frac{\Delta V}{V}$. This is an approximation, as thermal vibrations do not act this classically on the scale of single atoms. This changed vibration amplitude was put into the Debye-Waller factor from the Einstein model, Equation 5.2, using $\sin \theta / \lambda$ for 30 mrad, an angle in the middle of typical ADF detector range for these tilt series. The contribution to TDS intensity was estimated using Equation 5.1. A core region of diameter equal to the Burgers vector was given thermal vibration amplitude equal to twice $\langle u^2 \rangle$, to avoid calculation failure due to the asymptote that occurs when linear elasticity fails in the core region.

The result of this simple calculation (Figure 5.2) show that the additional TDS intensity generated around the dislocation is imperceptibly small, 1×10^{-11} of the background TDS intensity, whereas the threshold for visible contrast is of the order 0.05 [32]. Figure 5.2 shows the change in TDS intensity ΔI_{TDS} because a plot of absolute intensity showed no observable change to confirm the calculation had been done. Although this calculation includes many approximations, the extreme result shows that additional TDS from site volume change is probably not a significant contributor to defect contrast in STEM and can be safely ignored.

Defects can also interact with phonon-scattered electrons, another way to affect the outcome of TDS, and inelastic defect images can be formed by placing the objective aperture in the diffraction plane in the TDS region between Bragg spots and using conventional TEM to produce an image selecting the relevant energy [118]. This is comparable to the production of Kikuchi lines by a perfect crystal. The results of such an interaction between TDS and defects should also appear in the diffuse-scattered intensity falling

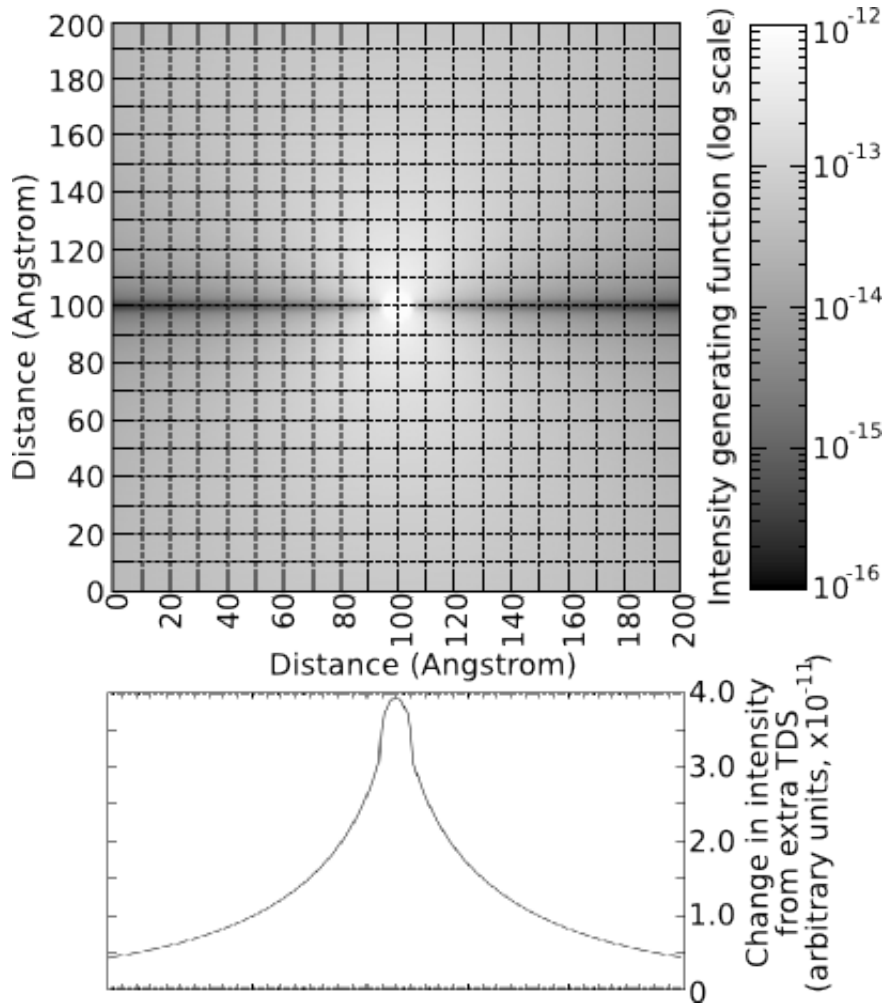


Figure 5.2: Top: cross section of Al edge dislocation showing TDS intensity generating power, as described in text. These changes are unobservable compared to background TDS intensity of 0.81 in the same units as displayed. Bottom: downward projection of intensity generating function, giving an approximate image profile, still unobservably small. The central $\approx 5\text{\AA}$ circle is an artificially imposed core region, as linear elasticity fails at dislocation cores.

on the ADF STEM detector in the diffraction plane. The effect of this is to redistribute intensity within the large angular range encompassed by the ADF detector, so it can be ignored for a preliminary analysis [109, p178].

5.2.3 Huang scattering

Huang scattering is similar to thermal diffuse scattering; in the frozen phonon approximation, a static displacement is equivalent to a displacement occurring as part of a thermal vibration, except that it is time-independent: the displacement is the same for each electron that passes through. Like TDS, Huang scattering removes intensity from Bragg scattering [117, p212]. If Huang scattering is the sole or major cause of ADF STEM dislocation contrast, as suggested by Wang [113] the maximum defect image intensity should occur where the maximum displacement occurs, i.e. at the dislocation core — unlike weak-beam dark-field images where the line is to one side of the actual core position [110], [113]. Cowley and Huang suggest that Huang scattering should have the same dependence on scattering angle as TDS [58]; however, the displacements involved are perfectly correlated between atoms, so its effects cannot be treated as a little extra TDS in the Einstein model and subsumed into the Debye-Waller factor in the same manner as Figure 5.2.

Initial assessment of Huang scattering

For Huang scattering to exceed background TDS in intensity and be observable, the magnitude of the atomic displacement from the defect strain field needs to be greater than the mean thermal vibration amplitude. For a threading edge dislocation in GaN, the maximum displacement arising from the long-range stress field (using the simple isotropic elasticity form [1]) is of the order 1-2 Å while the mean thermal vibration for Ga is 0.07 Å [119]. At the dislocation core there is a region without crystal structure of ~ 10 Å diameter [120] which should count as a narrow region of large displacement. Overall, the dislocation should be visible by its Huang scattering.

The dislocation's Huang scattering cross section σ_{disn} is then given by $\sigma_{disn} = 2r_o$ where displacement field at r_o , $R(r_o) = 2\sqrt{\langle u^2 \rangle}$, for mean thermal

vibration amplitude $\sqrt{\langle u^2 \rangle}$ [113]. For the direction perpendicular to the ‘additional atom plane’ for the same edge dislocation in GaN, this gives a Huang scattering image extending 9.1Å from the core, using the simple isotropic elasticity expression for the displacement field [1], which is valid for displacements in and close to the basal plane [121]. This gives a Huang scattered image width of $\approx 20\text{Å}$. This is narrower than that found in practice which is more of the order 10-20 nm, from the full-width half-maximum of the images in this work. This is a simple calculation; more complicated events must occur to give a wider image. In particular the image width may be broadened by what happens to the electrons after Huang scattering, such as thermal rescattering during propagation to the exit surface.

Theories of Huang scattering

In Wang’s STEM multislice theory [94], Huang scattering is included in the Bragg scattering terms, because it is also time-independent. The defect displacement field is then included in multislice simulations by modifying the atom positions in the slices, and has been done for point defects. However, the volume of crystal needed to contain a dislocation is larger than that used for normal multislice simulations [122] and setting up a multislice simulation of this size is beyond the scope of this project.

Cowley demonstrates a kinematical model [123] and, later, Wang demonstrates a two-beam Bloch wave model [117, Chapter 7] for Huang scattering intensity from the distortion around a distribution of point defects by calculating the total scattering and subtracting away the Bragg scattering. In order to arrive at something practical to analyse, these models rely on substantial simplification by approximations about bulk behaviour that are not appropriate to the case of the displacement around a dislocation or stacking fault; a different approach would be needed.

5.3 Bloch wave theories for ADF STEM dislocation contrast

There are a number of Bloch wave theories for ADF STEM contrast, all of them partially relevant to dislocation contrast. These theories will be explored briefly in this section.

Bragg and Huang scattering, both elastic and time-independent, can be combined into the same theory [124]. Nellist, Pennycook, Jesson and others give a Bloch wave theory of ADF STEM on elastic scattering for perfect crystals [108]. They cautioned, however, that this is not the whole story; TDS damps the Bloch wave oscillations [109]. Different states scatter to TDS differently, the basis of anomalous absorption. Perovic, Howie and Rossouw explained the detailed contrast of dislocations in HAADF-STEM by redistribution between Bloch states at the defect and subsequent differential scattering to TDS [95]; in this indirect way, TDS is important for defect contrast. Wang [117] developed a Bloch wave theory that includes TDS as well as Huang and Bragg scattering, but so far this complicated theory has been used only on perfect crystals and the simple strain fields of substitutional atoms. Extension to dislocations is work yet to be done.

5.3.1 Incorporating the convergent beam

In weak beam images, high convergence smears out or damps the depth oscillations of dislocation images [107] — convergence is modelled in that paper by incoherently summing images with incident beam orientations within the range that is covered by the convergence angle, up to 10 mrad. This is similar to the method used here to simulate WBDF tilt series, but with a different system for changing the incident beam direction.

Nellist *et. al.* incorporate differently the relatively large convergence angles used in STEM, 6 mrad for the data presented in this thesis. A incident cone of partial plane waves, with transverse wavevector components \mathbf{K}_i and complex amplitudes $A(\mathbf{K}_i)$, is used as the boundary condition at the entrance surface when finding the Bloch wave amplitudes [108]. This introduces an

additional integral over \mathbf{K}_i . The wavefunction from this, dependent on lateral position \mathbf{R} and depth z , for probe position \mathbf{R}_o is given by Equation 5.3 [108]: $\Phi_o^{(j)}(\mathbf{K}_i)$ are Bloch wave amplitudes dependent on the incident wave vector; $k_z^j(\mathbf{K}_i)$ is the wavevector of Bloch wave j in the beam direction.

$$\Psi(\mathbf{R}, z, \mathbf{R}_o) = \int \sum_j \sum_g A(\mathbf{K}_i) \Phi_o^{(j)*}(\mathbf{K}_i) \Phi_o^{(j)}(\mathbf{K}_i) \exp[-2\pi i ((\mathbf{K}_i + \mathbf{g}) \cdot \mathbf{R} - \mathbf{K}_i \cdot \mathbf{R}_o + k_z^j(\mathbf{K}_i)z)] d\mathbf{K}_i \quad (5.3)$$

The transverse momentum from the convergent probe elements is transferred to the wavefunction inside the crystal, which changes shape as it propagates through the crystal and as the beam rasters over the surface. The exit wave for each point is then Fourier transformed into a CBED pattern of overlapping discs, which is integrated over a detector function and squared to give the ADF-STEM intensity at each point.

Calculations of high-resolution HAADF image intensities for a perfect crystal from this theory showed the images were mostly a map of s-type Bloch states — other Bloch states did not contribute significantly to the image. This turned out to be due to the annular detector; it acts as a high pass filter to remove contributions from interference between states that are not sharply peaked, and the main contribution is from s states that peak sharply over atom strings [125]. Events occurring in the atom columns are not entirely incoherent perpendicular to the beam, but the detector's filtering effect only allows the incoherent effects to be seen [108]. This purely elastic scattering calculation did not predict all of the contrast effects, however; TDS is also important.

5.3.2 Thermal diffuse scattering in Bloch wave theories

Bloch states that are concentrated around atoms also experience more TDS, as they pass closer to the core electrons. This acts in addition to the filtering effect of the ADF detector [109]. TDS imposes additional incoherence in the beam direction; the coherence length in the longitudinal direction is generally

considered to be of the order 3-5 atoms [117]. The vibrations of atoms in the same column are only over this short distance correlated enough to give coherent thermal diffuse scattering. This partial longitudinal incoherence is why few thickness fringes are observed in HAADF STEM images.

5.3.3 Application to dislocations

Perovic, Rossouw and Howie [57] observed unusual behaviour in HAADF STEM dislocation contrast and proposed an explanation in terms of Bloch waves (Equation 5.4). It is assumed in this model that scattering to the ADF detector is entirely in the form of thermal diffuse scattering, and each Bloch state has a different mean free path for TDS. Their work used a rather higher scattering angle than the work in this thesis ($\beta_{in} = 105$ mrad, the same as β_{out} for the GaN tilt series), so there was no ZOLZ Bragg scattering included; also, their work concentrated on exact zone axis orientation.

The exit wave $\Psi(\mathbf{r})$ showing dislocation contrast in this model as a function of position \mathbf{r} in the crystal is given by Equation 5.4.

$$\Psi(\mathbf{r}) = \sum_j \alpha^{(j)}(z) \exp(-2\pi i \eta^{(j)} z) \sum_g C_g^{(j)} \exp(2\pi i (\mathbf{k}^{(j)} + \mathbf{g}) \cdot (\mathbf{r} + \mathbf{R})) \quad (5.4)$$

Here, $\alpha^{(j)}$ is the excitation amplitude of Bloch wave j , dependent on z because of the defect. $\sum_g C_g^{(j)} \exp(2\pi i (\mathbf{k}^{(j)} + \mathbf{g}) \cdot (\mathbf{r} + \mathbf{R}))$ is a standard Bloch wave in an imperfect crystal with defect displacement field \mathbf{R} , for Bloch waves of wavevector $\mathbf{k}^{(j)}$ and wave amplitudes at diffraction vector \mathbf{g} given by $C_g^{(j)}$. Bloch wave index j was i in their original paper, but has been changed here to avoid confusion with $\sqrt{-1}$.

The important element for ADF STEM, $\exp(-2\pi i \eta^{(j)} z)$, is the phase factor that incorporates the different scattering efficiencies of different Bloch waves: the wavevectors of the Bloch states are made complex, with a real (elastic) part and an imaginary (absorptive, TDS) part: $k^{(j)} = \gamma^{(j)} + i\eta^{(j)}$ [95]. $\eta^{(j)}$ is related to Bloch wave j 's TDS mean free path as $\lambda^{(j)} = 1/2\eta^{(j)}$ and is used to introduce this extra phase shift.

When they used this expression to calculate wave amplitudes as scattering

proceeded through a dislocated crystal, it was found (similar to the previous Bloch wave theory) that 99% of the electron flux stayed in $1s$ -like, $2s$ -like and $2p_x$ -like states (illustrated in [111]), and was redistributed among them as the dislocation was encountered. $1s$ and $2s$ are peaked around the atom columns and their wavevectors do not change much with propagation, but $2p_x$ is peaked between the columns and is more dispersive. Because of their position, the $1s$ and $2s$ states are more prone than the $2p_x$ to being scattered to the ADF detector by TDS, so have higher values of $\eta^{(j)}$.

Dislocation contrast in their HAADF STEM images showed a dark plug near the entrance surface, oscillatory contrast to a depth of ≈ 70 nm in silicon for convergence semiangle $\alpha = 6.2$ mrad, and bright contrast thereafter with no special features at the exit surface [95] (Figure 5.3 gives a schematic diagram of this). They proposed that in the dark plug, the dislocation transferred electron flux from the s into the p state, which experiences little TDS and appears dark. After a short distance the flux began to be transferred from the dispersive p state back to s , and scatter to TDS; there followed beating between the two waves, and as s scatters more than p , the line appeared striped. The period of this oscillatory contrast corresponded to beating between those two Bloch states. Eventually the s state was depleted, and flux fed in a trickle from p to s where it was scattered to the detector, giving a steady bright intensity.

As convergence angle of the beam was increased to $\alpha > \theta_B$, the oscillatory contrast region shortened and disappeared; this was interpreted as the higher angle components of the incident probe exciting p states and not s , so that there was less intensity transferred dramatically from $s \rightarrow p$ at the entrance surface to set off the oscillations; effectively, the initial force that caused the oscillations was weaker. This interpretation is plausible; it may be valuable further work on this project to simulate this behaviour at different orientations, perhaps by adapting existing simulation programs to incorporate the additional phase factor, and compare it and the multibeam Bragg simulation in Section 5.2.1 against STEM images in these tilt series. It may also contribute to explaining why the dislocation images obtained are broader than the Huang cross section calculated in Section 5.2.3.

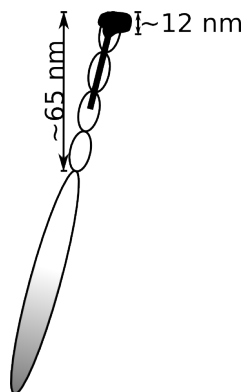


Figure 5.3: Schematic diagram of the HAADF contrast ($\beta_{in} = 105$ mrad, $\beta_{out} = 300$ mrad) at a dislocation on a $(1\bar{1}1)$ plane threading from top to bottom of the $\langle 110 \rangle$ foil in Si reported by Perovic, Howie and Rossouw [95]. The sketch represents the TEM image when the crystal is tilted (angle unreported). Lengths marked are the true depths in the crystal represented by the projected depths in the image. Total crystal thickness in this region was 177-190 nm. Fringed contrast was also seen in images from the GaN ADF tilt series, with $\beta_{in} = 34$ mrad, $\beta_{out} = 105$ mrad.

The characteristics of thermal diffuse scattering, and the implications of this for defect contrast, give an interesting possibility for the analysis of this contrast, illustrated in Figure 5.4. On the basis that the scattering contributing to the HAADF STEM image is incoherent in the transverse direction and partially coherent in the longitudinal direction, it has previously been assumed that only a displacement component in the longitudinal direction can be seen in the HAADF regime [120]. For an edge dislocation, the displacement is mainly in the direction parallel to \mathbf{b} ; therefore, for maximum scattering to HAADF, \mathbf{b} should be parallel to the beam direction, i.e. perpendicular to \mathbf{g} . In other words, **at this maximum contrast geometry, $\mathbf{g} \cdot \mathbf{b} = 0$** . This is directly the opposite of conventional DF dislocation contrast, for which contrast should be at a minimum when $\mathbf{g} \cdot \mathbf{b} = 0$. Finding the dependence of contrast on $\mathbf{g} \cdot \mathbf{b}$ could in principle give a guide as to which regime of contrast dominates for this low-to-medium scattering angle, Bragg scattering as for conventional TEM or Huang scattering and TDS as for HAADF-STEM. This idea seems quite incongruous at first, and should be experimentally investigated, which has not yet been completed.

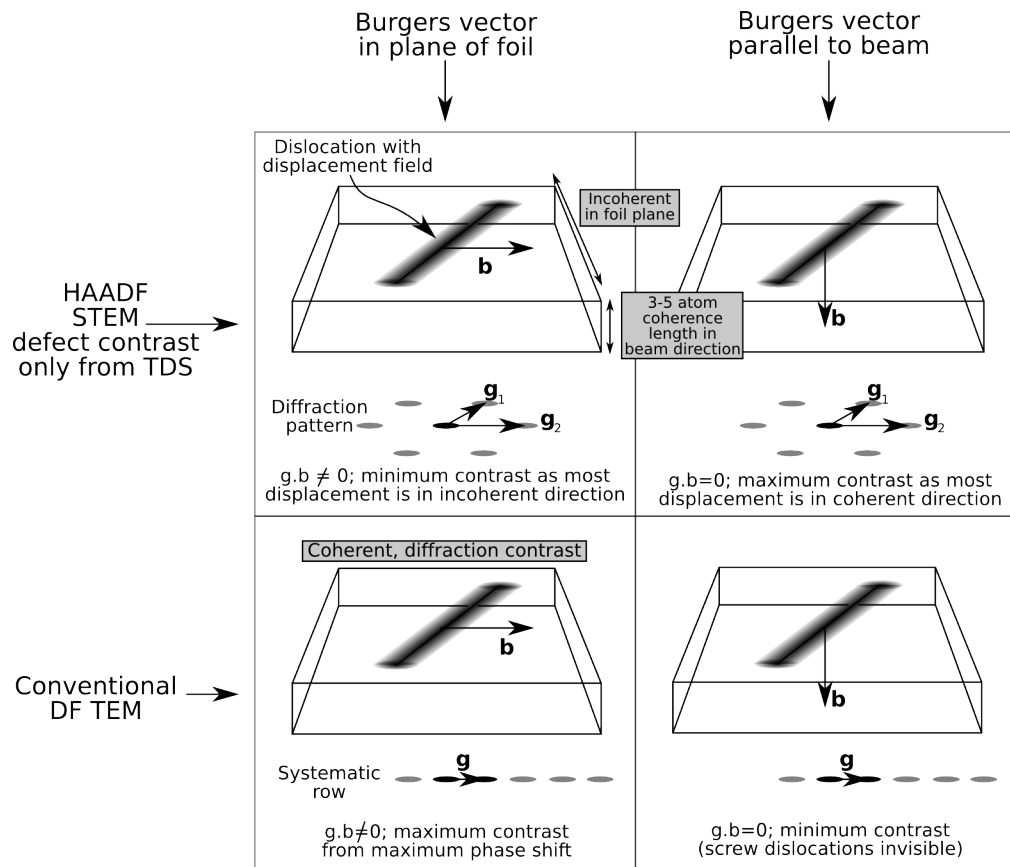


Figure 5.4: Schematic diagrams showing the possibility of opposite extinction conditions between HAADF-STEM and conventional DF defect images. Top row: HAADF-STEM imaging is incoherent in the foil plane but has a coherence length of 3-5 atoms in the beam direction [126]; strain field contrast should be at a maximum when the highest strain is parallel to the coherent direction, i.e. the beam direction. Bottom row: the extinction situation for conventional DF TEM.

5.4 Dechanneling

When the crystal is precisely oriented at a zone axis (typical tolerance: 4 mrad for [111] zone axis of Si with the nearest 220 peak $2\theta_B$ away at 19.3 mrad [127]), the electron beam can be confined to atom columns parallel to the beam (axial channeling), or if the columns are tilted in a direction such that they project as planes, the beam can be confined to this plane [128].

In a semi-classical explanation of channeling, the electrons rebound from the sides of the well as they pass down the atom column or plane [129]; this is valid for ions, or low mass particles travelling with large energies, i.e. many MeV. In the electron microscope, it is considered that the beam is fed directly into the lowest energy Bloch states, instead of being allowed to enter many states of various energies like a broad beam [109], [111], [127], [130]. These states are localised around atom strings or planes, and this behaviour, essentially dynamical scattering, is referred to as channeling.

During channeling, dynamical diffraction can be simplified in the case of a perfect crystal and the atom columns can be thought of as strings of lenses, co-operatively focusing intensity to travel along their optic axes [127]. As the crystal is tilted away from an exact zone axis orientation, higher order Bloch states that are not concentrated on the atom strings become the majority excited states, and the channeling condition is broken. The convergent beam also has an effect: electrons incident at $\alpha < \theta_B$ (CBED discs on detector do not overlap) are channeled along planes, whereas electrons incident at $\alpha > \theta_B$ (CBED discs do overlap) are antichanneled — they propagate between planes [130]. At these orientations we normally get a combination of channeling and antichanneling peaks [127]. Channeling peters out at ≈ 100 Å in columns of heavy elements from losses to TDS and Rutherford scattering, but in light elements can channel several times this distance [131].

Dechanneling is the term coined by Cowley and Huang [58] for what happens when a channeled electron beam encounters a crystal defect. If the columns or planes are tilted around the defect, the channeling condition is broken (higher order Bloch waves are excited) and the scattering distribution spreads out to that akin to an off-axis (many excited state) situation. An

annular detector arranged around the outside of the channeled diffraction pattern should receive more intensity when the probe passes areas that cause dechanneling to occur; thus the ADF STEM signal should be higher and the image pixels brighter from the defect region. This depends, however, on the beam being channeled before encountering the defect; this will be considered in Section 5.6.

5.5 Inner detector angle

Liu and Cowley studied what happened to ADF STEM dislocation contrast at different inner detector angles 20, 60 and 100 mrad in a sample of heat-resistant alloy [132]. At 20 mrad (within the ZOLZ) the dislocation images were wider than in the BF-STEM image, with diffraction contrast. As the inner detector angle was increased, less diffraction contrast was observed; some dislocations also became invisible, and in general dislocation images became sharper and less intense. This is consistent with a switch to an incoherent contrast mechanism such as Huang static strain scattering, which should come mostly from the dislocation core.

A similar experiment was carried out using the Cambridge Tecnai F20 to find the optimal camera length before the GaN ADF STEM tilt series was taken, using lower inner detector angles 50.0, 34.0, 23.0, 17.5, 11.6, 7.1 and 5.1 mrad, corresponding to 70, 100, 150, 200, 300, 490 and 680 mm camera lengths. In terms of the Bragg angle for the $(11\bar{2}0)$ planes, these are 6.25, 4.38, 2.88, 2.19, 1.45, 0.89 and $0.64 \theta_B$. The sample used for this was plan view (0001) GaN, with dislocations visible in the plane of the film. The results are shown in Figure 5.5. The dislocations show bright/dark contrast, which switches side with respect to the dislocation core between low and high inner detector angle. At the smallest inner detector semiangle $0.64 \theta_B$, the dislocation contrast is dark at the chosen dislocation, though one above it in the image shows light/dark contrast still. This changing from light to dark contrast is to be expected; at inner detector semiangles below θ_B , the bright field disc is beginning to be included, and the image is part dark field and part bright field.

The direction reversal for the light/dark contrast is less expected. The changeover semiangle from Bragg to TDS being the strongest scattering (Figure 4.2) is 38.2 mrad for GaN; this occurs between 100 mm and 150 mm camera lengths, approximately where the light/dark contrast reversal occurs. It can be seen in Figure 5.5 that the light/dark contrast is not in the same sense for each dislocation; some are opposite to others, notably the two vertical dislocation lines at the top of the 490 mm and 300 mm images. In conventional DF dislocation images, the dislocation image switches from one side of the core to the other when $(\mathbf{g}\cdot\mathbf{b})s$ changes sign (s is the extinction error). Either or both of s and \mathbf{g} could change sign if there is a misalignment of the crystal or detector respectively — shown in Figure 5.6.

5.5.1 Importance of Higher Order Laue Zones to ADF STEM dislocation images

Early on in analysis of ADF STEM contrast it was found in multislice simulations that as the inner detector angle was increased, the contrast of high-resolution HAADF-STEM images changed suddenly as the FOLZ was included, and contrast reversal occurred as focus changed if the FOLZ was included [105]. Experimentally, this was not found to occur [133]; later studies have agreed with this and treated the FOLZ contribution to contrast as much smaller than TDS such that it can be ignored [115], [109].

5.6 Application of ADF STEM contrast to tomography: the effect of tilting

Most analyses of ADF STEM contrast other than Z-contrast tomography have concentrated on a single orientation, or very small tilts used to assess the effects of breaking a channeling orientation [134] or using different zone axis channeling orientations [96]. Studies that concentrate on tilting are on the topic of high-resolution imaging in a perfect crystal, not defect contrast.

In tomography, the orientation of the sample changes a great deal,

and the Bloch states that are excited change with it. The importance of dechanneling contrast depends on the changes in diffraction conditions between tilt angles. If the sample ends up in a channeling orientation at some tilt angles, dechanneling may occur and boost ADF intensity at the defect, but if channeling orientations are never or very rarely found in the tilt path, then dechanneling contrast can probably be ignored and analysis becomes simpler. Dechanneling occurring at some angles but not all, is a factor that would change the dislocation contrast between tilt angles, and as such it would be wiser to avoid it throughout tilt series acquisition than include it at some angles and introduce inconsistency into the tilt series.

A selected area channeling pattern or channeling map [111] [135] would be a good tool to investigate the frequency of strong channeling/zone axis orientations along the tilt path. The tomographer could use this to plot a tilt path to keep diffraction conditions as constant as possible across the tilt series — probably by avoiding zone axes as much as possible. Unfortunately this possibility was not available on the Tecnai F20 used for STEM tomography.

To gain an idea where channeling orientations may have occurred for these experiments, lines were superimposed on the relevant $(11\bar{2}0)$ projection of the GaN lattice, shown in Figure 5.7. As a measure of the likelihood of meeting a channeling orientation, the **string strength** was used, given by P_s in Equation 5.5 [136] in which γ is the relativistic factor $c/\sqrt{c^2 - v^2}$, $\sum_i (Z_i)$ is the sum of the atomic numbers of atoms in the string, S_o is the area belonging to the string in the foil plane, and d is the spacing of atoms along the column.

$$P_s = \gamma \sum_i (Z_i) \frac{S_o}{d} \quad (5.5)$$

In this calculation the situation is complicated somewhat because the ‘strings’ in question are not necessarily at zone axes. The area belonging to each string is represented by the projected area of the unit cell shared between the number of columns in it (including the set of atoms in the other, positionally displaced $(11\bar{2}0)$ plane in the unit cell, which would occur $a/2$ behind that pictured in Figure 5.7). The spacing between atoms down the string is the length of the string divided by the number of atoms in it, which is probably

the biggest source of error in this calculation as the spacing is not necessarily uniform and this will have some effect on the propagation of the probe. The numbers of atoms in each string were recorded by eye from Figure 5.7, noting also for each angle whether there were two string types of different composition (i.e. different string strength) per unit cell, or two of the same composition (i.e. same string strength) per unit cell. The string strength with tilt angle is plotted in Figure 5.8. Those angles for which there are two strings of different composition have two points; for those with two strings of identical composition, only one point is plotted.

[0001] (0° tilt) is an obvious zone axis; between 45° and 47.5° there is also an orientation where the beam passes down a regular pattern of Ga-N dumbbells inclined to the beam, i.e. the $[1\bar{1}01]$ zone axis at 46.8° (Figure 5.7), giving a high string strength at 45° . The $+45^\circ$ image from the GaN tilt series shows fringes typical of dynamical contrast in the threading dislocations, similar to that found by Perovic, Howie and Rossouw in ADF STEM images of Si at higher magnification [95]. This is not seen in the -45° image, which is to be expected because the crystal structure does not have a mirror plane on $(\bar{1}100)$ such that strings seen from tilts θ and $-\theta$ would be identical.

Other orientations showing high string strength are 52.5° , 40° and 27.5° ; dislocation images were strongly fringed at these orientations. Conversely, 15° has very low string strength, and the dislocation images at this tilt (shown in Figure 5.7) are well-defined but not strongly fringed. It appears that string strength estimated even in this simple way could be a valuable guide in predicting where the contrast will show dynamical features and where it will not, and therefore in planning a tilt path before the experiment.

It is also possible that **planar** channeling occurs throughout the tilt series as the sample is tilted about an axis parallel to a certain \mathbf{g} ; however, it was seen in all of the WBDF tilt series that the diffraction condition differed by more than \mathbf{g} , enough to break a channeling alignment ($\mathbf{g}_{(11\bar{2}0)} \approx 8$ mrad for GaN), so it would be unwise to assume a planar channeling orientation was held throughout a STEM tilt series.

5.7 Conclusions and further work

Adequate reconstructions that showed dislocation paths moderately clearly have been attained from the empirically optimised tilt series presented in Chapter 4. The TiAl tilt series had extinctions typical of ordinary dark-field diffraction contrast, which were problematic for tomography, and were probably caused by using a detector with too small an inner detector angle; if the inner detector angle is large enough, extinctions may be avoidable. Fringed dislocation images at various tilt angles in the GaN tilt series correspond with possible channeling orientations, suggesting that channeling/Bloch wave interference and therefore the dechanneling mechanism of ADF STEM defect contrast is relevant at some angles in a tilt series but not most. However, this is only one piece of data, and other investigations would be needed to show any correlation.

The additional thermal diffuse scattering intensity due to changes in atom site volume from the dislocation's displacement field has been calculated and shown to be negligible. Huang scattering, however, should be visible above the background, but a simple calculation for the Huang scattering cross section gives a value an order of magnitude smaller than the width of the dislocation lines in real ADF STEM images. The extra broadening could be from rescattering of the Huang scattered intensity. The remaining contribution to ADF STEM dislocation intensity is changes in TDS intensity from redistribution between differently absorptive Bloch states at the dislocation; predicting this is future work (see also Chapter 6).

ADF STEM dislocation images are produced by many scattering processes; to predict the best orientation and other conditions for ADF STEM dislocation tomography, more theoretical work is needed. Further ADF STEM dislocation tomography experiments would be improved if the tilt axis were better aligned with the crystal axes; following these initial attempts at dislocation tomography and the misalignments found, others in the group have done further dislocation tomography with extensive checking and correction of the alignment during tilt series acquisition to improve this alignment (J.S. Barnard and M. Haeberlain, *pers. comm.*). Ideally, the tilt

axis should be oriented better than the channeling tolerance of ≈ 4 mrad, so it can be known what the situation is with regard to planar channeling. A selected area channeling pattern from the specimen would be a useful aid in ADF STEM for choosing a tilt axis that avoids strong channeling orientations in the tilt path, to keep the dislocation contrast throughout the tilt series as consistent with tilt angle as possible.

In terms of theory, it is important to check the hypothesis that choosing the detector to omit the first set of Bragg spots will avoid extinctions of dislocations in the tilt series. More images and CUFOUR simulations from corresponding materials and orientations should be obtained for Bragg contrast, to find whether the approach of adding images from all DF spots in the diffraction pattern is a reasonable way to simulate the Bragg contribution to ADF STEM dislocation images. Convergence at zone axes should also be incorporated in the simulation program.

The same simulation software could be adapted to model ADF TDS contrast using the approach presented by Perovic, Howie and Rossouw [57]. This could then be used with the Bragg multibeam approach to investigate the contributions to the ADF STEM image, and check whether this predicts an image width more similar to that seen experimentally. In addition, the behaviour of dislocation image intensity with $\mathbf{g}\cdot\mathbf{b}$ should be investigated as a method of finding which scattering regime dominates, as suggested in Section 5.3.3.

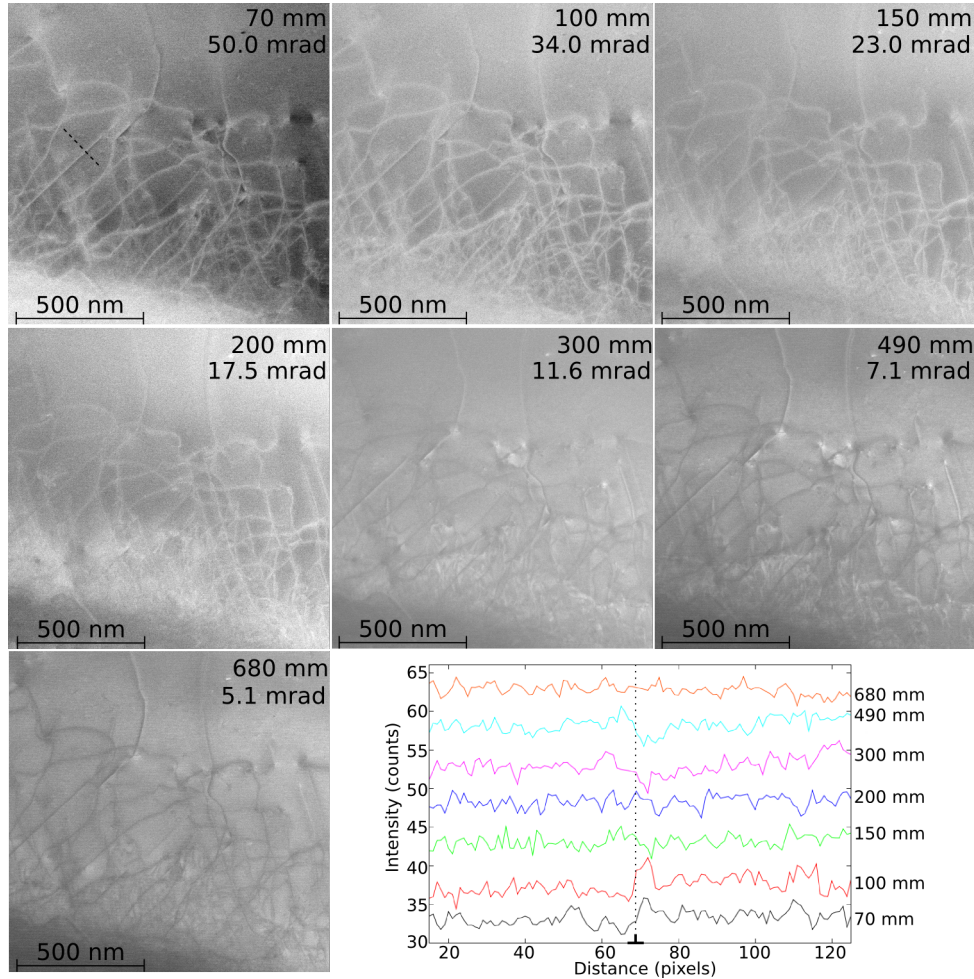


Figure 5.5: Set of ADF STEM images from GaN sample, taken before the ADF STEM tilt series to find the optimal camera length. Camera lengths and corresponding annular detector inner collection angles are shown. The plot shows line traces across the dislocation marked by a dotted line in the 70 mm image; the position of the dislocation is approximately shown by the vertical dotted line on the plot. Contrast reverses between the shortest and longest camera lengths, with intermediate images showing weak dislocation contrast — the dislocation is barely discernible from those line traces. The line traces are arranged in order of camera length, so the absolute intensity values are not correct, but the relative sizes of the intensity variations are correct. The images' contrast and brightness have been changed here to improve visibility; line traces were taken from the original images. Images obtained by JSB and author.

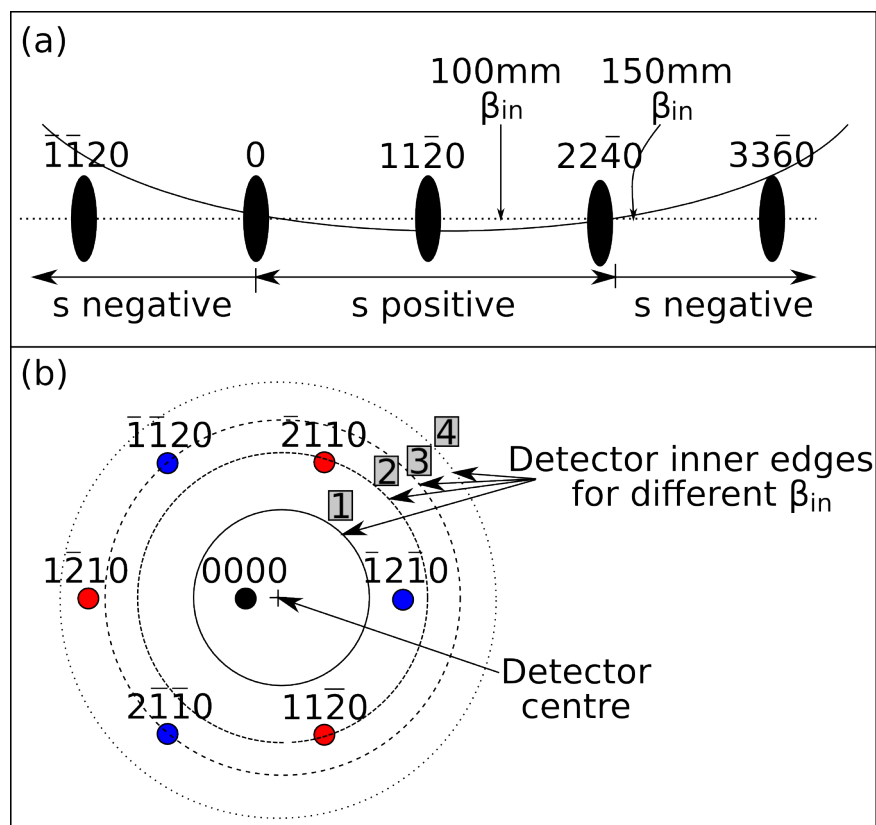


Figure 5.6: How the black/white contrast of ADF dislocation images may change sense as the camera length is increased. (a) The lowest order Bragg reflection received by the annular detector is the strongest, because of the exponential fall-off in Bragg intensity with scattering angle (Figure 4.2). As the inner acceptance radius moves out, this may change from one for which excitation error $s < 0$ to one for which $s > 0$, which would change the side of the black/white contrast in that reflection's DF image contributed to the final ADF STEM image. This would occur if the crystal is at systematic row, not zone axis, orientation. (b) If the annular detector and the diffraction pattern do not share a centre, the balance of $+\mathbf{g}$ (red) and $-\mathbf{g}$ (blue) over all the discs collected by the annular detector may change as the inner acceptance radius is changed. Here, radius 2 receives one $-\mathbf{g}$ and two $+\mathbf{g}$; radius 3 receives three $-\mathbf{g}$ and two $+\mathbf{g}$; radius 4 receives three $-\mathbf{g}$ and three $+\mathbf{g}$. The sense of the dislocation image from $-\mathbf{g}$ and $+\mathbf{g}$ images should be opposite; if there are more of one sign than the other, the sense of the final image should be in favour of the dominant sign of \mathbf{g} .

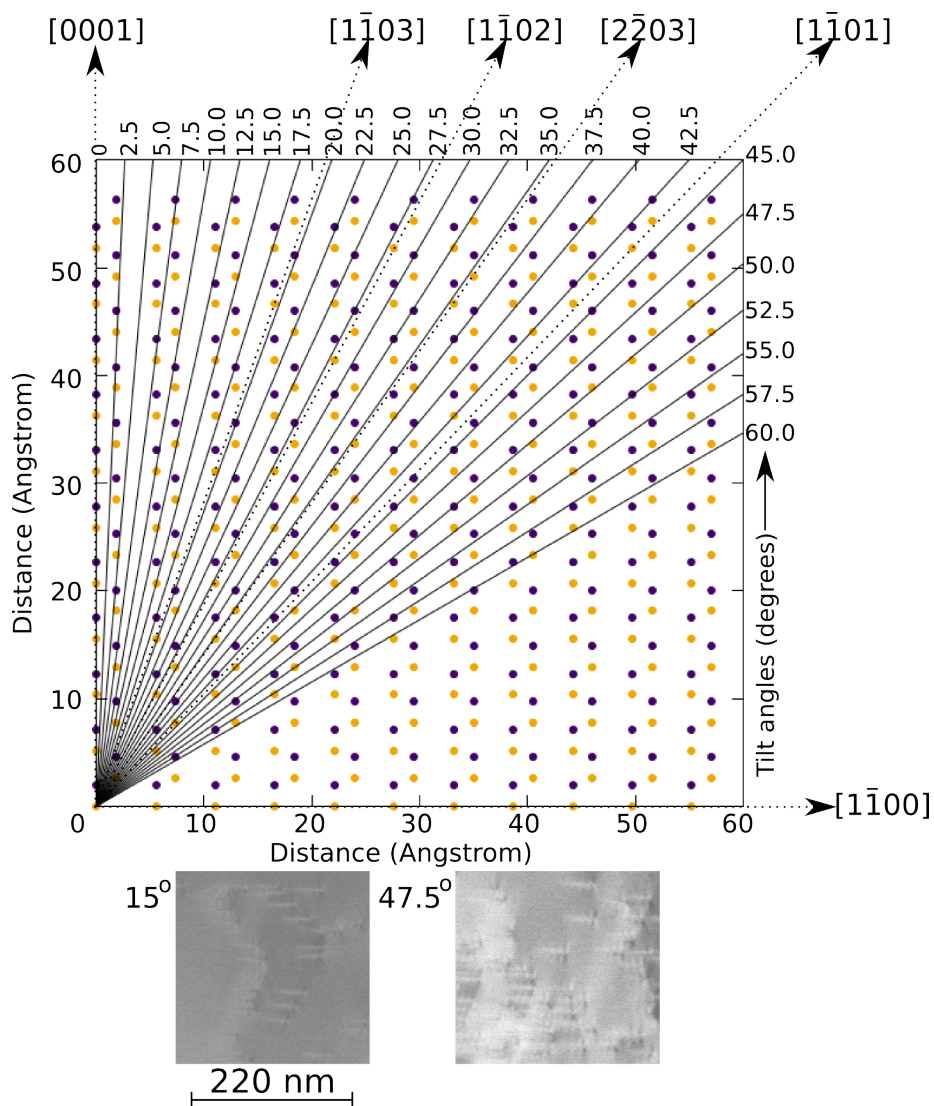


Figure 5.7: Top: tilt angles in GaN ADF STEM tilt series superimposed on a GaN crystal (only positive angles shown). Yellow and blue atoms are Ga and N. Below: though other images in this series (section of 15° image shown for comparison) show some dynamical effect, the 47.5° image (section shown) particularly exhibits fringed threading dislocations, a dynamical effect.

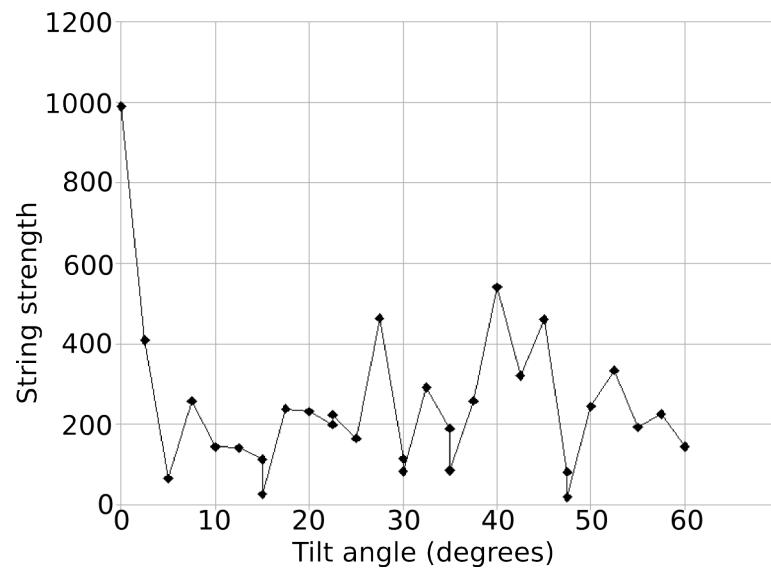


Figure 5.8: Plot of string strength (Equation 5.5) with angle for GaN; high string strength orientations appear to give fringed images resulting from more dynamical scattering (channeling), low string strength orientations give images that are more like simple lines.

Chapter 6

Conclusions and further work

6.1 Conclusions from weak-beam dark-field tomography experiments

Tilt series of weak-beam dark-field images can be used for tomography to produce a reconstruction of dislocations in the sample; this has been done for GaN, for dislocations surrounding a microcrack in Si and for a TiAl ordered alloy. Elongation occurred in the missing wedge direction (foil normal) by a factor of 3.1 in GaN, where the missing wedge should only elongate by a factor of 1.5; extra elongation may be due to anisotropy in the position of the WBDF dislocation image and misalignment effects. The elongation of dislocations in the TiAl reconstruction was that expected from the missing wedge effect alone.

Thickness contours pose a problem for alignment and reconstruction but this effect can be minimised by keeping thickness contours to the edge of the images, filtering them out of the alignment with a Hanning window, and cutting them out of the reconstruction volume before starting. The microcrack in the Si sample, showing fringed contrast in WBDF, was found not to reconstruct accurately from WBDF images, producing an object that was not planar; it also impaired reconstruction of the dislocations near its surfaces, as the fringed contrast caused fine alignment to fail. Simulations showed that the movement of stacking fault fringes during tilting resulted in

a reconstruction that resembled a 3D array of rods, i.e. was not planar.

Misalignment of the tilt axis with the intended crystal axis during weak-beam dark-field tilt series acquisition was found in simulation to have an extremely negative effect through the resultant change in diffraction conditions throughout the tilt series. Simulations with different tilt axis misalignments showed that as misalignment increased, the dislocations are reconstructed as thicker objects at incorrect angles of inclination to the foil surfaces.

6.2 Conclusions from annular dark field STEM tomography experiments

Annular dark field STEM was also found a suitable technique to acquire tilt series for dislocation tomography. In the case of the microcrack in Si, ADF STEM did not show moiré fringe contrast at the crack surfaces but a weak constant intensity at some angles. The resulting tomogram did not contain the microcrack, only the dislocations surrounding it, and was more successful than the weak-beam dark field reconstruction of the same defect in this respect. ADF STEM images also generally required less manual image processing for successful alignment, and were suitable for automatic specimen drift correction during tilt series acquisition, making ADF STEM defect tomography much faster and more straightforward for the user.

Dislocation contrast in ADF STEM varied within each tilt series, with some images sharper and narrower than others. For the tilt series taken in a TiAl alloy, which was the only ADF STEM tilt series for which the detector included the first Bragg spots from the central beam, extinction of dislocations was observed at some tilt angles. It was proposed that the exclusion of the first Bragg spots may preclude most of this dynamical behaviour.

Analysis of the factors contributing to ADF STEM contrast showed the topic to be complex and not yet fully understood. Additional thermal diffuse scattering (TDS) from changes to site volumes in the dislocation displacement

field was modelled using a simple Einstein model and found to be negligible, a factor of 10^9 smaller than background TDS.

It was estimated that Huang scattering (analogous to thermal diffuse scattering except from the dislocation's static displacement field) should have a significant contribution to ADF STEM dislocation contrast, but the image width should be 30\AA — ten times thinner than the actual image width found. A possible reason for this is broadening due to thermal rescattering of Huang scattered intensity. Additional ADF STEM contrast could originate from Bloch state population redistribution by the dislocation causing changes in TDS intensity as described by Perovic, Howie and Rossouw [57] but this has not yet been investigated as a possible cause of broader lines.

Dechanneling is another widely considered cause of ADF STEM dislocation images at zone axis orientations; channeling and dynamical diffraction within a small number of beams are the 'particle' and 'wave' equivalents of each other to describe the behaviour of electrons in the TEM. A study of the string strength of the crystal with tilt found channeling to be possible at some tilt angles over the GaN tilt series. These strong string orientations correlated with images for which the strongest oscillations were observed on threading dislocations, an effect of dynamical scattering.

6.3 General conclusions

The transfer function introduced by Norton [72] for algebraic reconstruction techniques as used here gives a far more pessimistic prediction for the possible resolution of dislocation tomography than is achievable. Reconstructions of a test object with a range of cosine gratings indicated that finer frequencies are attenuated less than expected, as the transfer function levels off. While Norton's transfer function starts from zero, Inspect3DTM's SIRT uses a backprojected reconstruction as the first estimate, which appears to make the difference for small spacings.

6.4 General experimental improvements

- Using ADF STEM imaging allows use of automatic feature retrieval to correct major shifts during tilting between images; this improved the ease and speed of defect tomography. The next improvement would be to allow automatic focusing, which is currently required to be done by the operator; this is somewhat of a pipedream in the case of dislocation images. If implemented this would also standardise focusing and enable better analysis of ADF STEM defect contrast, while currently diffuse contrast may be an actual feature of the scattering or merely human inconsistency in focusing.
- It is also important for both imaging techniques to align the tilt axis well; to within 4 mrad (a quarter of the way between Bragg spots for e.g. Si low order spots) if analysis of the relevance of dechanneling to ADF STEM defect tomography is to be investigated. The first way to improve this is to temporarily switch to diffraction mode, check and correct the tilt axis regularly throughout the experiment, currently implemented by others carrying out dislocation tomography following these studies. This is good enough to keep the diffraction condition moderately constant but it would facilitate conclusions about dechanneling if a more convenient method could be introduced for finer alignment.

6.5 Further work on WBDF tomography

- Theoretical analysis was started to find the orientation for WBDF tomography of a stacking fault that results in minimum fringe movement with tilt, to give minimal ‘array of rods’ artifacts on reconstruction. This developed into a complex problem and was postponed; it should be restarted in the near future.
- The software used here for Bloch-wave simulations of weak-beam dark-field defect images (CUFOUR) does not model the physical rotation

of defects correctly when the incident beam direction is changed, as this was not in the original specification for the program; simulation of tilt series using CUFOUR has restrictions on tilt axis because of this problem. The software could be augmented to enable arbitrary tilt axis orientations and check the theoretical analysis in the above point. Different software that can do this is yet to be found by the author; suggestions are welcome.

- It would also be useful to augment the author's Perl script for tilt series simulation, to rotate the crystal with even increments and to a maximum tilt angle chosen by the user; currently it is a quick fix written for the problem at hand.
- High magnification WBDF tilt series (i.e. a single stacking fault in the image) would be needed to experimentally check the results of the theoretical analysis of optimal stacking fault tilt axis orientation. This is limited by the ability to recover the correct area of interest after tilting at the low intensities typical of WBDF imaging, which is difficult enough for the medium magnification images obtained here in which larger features at the edge of the image provide a helpful guide. This is dependent on proficiency at the microscope, which comes with experience.
- Higher magnification tilt series would also aid investigation of the elongation of dislocations in the foil normal direction, greater than that expected from the missing wedge effect. In current tilt series, measuring the elongation is a matter of individual pixels, which is not accurate enough to assess whether it corresponds to hypotheses for the origin of this additional elongation.
- Ultimately, the reconstruction algorithms used here assume the images are direct projections, when they are not; they are projections of the function $\exp(-2\pi i\mathbf{g}\cdot\mathbf{R})\exp(-2\pi isz)$ (\mathbf{g} is diffraction vector, \mathbf{R} displacement field, s excitation error, z co-ordinate in beam direction). This situation is adequate for recovering the paths of dislocation cores,

as is done here. If a reconstruction algorithm could be used that takes into account the true method of propagation that produces WBDF images, unprecedented levels of detail about the defects could be recovered. This would be a difficult task, but would be worth pursuing.

6.6 Further work: ADF STEM tomography

- The relevance of dechanneling contrast should be investigated by taking an experimental channeling pattern of the sample before a tilt series, and aligning the sample to within 4 mrad of the intended orientation for each image. This poses a problem for self-supporting samples, as it is difficult to fix a self-supporting sample in the holder well enough that no small rotations occur with tilt, without damaging the sample.
- To investigate the hypothesis that the first ring of Bragg spots is key to whether the contrast is dominated by dynamical low-angle diffraction or mid-angle Huang and thermal diffuse scattering, more data must be compared. In order to do this, the multibeam approach to simulating STEM diffraction contrast must be made to work for corresponding experimental images.
- The effect of Bloch state transitions on TDS as proposed by Perovic, Howie and Rossouw [57] could be modelled with an adaptation of CUFOUR; this could be used with the multibeam approach in the previous item.
- The variation in intensity with $\mathbf{g}\cdot\mathbf{b}$ at different ADF STEM detector angles should be investigated as a potential empirical method to diagnose which contrast mechanisms dominate at different inner detector angles, and thus which camera length should be used for a particular sample.
- The extinction behaviour of the bands of four dislocations in TiAl as related to the incidence of superstructure diffraction spots on the annular detector should be investigated. A higher magnification tilt

series of either technique should be obtained and reconstructed for this material, from a sample which has been plasma cleaned or differently prepared (whichever improvement removes the speckle effect seen in the ADF STEM tilt series), in order to complete the analysis which was the original goal — to find out whether one dislocation of the four climbs out of the band plane or not. This is a very appropriate materials problem for defect tomography.

Appendix A

Fourier slice theorem for WBDF images

This appendix contains a brief algebraic check of the statement described in subsection 3.2.2, that:

The Fourier transform of an electron micrograph taken at a tilt angle θ is equivalent to a slice inclined by θ from zero tilt, through a Fourier transform of the intensity of the ‘object’ reconstructed from a tilt series of such images by an algorithm based on the conventional Fourier Slice Theorem.

It begins by mirroring the derivation of the Fourier Slice Theorem as described in Kak and Slaney’s *Principles of Computerized Tomographic Imaging* [61].

The Fourier transform of an object, in this case magnitude of the displacement field $\mathbf{R}(x, y, z)$, is shown in Equation A.1 where (x, y, z) are real-space coordinates with z following the beam direction and (u, v, w) are frequency coordinates in the corresponding directions. (This breaks the usual convention that $F(u, v, w)$ is the Fourier transform of $f(x, y, z)$ because it will make the notation clearer later.)

$$F_R(u, v, w) = \int_{-\infty}^{\infty} \int_{-\infty}^{\infty} \int_{-\infty}^{\infty} |\mathbf{R}(x, y, z)| \exp(-2\pi i(ux + vy + wz)) dx dy dz \quad (\text{A.1})$$

Taking a slice through this Fourier transform at $w = 0$ (i.e. a central slice perpendicular to beam direction z) reduces this to Equation A.2. At this point we may also redefine the limits on the z integral; since the sample is not infinite in the z direction the integral may as well be taken over the sample thickness t .

$$F_R(u, v, 0) = \int_{-\infty}^{\infty} \int_{-\infty}^{\infty} \left[\int_0^t |\mathbf{R}(x, y, z)| dz \right] \exp(-2\pi i(ux + vy)) dx dy \quad (\text{A.2})$$

At this point in the derivation of the conventional Fourier Slice Theorem, the term in square brackets in equation A.2 is seen to be identical to the projection (Radon transform) of the object $|\mathbf{R}(x, y, z)|$ as measured by a straight-ray non-diffracting imaging technique, $\int_{-\infty}^{\infty} |\mathbf{R}(x, y, z)| dz$, leading to the final step. This term is the projection image of the type used as input for a backprojection tomographic reconstruction method. We will replace it with our dark-field image in Equation A.3 and find the consequences.

$$F_{DF}(u, v, 0) = \int_{-\infty}^{\infty} \int_{-\infty}^{\infty} \left[\frac{i\pi}{\xi_g} \int_0^t \exp(-2\pi i \mathbf{g} \cdot \mathbf{R}(x, y, z)) \exp(-2\pi i s z) dz \right]^2 \times \exp(-2\pi i(ux + vy)) dx dy \quad (\text{A.3})$$

Here the term in the square brackets is the dark-field intensity derived using the kinematical and two-beam approximations; it is the square of the amplitude in Equation 3.1. If it were possible to do the z integration and then reverse the Fourier transform, an analytical expression could be found for the ‘object’ reconstructed by the conventional technique in response to the images given. However, the form of the displacement field $\mathbf{R}(x, y, z)$ makes the integration impossible even for the simplest geometry, which is the reason dislocation images are simulated by Bloch wave or multislice methods instead of simply being calculated analytically. Instead the image will be given as I_g giving Equation A.4.

$$F_{DF}(u, v, 0) = \int_{-\infty}^{\infty} \int_{-\infty}^{\infty} I_g \exp(-2\pi i(ux + vy)) dx dy \quad (\text{A.4})$$

If Equation A.4 is inverse-Fourier-transformed in the x - y plane, Equation A.5 is arrived at. This states that the central slice through the reconstructed ‘object’ at zero tilt is the dark field image taken at zero tilt.

$$f_{DF,\theta=0}(x, y, z) = I_g(\theta = 0) \quad (\text{A.5})$$

This applies to not only zero tilt but all tilt angles; the rotation of the sample can be done by a rotation of real and Fourier space coordinate systems. Therefore, each central slice of the reconstructed ‘object’ is the image at that tilt angle, and the reconstructed object is the trace of where the intensity maxima fall from image to image in the tilt series. Considering the backprojection process, this intuitively makes sense; an image is backprojected through object space on a course that intersects this central slice, as well as slices at the same tilt angle that do not intersect the origin.

References

- [1] J P Hirth and J Lothe. *Theory of dislocations*. Wiley, 1982.
- [2] P B Hirsch, R W Horne, and M J Whelan. Direct observations of the arrangement and motion of dislocations in aluminium. *Philosophical Magazine*, 1:677, 1956.
- [3] P.B. Hirsch, A Howie, R B Nicholson, P W Pashley, and M J Whelan. *Electron Microscopy of Thin Crystals*. Butterworths, London, 1965.
- [4] R S Barnes and D J Mazey. Stress-generated prismatic dislocation loops in quenched copper. *Acta Metallurgica*, 11:281, 1963.
- [5] R Peierls. The size of a dislocation. *Proceedings of the Physical Society*, 52:34–37, 1940.
- [6] R.K. Ham. On the loss of dislocations during the preparation of a thin film. *Philosophical Magazine*, 7:1177, 1962.
- [7] A H Cottrell and B A Bilby. Dislocation theory of yielding and strain ageing of iron. *Proceedings of the Physical Society A*, 62:49–62, 1949.
- [8] B. W. Lagow, I. M. Robertson, M. Jouiad, D. H. Lassila, T. C. Lee, and H. K. Birnbaum. Observation of dislocation dynamics in the electron microscope. *Materials Science and Engineering A*, 309:445–450, 2001.
- [9] M J Whelan, P B Hirsch, R W Horne, and W Bollman. Dislocations and stacking faults in stainless steel. *Proceedings of the Royal Society of London*, A240:524–538, 1957.

-
- [10] A H Cottrell. *Dislocations and plastic flow in crystals*. Oxford University Press, 1963.
- [11] I R Kramer and L J Demer. Effects of environment on the mechanical properties of metals. *Progress in Materials Science*, 9:133, 1961.
- [12] H Mughrabi. Dislocation wall and cell structures and long-range internal stresses in deformed metal crystals. *Acta Metallurgica*, 31:1367–1379, 1983.
- [13] C St John. The brittle-to-ductile transition in pre-cleaved silicon single crystals. *Philosophical Magazine*, 32:1193–1212, 1975.
- [14] U Essmann. Die Versetzungsanordnung in plastisch verformten Kupfreinkristallen / The dislocation arrangement in plastically deformed copper crystals. *Physica Status Solidi*, 3:932–949, 1963.
- [15] V K Astashev and V I Babitsky. Ultrasonic cutting as a nonlinear (vibro-impact) process. *Ultrasonics*, 36:89–96, 1998.
- [16] A Bohg, E Mirbach, and L Schneider. Preparation of preselected areas of silicon wafers for transmission electron microscopy. *Journal of Physics E: Scientific Instruments*, 11:166–168, 1978.
- [17] R Stickler and G R Booker. Surface damage on abraded silicon specimens. *Philosophical Magazine*, 8:859, 1963.
- [18] L E Samuels. The surface deformation produced by abrasion and polishing of 70:30 brass. *Journal of the Institute of Metals*, 85:51, 1956-7.
- [19] Gatan Inc. *Dimpling ductile materials: technical note 9201*.
- [20] J W Steeds. Dislocation arrangement in copper single crystals as a function of strain. *Proceedings of the Royal Society of London, Series A, Mathematical and Physical Sciences*, 292:343–373, 1966.

- [21] L E Samuels. Surface damage produced by the electric-spark cutting process. *Journal of the Institute of Metals*, 91:191, 1962-1963.
- [22] P R Strutt. Preparation of thin metal foils from ordinary tensile specimens for use in transmission electron microscopy. *Review of Scientific Instruments*, 32:411–413, 1961.
- [23] J A Hugo and V A Phillips. A versatile jet technique for thinning metals for transmission electron microscopy. *Journal of Scientific Instruments*, 40:202–204, 1963.
- [24] S Mader, A Seeger, and C Leitz. Work hardening and dislocation arrangement of fcc single crystals. II. Electron microscope transmission studies of NiCo single crystals and relation to work-hardening theory. *Journal of Applied Physics*, 34:3376, 1963.
- [25] S. Mader, A. Seeger, and C. Leitz. Work-hardening of metal single crystals, slip lines and transmission electron microscopy. In N. P. Allen, editor, *Relation between structure and mechanical properties of metals*, number 15 in NPL symposium series, pages 3–38. National Physical Laboratory, HMSO, Teddington, 1964.
- [26] J C Grosskreutz and H Mughrabi. Description of the work-hardened structure at low temperature in cyclic deformation. In A S Argon, editor, *Constitutive Equations in Plasticity*, page 251. MIT Press, 1975.
- [27] U Essmann. Elektronenmikroskopische Untersuchung der Versetzungsanordnung in plastisch verformten Kupfereinkristallen. *Acta Metallurgica*, 12:1468–1470, 1964.
- [28] Bernard J Kestel. Improved methods and novel techniques for jet electropolishing of TEM foils. In Ron Anderson, editor, *Specimen Preparation for Transmission Electron Microscopy of Materials II*, volume 199 of *MRS symposium*, pages 51–74. Materials Research Society, MRS, San Francisco, California, USA, 1990.

- [29] Peter Sigmund. A mechanism of surface micro-roughening by ion bombardment. *Journal of Materials Science*, 8:1545–1553, 1973.
- [30] Peter Sigmund, André Fettouhi, and Andreas Schinner. Material dependence of electronic stopping. *Nuclear Instruments and Methods in Physics Research B*, 209:19–25, 2003.
- [31] D J Barber. Radiation damage in ion-milled specimens: characteristics, effects and methods of damage limitation. *Ultramicroscopy*, 52:101–125, 1993.
- [32] D B Williams and C B Carter. *Transmission electron microscopy*. Springer, 1996.
- [33] K Tsujimoto, S Tsuji, K Kuroda, and H Saka. Transmission electron microscopy of thin-film transistors on glass substrates. *Thin Solid Films*, 319:106–109, 1998.
- [34] M Sugiyama and G Sigesato. A review of focused ion beam technology and its applications in transmission electron microscopy. *Journal of Electron Microscopy*, 53:527–536, 2004.
- [35] N Hermanne and A Art. Microrelief of ion-bombarded crystals and induced damage. *Radiation Damage*, 5:203–211, 1970.
- [36] I. H. Wilson, N. J. Zheng, U. Knipping, and I. S. T. Tsong. Scanning tunneling microscopy of ion impacts on semiconductor surfaces. *Journal of Vacuum Science and Technology A: Vacuum, Surfaces, and Films*, 7:2840–2844, 1989.
- [37] G Lu, F Niu, and R Wang. Radiation damage and electron radiation induced recovery in ZnTe. *Radiation Effects and Defects in Solids*, 116:81–94, 1991.
- [38] J M Cairney and P R Munroe. Redeposition effects in transmission electron microscope specimens of FeAl–WC composites prepared using a focused ion beam. *Micron*, 34:97–107, 2003.

- [39] A G Cullis, N G Chew, and J L Hutchinson. Formation and elimination of surface ion milling defects in cadmium telluride, zinc sulphide and zinc selenide. *Ultramicroscopy*, 17:203–212, 1985.
- [40] S Ruvimov, Z Liliental-Weber, J Washburn, K J Duxstad, E E Haller, X-F Fan, S N Mohammad, W Kim, A E Botchkarev, and H Morkoç. Microstructure of Ti/Al and Ti/Al/Ni/Au ohmic contacts for n-GaN. *Applied Physics Letters*, 69:1556–1558, 1996.
- [41] J S Barnard, J Sharp, J R Tong, and P A Midgley. Weak-beam dark-field electron tomography of dislocations in GaN. In *EMAG-NANO 05 Imaging analysis and fabrication on the nanoscale*, volume 26, page 247. Journal of Physics, Institute of Physics Publishing, 2006.
- [42] J S Barnard, J Sharp, J R Tong, and P A Midgley. Three-dimensional analysis of dislocation networks in GaN using weak-beam dark-field electron tomography. *Philosophical Magazine*, 86:4901–4922, 2006.
- [43] J H Sharp, J S Barnard, K Kaneko, K Higashida, and P A Midgley. Dislocation tomography made easy: a reconstruction from ADF STEM images obtained using automated image shift correction. In *J. Phys. Conf. Ser. EMAG 07: Characterisation, manipulation and fabrication on the nanoscale*, volume 126, page 012013. Journal of Physics, Institute of Physics publishing, 2008.
- [44] J Sharp. Electron tomography of dislocations in gallium nitride. Master’s thesis, Department of Materials Science, University of Cambridge, UK, 2005. Available from author in PDF format on request; numerical calculations have been revisited since 2005.
- [45] A. Rosenfeld and A.C. Kak. *Digital Picture Processing*. Academic Press, New York, 1982.
- [46] Masaki Tanaka, Kenji Higashida, Kenji Kaneko, Satoshi Hata, and Masatoshi Mitsuhashi. Crack tip dislocations revealed by electron tomography in silicon single crystal. *Scripta Materialia*, 59:901904, 2008.

-
- [47] J Radon. Über die Bestimmung von Funktionen durch ihre Integralwerte längs gewisser Mannigfaltigkeiten. Berichte über die Verhandlungen der Königlich Sächsischen Gesellschaft der Wissenschaften zu Leipzig. *Math Phys Klasse*, 69:262, 1917.
- [48] V J Lowe and K S Naunheim. Positron emission tomography in lung cancer. *Annals of thoracic surgery*, 65:1821, 1998.
- [49] K H Khor, J-Y Buffière, W Ludwig, H Toda, H S Ubhi, P J Gregson, and I Sinclair. In situ high resolution synchrotron x-ray tomography of fatigue crack closure micromechanisms. *Journal of Physics: Condensed Matter*, 16:S3511, 2004.
- [50] D DeRosier and A Klug. Reconstruction of three-dimensional structures from electron micrographs. *Nature*, 217:130, 1968.
- [51] M Weyland and P A Midgley. Electron tomography. *Materials Today*, page 32, Dec 2004.
- [52] A.R. Lang. The projection topograph: a new method in x-ray diffraction microradiography. *Acta Crystallographica*, 12:249, 1959.
- [53] W Ludwig, P Cloetens, J Härtwig, J Baruchel, B Hamelin, and P Bastie. Three dimensional imaging of crystal defects by ‘tomotopography’. *Journal of Applied Crystallography*, 34:602, 2001.
- [54] K Haruta. New method of obtaining stereoscopic pairs of x-ray diffraction topographs. *Journal of Applied Physics*, 3:1789, 1965.
- [55] P.W. Hawkes. The electron microscope as a structure projector. In J. Frank, editor, *Electron Tomography: Three-dimensional Imaging with the Transmission Electron Microscope*, page 17. Plenum Press, New York–London, 1992.
- [56] L Cervera Gontard, R E Dunin-Borkowski, R K K Chong, D Ozkaya, and P A Midgley. Electron tomography of Pt nanocatalyst particles and their carbon support. In *EMAG-NANO 05 Imaging Analysis and*

Fabrication on the Nanoscale, volume 26, page 203. Journal of Physics, Insitute of Physics publishing, 2006.

- [57] D. D. Perovic, C. J. Rossouw, and A. Howie. Imaging elastic strains in high-angle annular dark field scanning transmission electron microscopy. *Ultramicroscopy*, 52:353–359, 1993.
- [58] J M Cowley and Y Huang. De-channelling contrast in annular dark-field STEM. *Ultramicroscopy*, 40:171–180, 1992.
- [59] A P Pathak, L N S Prakash Goteti, and S V S Nageswara Rao. Channeling radiation from relativistic electrons — study of stacking faults and dislocations. *Nuclear Instruments and Methods in Physics Research B*, 193:188–191, 2002.
- [60] Laurent Desbat and Andreas Wernsdörfer. Direct algebraic reconstruction and optimal sampling in vector field tomography. *IEEE transactions on signal processing*, 43:1798–1808, 1995.
- [61] M. Slaney and A.C. Kak. *Principles of Computerized Tomographic Imaging*. IEEE Press, 1988.
- [62] S R Deans. *The Radon Transform and Some of Its Applications*. Wiley, New York; Chichester, 1983.
- [63] A.C. Kak. Tomographic imaging with diffracting and non-diffracting sources. In T.Y. Young and K.S. Fu, editors, *Array Signal Processing*. Prentice-Hall, Englewood Cliffs, New Jersey, 1985.
- [64] R A Crowther, D J DeRosier, and A Klug. The reconstruction of a three-dimensional structure from projections and its application to electron microscopy. *Proceedings of the Royal Society of London A*, 317:319–340, 1970.
- [65] R Gordon, R Bender, and G T Herman. Algebraic reconstruction techniques (ART) for three-dimensional electron microscopy and x-ray photography. *Journal of Theoretical Biology*, 29:471–481, 1970.

-
- [66] H. Stark et al. Direct fourier reconstruction in computer tomography. *IEEE Transactions of Acoustic Speech Signal Processing*, ASSP-29:237, 1981.
- [67] Gilbert. Iterative methods for the three-dimensional reconstruction of an object from projections. *Journal of Theoretical Biology*, 36:105, 1972.
- [68] Sewell B T Lawrence M C, Jaffer M A. The application of the maximum-entropy method to electron-microscopic tomography. *Ultramicroscopy*, 31:285-302, 1989.
- [69] K J Batenburg, S Bals, J Sijbers, C Kubel, P A Midgley, J C Hernandez, U Kaiser, E R Encina, E A Coronado, and G Van Tendeloo. 3D imaging of nanomaterials by discrete tomography. *Ultramicroscopy*, 109:730-740, 2009.
- [70] M Radermacher and W Hoppe. Properties of 3D reconstruction from projections by conical tilting compared to single axis tilting. In *Electron Microscopy, volume 1: Physics*, page 132. Seventh European Congress on Electron Microscopy foundation, Leiden, 1980.
- [71] P G Kotula, L N Brewer, J Michael, and L Giannuzzi. Computed tomographic spectral imaging: 3D STEM-EDS spectral imaging. *Microscopy and Microanalysis*, 13 (Suppl. 02):1324-1325, 2007.
- [72] Stephen J. Norton. Iterative reconstruction algorithms: convergence as a function of spatial frequency. *Journal of the Optics Society of America A*, 2:6-14, 1985.
- [73] Claude E Shannon. Communication in the presence of noise. *Proceedings of the IRE*, 137:10-21, 1949. Reprinted as Proc. IEEE, vol. 86, pp 447-457, 1998.
- [74] P B Hirsch et al. A kinematical theory of diffraction contrast of electron transmission microscope images of dislocations and other

- defects. *Philosophical Transactions of the Royal Society*, A252:499, 1960.
- [75] D J H Cockayne, I L F Ray, and M J Whelan. Investigations of dislocation strain fields using weak beams. *Philosophical Magazine*, 20:1265, 1969.
- [76] W M Stobbs. *Electron Microscopy in Materials Science : Third course of the International School of Electron Microscopy, 'Ettore Majorana' International Centre for Scientific Culture*. Office for Official Publications of the European Communities, 1975. 591 pp.
- [77] W M Stobbs and C H Sworn. The weak beam technique as applied to the determination of the stacking-fault energy of copper. *Philosophical Magazine*, 24:1365–1381, 1971.
- [78] A Howie and C H Sworn. Column approximation effects in high resolution electron microscopy using weak diffracted beams. *Philosophical Magazine*, 22:861–864, 1970.
- [79] Robin Schäublin. Nanometric crystal defects in transmission electron microscopy. *Microscopy Research and Technique*, 69:305–316, 2006.
- [80] X H Wu et al. Defect structure of metal-organic chemical vapor deposition grown epitaxial (0001) GaN/Al₂O₃. *Journal of Applied Physics*, 80:3228, 1996.
- [81] D Cherns. The structure and optoelectronic properties of dislocations in GaN. *Journal of Physics condensed matter*, 12:17494, 2000.
- [82] X H Wu, L M Brown, D Kapolnek, S Keller, B Keller, S P DenBaars, and J S Speck. Defect structure of metal-organic chemical vapor deposition-grown epitaxial (0001) GaN/al₂O₃. *Journal of Applied Physics*, 80:3228, 1996.
- [83] X J Ning, F R Chein, and P Pirouz. Growth defects in GaN films on sapphire: The probable origin of threading dislocations. *Journal of Material Research*, 11:580, 1996.

-
- [84] L Meshi, D Cherns, I Griffiths, S Khongphetsak, A Gott, C Liu, S Denchitcharoen, P Shields, W Wang, R Champion, S Novikov, and T Foxon. The reduction of threading dislocations in GaN using a GaN nanocolumn interlayer. *Physica Status Solidi C*, 5:1645-1647, 2008.
- [85] S-L Sahonta, D Cherns, R Liu, F A Ponce, H Amano, and I Akasaki. CBED study of grain misorientations in AlGaN epilayers. *Ultramicroscopy*, 103:2332, 2005.
- [86] Suprijadi and H Saka. On the nature of a dislocation wake along a crack introduced in Si at the ductile-brittle transition temperature. *Philosophical Magazine Letters*, 78:435-443, 1998.
- [87] Pawel Penczek, Michael Marko, Karolyn Buttle, and Joachim Frank. Double-tilt electron tomography. *Ultramicroscopy*, 60:393-410, 1995.
- [88] R F Egerton. *Electron energy-loss spectroscopy in the electron microscope, 2nd Ed.* Kluwer/Plenum, 1996.
- [89] T. Malis, S. C. Cheng, and R. F. Egerton. EELS log-ratio technique for specimen-thickness measurement in the TEM. *Journal of Electron Microscopy Technique*, 8:193-200, 2005.
- [90] T Nakano, K Hayashi, Y Umakoshi, Y L Chiu, and P Veysseyère. Effects of Al concentration and resulting long-period superstructures on the plastic properties at room temperature of Al-rich TiAl single crystals. *Philosophical Magazine*, 85:2527-2548, 2005.
- [91] H Inui, M Matsumuro, D H Wu, and M Yamaguchi. Temperature dependence of yield stress, deformation mode and deformation structure in single crystals of TiAl (Ti-56 at.% Al). *Philosophical Magazine A*, 75:395-423, 1997.
- [92] K Hayashi, T Nakano, and Y Umakoshi. Plastic deformation behaviour and deformation substructure in Al-rich TiAl single crystals deformed at high temperatures. *Science and Technology of Advanced Materials*, 2:433-441, 2001.

- [93] W O Saxton, W Baumeister, and M Hahn. Three-dimensional reconstruction of imperfect two-dimensional crystals. *Ultramicroscopy*, 13:57–70, 1984.
- [94] Z L Wang. Dynamical theories of dark field imaging using diffusely scattered electrons in STEM and TEM. *Acta Crystallographica*, A51: 569, 1995.
- [95] D D Perovic, A Howie, and C J Rossouw. On the image contrast from dislocations in high-angle annular dark-field transmission electron microscopy. *Philosophical Magazine Letters*, 67:261–272, 1993.
- [96] Dmitri O. Klenov, Scott D. Findlay, Leslie J. Allen, and Susanne Stemmer. Influence of orientation on the contrast of high-angle annular dark-field images of silicon. *Physical Review B*, 76:014111, 2007.
- [97] M Weyland and P A Midgley. 3D microscopy in the physical sciences: the development of Z-contrast and EFTEM tomography. *Ultramicroscopy*, 96:413, 2003.
- [98] Z L Wang and D C Li. Dynamical diffraction of double-inelastically scattered electrons. *Philosophical magazine B*, 71:201–219, 1995.
- [99] A. Hangleiter et al. Suppression of nonradiative recombination by v-shaped pits in GaInN/GaN quantum wells produces a large increase in the light emission efficiency. *Physical Review Letters*, 95:127402, 2005.
- [100] R Langford. Focused ion beams techniques for nanomaterials characterization. *Microscopy Research and Techniques*, 69:538–549, 2006.
- [101] W J Tunstall, P B Hirsch, and J W Steeds. Effects of surface stress relaxation on the electron microscope images of dislocations normal to thin metal foils. *Philosophical Magazine*, 9:99, 1964.
- [102] John Allison. *Electronic integrated circuits: their technology and design*. McGraw-Hill, 1975.

- [103] Masaki Tanaka and Kenji Higashida. High-voltage electron-microscopical observation of crack-tip dislocations in silicon crystals. *Materials Science and Engineering A*, 400-401:426–430, 2005.
- [104] T Ono, G A Rozgonyi, C Au, T Messina, R K Goodall, and H R Huff. Oxygen precipitation behavior in 300 mm polished Czochralski silicon wafers. *Journal of The Electrochemical Society*, 146(10):3807–3811, 1999.
- [105] Z L Wang and J M Cowley. Simulating high-angle annular dark-field STEM images including inelastic thermal diffuse scattering. *Ultramicroscopy*, 31:437–454, 1989.
- [106] A Howie. Image contrast and localized signal selection techniques. *Journal of Microscopy*, 117:11, 1979.
- [107] X Meng, R E Schäublin, and W M Stobbs. Assessment of convergence effects in weak-beam transmission electron microscopy in partial spacing measurements in Ni_3Al . *Philosophical Magazine Letters*, 75:179–185, 1997.
- [108] P D Nellist and S J Pennycook. Incoherent imaging using dynamically scattered coherent electrons. *Ultramicroscopy*, 78:111–124, 1999.
- [109] P D Nellist and S J Pennycook. *The principles and interpretation of annular dark-field Z-contrast imaging*, pages 148–204. Number 113 in *Advances in imaging and electron physics*. Academic Press, 2000.
- [110] M Shiojiri and H Saijo. Imaging of high-angle annular dark-field scanning transmission electron microscopy and observations of GaN-based violet laser diodes. *Journal of Microscopy*, 223:172–178, 2006.
- [111] S J Pennycook and D E Jesson. High-resolution Z-contrast imaging of crystals. *Ultramicroscopy*, 37:14–38, 1991.
- [112] C R Hall and P B Hirsch. Effect of thermal diffuse scattering on propagation of high energy electrons through crystals. *Proceedings*

- of the Royal Society of London. Series A, Mathematical and Physical Sciences*, 286:158–177, 1965.
- [113] Z L Wang. Dislocation contrast in high-angle hollow-cone dark-field TEM. *Ultramicroscopy*, 53:73–90, 1994.
- [114] Sean Hillyard and John Silcox. Detector geometry, thermal diffuse scattering and strain effects in ADF STEM imaging. *Ultramicroscopy*, 58(1):6–17, 1995.
- [115] Adam Amali and Peter Rez. Theory of lattice resolution in high-angle annular dark-field images. *Microscopy and Microanalysis*, 3:28–46, 1997.
- [116] R F Loane, P Xu, and J Silcox. Thermal vibrations in convergent-beam electron diffraction. *Acta Crystallographica A*, 47:267–278, 1991.
- [117] Z L Wang. *Elastic and inelastic scattering in electron diffraction and imaging*. Plenum Press, 1995.
- [118] Peter Rez. The contrast of defects in inelastically scattered electrons. *Acta Crystallographica A*, 39:697–706, 1983.
- [119] U Wahl, E Alves, K Lorenz, J G Correia, T Monteiro, B De Vries, and A Vantomme and R Vianden. Lattice location and optical activation of rare earth implanted GaN. *Materials Science and Engineering B*, 105:132–140, 2003.
- [120] I Arslan, A Bleloch, E A Stach, S Ogut, and N D Browning. Using eels to observe composition and electronic structure variations at dislocation cores in GaN. *Philosophical Magazine*, 86:4727–4746, 2006.
- [121] J W Steeds. *Anisotropic Elasticity Theory of Dislocations*. Clarendon Press, 1973.
- [122] E J Kirkland, R F Loane, and J Silcox. Simulation of annular dark field stem images using a modified multislice method. *Ultramicroscopy*, 23:77–96, 1987.

-
- [123] J M Cowley. *Diffraction Physics*. Elsevier, 1981.
- [124] M A Kirk, R S Davidson, M L Jenkins, and R D Twisten. Measurement of diffuse electron scattering by single nanometre-sized defects in gold. *Philosophical Magazine*, 85:497–507, 2005.
- [125] D E Jesson and S J Pennycook. Incoherent imaging of thin specimens using coherently scattered electrons. *Proceedings of the Royal Society of London A*, 441:261–281, 1993.
- [126] P D Nellist and J Pennycook. Accurate structure determination from image reconstruction in ADF STEM. *Journal of Microscopy*, 190:159–170, 1998.
- [127] R. F. Loane, E. J. Kirkland, and J. Silcox. Visibility of single heavy atoms on thin crystalline silicon in simulated annular dark-field STEM images. *Acta Crystallographica A*, 44:912–927, 1988.
- [128] Donald S Gemmell. Channeling and related effects in the motion of charged particles through crystals. *Reviews of Modern Physics*, 46:129–227, 1974.
- [129] J Lindhard. Influence of crystal lattice on motion of energetic charged particles. *Konelinge Danske Videnskabernes Selskab Matematisk-Fysiske meddelelser, or, Royal Danish Academy of Sciences and Letters: Mathematical Physical Journal*, 34:14, 1965.
- [130] S J Pennycook. Z-contrast STEM for materials science. *Ultramicroscopy*, 30:58–69, 1989.
- [131] Sean Hillyard, Russell F Loane, and John Silcox. Annular dark-field imaging: resolution and thickness effects. *Ultramicroscopy*, 49:14–25, 1993.
- [132] J Liu and J M Cowley. Imaging dislocations with an annular dark-field detector. In G W Bailey, editor, *Proceedings of the 50th Annual Meeting of the Electron Microscopy Society of America*. EMS publishing, 1992.

- [133] S J Pennycook and D E Jesson. High-resolution Z -contrast imaging of crystals. *Ultramicroscopy*, 37:14–38, 1991.
- [134] L Fitting, S Thiel, A Schmehl, J Mannhart, and D A Muller. Subtleties in ADF imaging and spatially resolved EELS: A case study of low-angle twist boundaries in SrTiO_3 . *Ultramicroscopy*, 106:1053–1061, 2006.
- [135] S J Pennycook. Impurity lattice and sublattice location by electron channeling. *Scanning Microscopy*, 2:21–32, 1988.
- [136] J W Steeds, P M Jones, J E Loveluck, and K Cooke. The dependence of zone axis patterns on string integrals or the number of bound states in high energy electron diffraction. *Philosophical Magazine*, 36:309–322, 1977.

